Chalcophile elements track the fate of sulfur at Kīlauea Volcano, Hawai'i

Penny E. Wieser*[1], Frances Jenner[2], Marie Edmonds[1], John Maclennan[1], and Barbara E. Kunz[2].

[1] Department of Earth Sciences, University of Cambridge, Downing Street, Cambridge, UK, CB2 3EQ.

[2]School of Environment, Earth and Ecosystem Sciences, The Open University, Walton Hall, 7 Milton Keynes, Buckinghamshire, MK7 6AA.

**Corresponding Author: pew26@cam.ac.uk*

Abstract

Chalcophile element concentrations in melt inclusions and matrix glasses may be used to track sulfide saturation during mantle melting and crustal fractionation, and to investigate low pressure degassing processes. Erupted products from Kīlauea Volcano, Hawai'i record three stages of sulfide saturation (in the mantle, crust, and within lava lakes), separated by episodes of sulfide resorption during ascent through the thick Hawaiian lithosphere, and during syn-eruptive degassing. Residual sulfides in the mantle source retain chalcophile elements during melting, decoupling their variability from that of lithophile elements. The estimated S concentrations of Kīlauean primary melts (1387–1600 ppm) exceed model predictions of S^{2-} solubility at pressures and temperatures relevant to mantle melting, implying that some proportion of S is present as S^{6+}. Decompression associated with magma ascent through the thick Hawaiian lithosphere drives an increase in the sulfide concentration at sulfide saturation ($SCSS^{2-}$), resulting in shallow storage reservoirs (~1-5 km depth) being supplied with sulfide-undersaturated melts. A drop in temperature coupled with the fractionation of olivine (and chrome-spinel) causes the $SCSS^{2-}$ to decrease. Combined with an increase in melt S contents during olivine fractionation, this initiates a second stage of sulfide saturation at relatively high MgO contents (~10–14 wt% MgO). Syneruptive degassing drives the resorption of sulfides in contact with the carrier liquid. The covariance structure of Cu, MgO and Ni contents in melt inclusions and matrix glasses indicates that the dissolution of sulfides effectively liberates sulfide-hosted Cu and Ni back into the melt. The partitioning of S between the dissolving sulfide, melt and vapour phase accounts for between 10 and 40% of the total S release into the atmosphere. The participation of dense sulfide liquids in shallow degassing processes may result from their direct attachment to buoyant vapour bubbles, or olivine crystals which were remobilized prior to eruption. Sulfide resorption obscures the textural and chemical

record of sulfide saturation in matrix glasses, but not in melt inclusions, which are isolated from the late-stage release of chalcophile elements during sulfide breakdown.

Introduction

Volcanic eruptions emit vast quantities of sulfur (S) and sulfur-loving (chalcophile) elements to the atmosphere, causing perturbations to the global climate system and regional air quality (Robock, 2000; Witham and Oppenheimer, 2004). For example, during the last 35 years, the near-continuous effusion of lava at Kīlauea Volcano, Hawai'i has released globally significant amounts of S to the lower troposphere, culminating in fluxes of >50,000 t/day SO_2 during the lower East Rift Zone eruption in 2018 (Neal et al., 2018). These emissions have serious implications for respiratory health and agricultural productivity across the island (Longo et al., 2010; Nelson and Sewake, 2008; Tam et al., 2016).

The concentrations of sulfur and chalcophiles in primary melts entering Kīlauea volcano, and other basaltic systems, are predominantly controlled by the behaviour of sulfide during mantle melting (Ding and Dasgupta, 2018). During crystallization in crustal magma chambers, S contents may increase due to the fractionation of S-poor silicate phases, or become buffered by the stabilization of an immiscible sulfide phase (Smythe et al., 2017). Tracking the pre-eruptive evolution of S is non-trivial; erupted lavas have typically lost ~90% of their original S (Metrich and Mandeville, 2010), and evidence for sulfide fractionation may be obscured by the resorption of sulfides during low pressure degassing (Edmonds and Mather, 2017; Moore et al., 1980). These problems are often circumvented by measuring S contents in melt inclusions (pockets of melt trapped within growing crystals that are less susceptible to degassing than erupted carrier liquids), or through measurements of refractory chalcophile element abundances in quenched matrix glasses (Jenner et al., 2010; Reekie et al., 2019). However, these archives can be degraded by petrological processes; the concentrations of chalcophile elements in melt inclusions may be altered by the secondary growth of sulfide phases post-entrapment (e.g., Hartley et al., 2017). Additionally, S concentrations in melt inclusions at Kīlauea are highly variable within a given sample, possibly due to the mixing of degassed and undegassed melts at depth (identified in submarine glasses by Dixon et al., 1991), or the entrapment of melt inclusions during late-stage degassing (Thornber et al., 2015).

The alternative approach, where refractory chalcophile elements in matrix glasses are used as a proxy for S, relies on the assumption that these elements are significantly less volatile than S, so are resistant to low pressure degassing. For example, Se has been used to reconstruct the pre-degassing behaviour of S in subaqueous lavas under the assumption that it behaves identically to sulfur, but is refractory (Jenner et al., 2010, 2012, 2015; Reekie et al. 2019). However, measurements of significant fluxes of Se within volcanic plumes emitted at

Kīlauea and other basaltic volcanoes indicates that chalcophile element volatility may differ between subaqueous and subaerial eruptions (Crowe et al., 1987; Edmonds et al., 2018; Mather et al., 2012). Recently, lavas from Antuco, Chile, have been shown to have S and Se contents which are significantly lower than mid-oceanic ridge basalts (MORB), supporting the hypothesis that Se degasses at low pressures (Cox et al., 2019).

In this paper, we track the behaviour of S and other chalcophile elements (Cu, Zn, Mo, Cd, In, Sn, Sb, W, Tl, Bi, Se, As) from the Hawaiian mantle source to the site of subaerial eruptions using a suite of melt inclusions and matrix glasses from Kīlauea Volcano. Previous studies investigating sulfide saturation and chalcophile element behaviour at Kīlauea have been restricted to subaerial lavas which have fractionated beyond olivine control (e.g., those erupted during the 1955 and 1977 eruption; Desborough et al., 1968; Helz and Wright, 1992; Moore et al., 1980). There has been a particular focus in the literature on chalcophile element behaviour in lava lakes, where degassed magma ponded and fractionated in pre-existing pit craters (Skinner and Peck, 1969; Fleet and Stone, 1990; Greaney et al., 2017; Stone and Fleet, 1991). Until now, the most primitive glass composition at Kīlauea analysed for chalcophile elements had an MgO content of only 6.1 wt% (Fig. 1a; Greaney et al., 2017). In contrast, the spatter and scoria samples investigated in this study span a range of MgO contents (10.0–5.7 wt% MgO; Wieser et al., 2019), and were rapidly quenched following eruption. Thus, the three rift zone samples investigated in this study, which have experienced only olivine (+chrome-spinel) fractionation, provide new insights into the behaviour of chalcophile elements during mantle melting and fractional crystallization.

Ratios of chalcophile to lithophile elements in erupted melts (e.g., Pb/Ce, S/Dy, Sb/Pr) are frequently used to gain insight into various aspects of mantle evolution (Jochum and Hofmann, 1997; Kelley et al., 2013; Newsom et al., 1986; Saal et al., 2002). These studies generally assume that lithophile and chalcophile elements behave similarly during mantle melting, neglecting the complex changes in chalcophile element concentrations with increasing melt fraction in the presence of residual sulfides. The fate of sulfides during mantle melting for mid-ocean ridge and ocean island basalts remains uncertain (Ding and Dasgupta, 2018). Variations in the concentrations of platinum group elements (PGEs) in lavas across the Hawaiian islands, along with elevated Cu/Pd ratios, have been attributed to variable abundances of residual sulfide in the Hawaiian mantle plume (Bennett et al., 2000). In contrast, Greaney et al. (2017) estimate the chalcophile element concentration of the Kīlauean mantle source from the batch melting equation under the assumption of sulfide-absent melting. As the bulk K_D (silicate-melt partition coefficient) of chalcophile elements is substantially higher if sulfides are present in the mantle source, sulfide-free melting models will underestimate the concentrations of these elements if residual sulfides are in fact present in the Kīlauean mantle source. Clearly, the fate of mantle sulfides must be critically evaluated before chalcophile element signatures can be used to assess the presence or absence of recycled materials in the Hawaiian mantle plume (e.g., Greaney et al., 2017).

The point at which sulfides saturate during fractional crystallization in Hawaiian lavas is also debated (Bennett et al., 2000; Desborough et al., 1968; Dixon et al., 1997; Greaney et al., 2017; Helz et al., 2017; Tatsumi et al., 1999; Wallace and Anderson, 1998). It has been demonstrated, using the chalcophile element systematics of mid-ocean ridges and oceanic plateaux, that a second stage of sulfide saturation often occurs following ascent of magmas from the mantle and fractional crystallization of these sulfide-undersaturated melts in the crust (Jenner, 2017; Reekie et al., 2019). This second stage of sulfide saturation is driven by an increase in S concentrations during fractional crystallization (as S is incompatible in most silicate minerals), along with a concurrent decrease in the sulfide (S^{2-}) solubility at sulfide saturation (SCSS), due to dropping temperature and changes in melt chemistry (Smythe et al., 2017). Specifically, the SCSS describes the amount of S^{2-} present in a silicate melt in equilibrium with a sulfide phase (O'Neill, 2020; hereafter $SCSS^{2-}$ for clarity). While PGE fractionation trends in Hawaiian lavas have been attributed to sulfide saturation (Tatsumi et al., 1999), recent Cu measurements in whole rock and glasses from the Kīlauea Iki lava lake have led to suggestions that sulfides only fractionate at ~2 wt% MgO (when Cu starts to decrease; Greaney et al., 2017; Fig 1a). Furthermore, although sulfides are present in eruption pumices and lake samples from Kīlauea Iki with MgO>2 wt%, the wide variability in bulk sulfide composition has been attributed to sulfide formation during late-stage processes such as quenching, rather than during primary sulfide-liquid immiscibility (Stone and Fleet, 1991). Our new data challenges this dominant view, and instead supports a model where almost all erupting melts at Kīlauea (~10–14 wt% MgO) were sulfide-saturated prior to the onset of S degassing at shallow pressures (c.f. Ding and Dasgupta, 2018; Greaney et al., 2017; Helz et al., 2017; Pitcher et al., 2009; Skinner and Peck, 1969).

Finally, we investigate the effects of syn-eruptive chalcophile element degassing and sulfide resorption by comparing the chalcophile element abundances of matrix glasses and melt inclusions at Kīlauea, and undegassed submarine glasses from Lōiʻhi volcano. While there is growing evidence that Se degasses during subaerial eruptions (Cox et al., 2019; Mather et al., 2012), until now, Se analyses could only be conducted with laser ablation spot sizes greater than 100 µm. This prevented in-situ analyses of melt inclusions (Jenner and O'Neill, 2012), making it difficult to pinpoint the timing of Se loss in relation to other volatile species (e.g., S). In this study, we utilize a novel method by which Se and As are measured in melt inclusions using a line scan with a diameter of 50 µm diameter (Supplementary Fig. A1). This analysis demonstrates that Se and S degas almost concurrently at Kīlauea. Overall, comparisons between matrix glass and melt inclusion compositions allow us to estimate the influence of sulfide saturation, and subsequent resorption on the sulfur outgassing budget of Kīlauean eruptions.

2. Methods

2.1 Sample Details

Melt inclusions and matrix glasses were analysed from rapidly-quenched spatter and tephra from four subaerial eruptions temporally associated with the East Rift Zone (ERZ) eruption at Mauna Ulu. Three eruptions occurred on Kīlauea's rift zones: (1) The highest fountaining phase of Mauna Ulu (Episode 12; December, 1969; ERZ, Swanson et al., 1979) (2) The Pauahi Crater eruption (November, 1973; ERZ) and (3) The Seismic South West Rift Zone (SSWRZ) fissure eruption of December, 1974 (Poland et al., 2014). The fourth eruption occurred within the summit caldera in August, 1971. To further constrain sulfide occurrence and chemistry at Kīlauea, scoria and lava samples from various locations across the Kīlauean edifice were examined (see Supplementary Fig. A2; Supplementary Table A1). To supplement this dataset from Kīlauea, 18 submarine glasses from Lōiʻhi Volcano collected using submersibles at water depths of ~980–4700 m were analysed (Garcia et al., 1998, 1993; Pietruszka et al., 2011).

2.2 Analytical Methodology

Glass chips were handpicked from jaw-crushed tephra and spatter samples and mounted in epoxy stubs. Melt inclusions were exposed by individually mounting picked olivines on glass slides in Crystalbond^{TM} and grinding down to the level of melt inclusions with 250 – 1500 grade wet and dry paper. This method allowed embayments to be identified and discarded. Exposed melt inclusions were then mounted in epoxy and polished with progressively finer silicon pastes.

Major elements in Kīlauean melt inclusions, host olivines and matrix glasses were measured using the Cameca SX100 EPMA in the Department of Earth Sciences, University of Cambridge. Trace elements in Kīlauean matrix glasses and melt inclusions were analysed by laser ablation inductively coupled mass spectrometry (LA-ICP-MS/MS) at the School of Environment, Earth and Ecosystem Sciences at the Open University using a Photon Machines Analyte G2 193 nm excimer laser system coupled to an Agilent 8800 ICP-QQQ following the techniques described in Jenner et al. (2015; additional details in Appendix A). Kīlauean matrix glasses were analysed with a spot size of 110 µm. Melt inclusions were analysed at varying spot sizes (65 µm, 50 µm, 40 µm and 25 µm) depending on the diameter of the inclusion. The surface of melt inclusions were pre-ablated (3 laser shots) prior to analysis. Analyses were performed manually to ensure that laser spots were placed such that they did not overlap with the host olivine, or vapour bubbles below the surface. Ni signals were monitored during each analysis, and signals were carefully selected in Iolite software to only include the signal from the melt inclusion. Backgrounds were measured for 30 seconds prior to each analysis, followed by 20 seconds of signal and 50 seconds washout. NIST-SRM 612 was used for external calibration and ^{43}Ca for internal calibration of trace element data. BCR-2G was used as the secondary standard to monitor precision and accuracy.

Major and lithophile element concentrations for the Kīlauean glasses and melt inclusions were reported in Wieser et al. (2019). Repeated analyses of secondary standards for these elements lie within ±5% of long-term (>2 years) Open University laboratory preferred values and preferred values for BCR-2G reported in Jenner and O'Neill, (2012). Repeated analyses of secondary standards for the chalcophile element concentrations reported in this study predominantly lie within ±5% for Ni, Cu, Zn, ±10% for Mo, Sb, W, As, and ±20–30% for Cd, In, Bi, Tl, Sn, Se of preferred values (see Appendix B for more detail). Some of the variability in the latter elements may be attributed to standard heterogeneity (Jenner and Arevalo, 2016) . Precision (calculated from the standard deviation of 55 repeated standard analyses divided by the mean) was between 5–10% for most chalcophile elements (12% for Tl, 19% for Bi). Lōiʻhi matrix glasses were analysed by EPMA at the Smithsonian Institution (see Jenner et al., 2015 for description of analytical techniques). Each glass was analysed three times and averaged. SIMS and LA-ICP-MS analyses of the Lōiʻhi glasses were undertaken at the Carnegie Institution of Washington, and the Australian National University, respectively (see Jenner et al., 2015 for details), and the Open University (Se and As only).

Se and As are both affected by polyatomic and doubly charged interferences, and therefore require a different analytical protocol from the other trace elements. In Kīlauean and Lōiʻhi matrix glasses, Se and As were analysed using a spot size of 110 µm. Se and As in melt inclusions were measured using lines scans with a width of 50 µm. Line scans started and ended in the surrounding olivine, allowing careful selection of the signal from the melt inclusion in Iolite (Supplementary Fig. A1). Analyses were performed in oxygen mode using MS/MS mode, mass shifting ^{80}Se and ^{75}As to ^{96}SeO^{+} and ^{91}AsO^{+}. This allowed effective elimination of all interferences, monitored by comparing analyses of in-house Se and As standards to preferred values (measured using isotope dilution ICP-MS). NIST 612 was used for external calibration of data, with ^{29}Si used for internal calibration. NIST SRM 612 has considerably higher contents of some elements compared to volcanic materials (e.g., NIST SRM 612 has 15.2 ppm Se, Jenner et al., 2009). To avoid 'phantom' Se and other memory effects from analyses of these standards (see Jenner and O'Neill, 2012), repeat analyses of San Carlos olivine were undertaken prior to sample analyses. Accuracy was ±10% relative to in-house standards (see Jenner et al., 2015) with Se and As concentrations close to those in our samples.

Sulfides were identified using an automated approach utilizing backscatter electron (BSE) and secondary electron (SE) imaging on a FEI Quanta 650FEG SEM at the University of Cambridge. BSE maps of epoxy mounts were collected with the brightness and contrast of the image adjusted such that only sulfides were visible. Concurrent collection of SE maps at normal brightness and contrast conditions allowed the position of sulfides within grains to be determined. While reflected light observations may bias observations towards larger sulfides, this method ensured that all sulfides greater than ~1 µm were identified. Bulk sulfide compositions were quantified by summing over energy dispersive x-ray spectroscopy (EDS) maps, as the fine scale exsolution features of many sulfides resulted in highly imprecise EPMA point analyses (even with a defocused beam). Quantification of EDS maps collected for secondary sulfide standards characterized by EPMA (pyrite, chalcopyrite and pentlandite) during each analytical session allowed assessment of the accuracy and the precision of EDS quantification. Precision for EDS quantification was <1%, and the accuracy relative to EPMA measurements of these standards was within ±5%. EDS results were corrected for consistent offsets from EPMA measurements by a factor of 0.96 for Fe, and 1.025 for Ni and Cu. Additional analytical details are provided in Appendix A.

3. Results

3.1 Glass and Melt inclusion Chemistry

Matrix glasses from the three Kīlauean rift eruptions (Mauna Ulu, 1969, Pauhi Crater, 1973, and SSWRZ, 1974) are relatively primitive, with 7.4–10 wt% MgO (Fig. 2), and 10.2–11.2 wt% CaO (Supplementary Fig. A3). Their major element systematics, along with the absence of clinopyroxene and plagioclase phenocrysts, indicate that these lavas experienced only olivine (+chrome-spinel) fractionation (Wright and Fiske, 1971; Supplementary Fig. A3). The high MgO contents of these glasses relative to the vast majority of subaerial Kīlauea deposits (Helz et al., 2014), combined with their simple fractionation trajectories, makes them suitable for assessment of the behaviour of chalcophile elements during mantle melting. Glasses from the 1971 summit eruption are more evolved than the three rift eruptions (5.7–6.6 wt% MgO, 10.71–11.12 wt% CaO; Fig. 2; Supplementary Fig. A3) and they contain small phenocrysts of clinopyroxene. Lōiʻhi glasses are variably evolved, with MgO contents between 5.1–7.9 wt% MgO (Fig. 2). Uncorrected Kīlauean melt inclusions have MgO contents which overlap with the compositions of their co-erupted erupted matrix glasses (Fig. 2a; Wieser et al., 2019). The amount of post-entrapment crystallization calculated using the Petrolog3 “Olivine MI” tool (Danyushevsky et al., 2011) at QFM assuming FeO*=11.33 wt% (for consistency with previous studies; Wieser et al., 2019; Sides et al., 2014a, b) varies from -12 to 29%. Corrected melt inclusion MgO contents range from 6.9–13.3 wt% (Fig. 2b).

Uncorrected Kīlauean melt inclusion compositions show variable S contents, from ~100–1904 ppm (Fig. 2a), while melt inclusion compositions corrected for post-entrapment crystallization (assuming S is perfectly incompatible in olivine) range between 82–1978 ppm (Fig. 2b). Kīlauean matrix glasses have substantially lower S contents (~82–190 ppm) than melt inclusions, while submarine Lōʻihi matrix glasses have S contents mostly exceeding those in even the most S-rich Kīlauean melt inclusions (~1010–2073 ppm; Fig. 2a). Melt inclusions with the highest S concentrations have Cl concentrations extending to higher values than erupted matrix glasses, although the correlation between Cl and S for the combined Kīlauean dataset is relatively weak (R^2=0.13; Fig. 3a). In contrast, there is a strong correlation between S and Se (R^2=0.90; Fig. 3b), and a moderate correlation between S and Bi (R^2=0.34; Fig. 3c). Lōʻihi glasses have similar Se, Bi, Cd and Cu concentrations to the Kīlauean melt inclusions with the highest S concentrations, but significantly higher Cl, and lower As concentrations (Fig. 3).

Kīlauean matrix glasses show a slight increase in Cu with decreasing MgO (Fig. 2c), consistent with literature observations of Cu systematics from the Kīlauea Iki lava lake (Greaney et al., 2017; Fig. 1a). In contrast, the more restricted dataset for Lōʻihi glasses indicates that Cu decreases with decreasing MgO (R^2=0.44; Fig. 2c; Supplementary Fig. A4). Uncorrected Kīlauean melt inclusions show Cu contents which overlap with and extend to significantly lower values than matrix glasses (Fig. 2c). Following a correction for post-entrapment crystallization (assuming $K_{D,Cu}^{Ol/melt}$ = 0.1; Greaney et al., 2017), approximately half of melt inclusions with high MgO contents (~12-14 wt%) lie on the extension of the fractional crystallization trajectory defined by matrix glasses, while the other half plot to significantly lower Cu concentrations. The majority of inclusions with <10 wt % MgO have lower Cu contents than matrix glasses (Fig. 2d).

The trace element compositions of matrix glasses from the three rift eruptions which have not fractionated beyond olivine control (MgO>6.8 wt%; Wright and Fiske, 1971) were corrected for the effect of variable olivine fractionation by projecting back to 16 wt% MgO using the reverse crystallization tool in Petrolog3. For simplicity, all elements except Cu ($K_{D,Cu}^{Ol/melt}$ = 0.1) were assumed to be entirely incompatible in olivine. Fractionation-corrected (FC) glass compositions exhibit strong positive correlations between highly incompatible lithophile elements (e.g., Ba vs. Ce, Ba vs. La; Fig 4a-b). In contrast, Yb, Cu, Cd and Pb show weak, or even slightly negative correlations against Ba (Fig. 4c-f).

3.2 Sulfide Occurrence

Automated BSE-SE mapping identified sulfides in 7 different subaerial eruptions at Kīlauea (with glass MgO contents ranging from ~6–10 wt%). Sulfides are relatively rare, but were observed in four textural contexts:

1) Included in olivine phenocrysts (Fig. 5a), often alongside spinels and/or variable quantities of melt (Fig. 5e, f, g, h; Supplementary Fig. A5)
2) Within glassy, relatively open embayments with moderate-high S contents (Fig. 5c, d). In one instance, the sulfide is attached to the face of the olivine crystal (Fig. 5c).
4) In the walls of melt inclusion vapour bubbles and matrix glass vesicles (Fig. 5b; Supplementary Fig. A6-7).

Sulfides are roughly spherical to ellipsoidal, with diameters between 3–30 µm, except for bubble wall sulfides, which have diameters of ~0.5–3.0 µm (Fig. 5). EDS mapping reveals that sulfides consist of exsolved Cu- and Ni-rich phases, often with a separate Fe-rich phase (Fig. 5c, f, i, j). These textures likely result from the exsolution of monosulfide-intermediate solid solution (MSS-ISS) phases from an immiscible sulfide liquid (Czamanske and Moore, 1977; Patten et al., 2012). These findings build on literature reports; sulfide inclusions have been noted in primitive olivines erupted in Kīlauea Iki pumices ($Fo_{88.5}$; Helz 1987), and within silicate phases and matrix glass from the 1955 and 1977 eruptions of Kīlauea (Desborough et al., 1968; Helz and Wright, 1992; Moore et al., 1980).

Interestingly, only 2 sulfides were found in Kīlauean matrix glasses in comparison to the 14 sulfides found when mapping a roughly equivalent area of olivine crystals. Sulfides within matrix glasses have complex external morphologies (Fig. 6; Supplementary Fig. A8) compared with the smooth, spherical morphology of sulfides hosted within olivine crystals, embayments, and melt inclusions (Fig. 5). EDS mapping reveals that sulfides with these complex morphologies are predominantly composed of Fe and O, with only small quantities of Cu, Ni and S-rich material (~1 µm; Fig. 6; Supplementary Fig. A8). In contrast, spherical sulfides are very O-poor (Supplementary Fig. A9). Spherical, O-poor sulfides with comparable exsolution textures to those found within Kīlauean olivines and melt inclusions are relatively abundant within Lōʻihi matrix glasses. No texturally complex, O-rich sulfides were observed in Lōʻihi glasses.

4. Discussion

4.1 Sulfide in Kīlauea's mantle source

The fate of sulfides during mantle melting can be assessed by comparing the S concentrations of primary magmas to models of the sulfide content at sulfide saturation ($SCSS^{2-}$). If residual sulfide is present during mantle melting, the concentration of S^{2-} in the melt in equilibrium with this mantle is equal to the $SCSS^{2-}$; once sulfide is exhausted, the S^{2-} concentration in melts drops to significantly lower values than the $SCSS^{2-}$ (Ding and Dasgupta, 2018). Thus, if residual sulfides are present throughout the melting interval, the calculated $SCSS^{2-}$ should be approximately equal to the S^{2-} concentration of primary Kīlauean melts. In contrast, if the mantle has exhausted sulfide, primary melts should have S^{2-} concentrations less than the $SCSS^{2-}$.

For a given pressure, temperature, and melt composition, there are a variety of models to calculate the $SCSS^{2-}$ (e.g., Fortin et al., 2015; Li and Ripley, 2009, 2005; Smythe et al., 2017; O'Neill, 2020). However, most experiments used to calibrate $SCSS^{2-}$ models have been performed on FeS liquids, despite the fact that sulfides in basaltic lavas and mantle peridotites contain substantial quantities of Ni and Cu (Kiseeva et al., 2017; Patten et al., 2013; Smythe et al., 2017; Figs. 5c, f, i, j). The $SCSS^{2-}$ decreases as the ratio of Fe/(Fe+Ni+Cu) in the sulfide decreases, so $SCSS^{2-}$ models based on experiments with FeS sulfides will substantially overestimate the predicted $SCSS^{2-}$ (Smythe et al., 2017). To account for this, only the two most recent $SCSS^{2-}$ models that include a correction for the Ni and Cu contents of sulfides were used (Smythe et al., 2017; O'Neill, 2020).

The $SCSS^{2-}$ along PT paths for melts produced from a peridotitic mantle ascending from its solidus to the base of the lithosphere beneath the island of Hawai'i were calculated for three different potential temperatures (1450 ˚C, 1550 ˚C, 1650˚C; Fig. 7a). PT paths were calculated using Melt-PX (Lambart et al., 2016). The pressure at which melting terminated was calculated using estimated lithospheric thicknesses of 90–110 km (Li et al., 2004; Wölbern et al., 2006), assuming 15 km of crust with the density-depth profile of Putirka (2017), and a mantle with ρ=3300 kgm^{-3}. A constant primary melt composition was used for all points along the PT array in $SCSS^{2-}$ models. This composition was adjusted from that of Clague et al. (1991), with Cu=100 ppm and Ni=900 ppm, and FeO_T reduced by 3.2% to better fit the liquid line of descent for Kīlauea for the glasses measured in this study (Supplementary Fig. A3). The $SCSS^{2-}$ models of O'Neill (2020) and Smythe et al. (2017; hereafter O2020 and S2017 for brevity) both calculate the composition of the co-existing sulfide. However, in both models (but particularly in the S2017 model), the calculated sulfide compositions are very Ni-rich and Fe-poor compared with the vast majority of observed sulfide compositions within mantle peridotites and pyroxenites (Fig. 7b). This may reflect the fact that the sulfide-silicate partition coefficients used to calculate sulfide compositions in these models are based on parameterizations performed at significantly lower pressures than those relevant to mantle melting beneath Kīlauea. For example, sulfide compositions in the S2017 model are calculated using the sulfide-silicate partitioning behaviour determined by Kiseeva and Wood (2015) at 1.5 GPa.

Due to the absence of partitioning data at high pressures, we favour the results from SCSS^{2-} models where the sulfide composition was fixed at 5 wt% Cu, 20 wt% Ni, 33 wt% S, 42 wt% Fe (after Ding and Dasgupta, 2018; yellow square; Fig. 7b).

The S content of primary melts at Kīlauea was estimated from PEC-corrected S contents in melt inclusions (this study; Sides et al., 2014a, b). The upper limit of primary melts was set at 1600 ppm, based on the approximately constant upper limit of PEC-corrected melt inclusion data (ignoring a small number of inclusions with significantly higher S; Fig. 2b). As S behaves incompatibly during olivine-only fractionation, a minimum value for the primary S concentration of 1387 ppm was calculated by back-projecting the 1600 ppm observed at ~11.33 wt% MgO to 17.1 wt% MgO (a reasonable upper limit of the MgO content for Kīlauean primary melts; Clague et al., 1991) assuming S is entirely incompatible in olivine (Fig. 2b).

The SCSS^{2-} model trajectories using calculated sulfide compositions lie significantly below the range of S contents in primary melts at all pressures (Fig. 7c). Interestingly, the S2017 model shows a decrease in the SCSS^{2-} with decreasing pressure due to changes in the sulfide composition, which is the opposite trajectory to that expected from the strong pressure dependency on the SCSS^{2-}. This behaviour is likely anomalous, reflecting the absence of suitable parameterizations for sulfide-liquid partitioning at high pressure. In the O2020 model with a fixed sulfide composition, the SCSS^{2-} model trajectories increase with decreasing pressure, intercepting the field defined by the S contents of primary melts at ~4.5 GPa for T_p=1650˚C, and ~3 GPa for T_p=1450˚C (dashed lines; Fig. 7d). In the S2017 model with a fixed sulfide composition, only melts produced right at the base of the lithosphere for T_p=1650˚C (beige bar; Li et al., 2004; Wölbern et al., 2006) have SCSS^{2-} values comparable to the S contents of primary melts (solid lines; Fig. 7d). As primary melts supplied to the volcanic edifice reflect an aggregation of melts formed over a wide range of depths, both models indicate that mantle melts cannot dissolve enough S^{2-} to account for the high S contents observed in primitive melt inclusions (Fig. 2, Fig. 7). Crucially, this is the first line of evidence that sulfides were present throughout the melting interval at Kīlauea; if sulfides were exhausted during melting, the S contents of melt inclusions would be lower than the modelled SCSS^{2-} values.

The fact that melt inclusion S contents are higher than modelled SCSS^{2-} values can be reconciled by considering the elevated oxidation state of Hawaiian melts relative to MORB (Brounce et al., 2017; Moussallam et al., 2019, 2016; Fig. 8a). The speciation of S in basaltic melts undergoes an abrupt transition from S^{2-} and S^{6+} with increasing fO$_2$ between QFM and QFM+2 (Jugo et al., 2010). S^{6+} species are an order of magnitude more soluble than S^{2-} species in basaltic melts, only forming a separate sulfate phase such as anhydrite at very high melt S contents (~1.5 wt%, Jugo et al., 2005). Thus, in relatively S-poor melts such as those at Kīlauea (<1600 ppm), the exponential increase in S^{6+} species with increasing fO_2 drives an exponential increase in the total solubility of S (Jugo et al., 2010). As models of sulfide solubility (e.g., S2017, O2020) only account for S^{2-} species, if S^{6+} species are present, a correction must be applied to $SCSS^{2-}$ model outputs to calculate the total solubility of S (hereafter $SCSS_{Tot}$):

$$SCSS_{Tot} = \frac{SCSS^{2-}}{(1-\frac{S^{6+}}{\sum S})} \qquad \text{(Equation 1; Jugo et al., 2010)}$$

For example, if the $SCSS^{2-}$ = 1300 ppm (Fig. 7d), but Kīlauean melts contains 10% S^{6+}, the $SCSS_{Tot}$ would equal 1444 ppm. Thus, the presence of even a relatively small proportion of S^{6+} species can account for the fact that primary Kīlauean melts have S contents exceeding the solubility of S^{2-} species at pressures and temperatures relevant to melt generation in the mantle.

To our knowledge, there are no published measurements of S speciation from shield-stage tholeiitic lavas at Kīlauea. Early submarine alkalic lavas have S^{6+}/S_T ratios of 0.09-0.24 (determined by X-ray absorption near-edge structure- XANES; Jugo et al., 2010; Fig. 8b). While Sisson (2003) suggested that these lavas are more oxidised than shield-stage lavas, his fO_2 estimates of ~ΔQFM+0.7 (derived from analyses of olivine-phenocryst rims) align with recent XANES measurements in Kīlauean melt inclusions (Helz et al., 2017; Moussallam et al., 2016; Fig. 8b). Further constraints can be derived from other Hawaiian volcanoes: XANES measurements of submarine basalts from Mauna Kea and Lōiʻhi show S^{6+}/S_T ratios up to ~0.1 (Brounce et al., 2017) and 0.31 respectively (Jugo et al., 2010). However, there is a concerning lack of consistency between different studies; the S^{6+}/S_T of a single sample from Lōiʻhi has been variably estimated at 0.21 and 0.144 using the SKα peak shift (Wallace and Carmichael, 1994; Wallace and Carmichael, 1992), and -0.24 (XANES, Jugo et al., 2010). While the final number has no physical meaning, there is no correlation between the S^{6+}/S_T values in any of the six samples measured by Jugo et al. (2010) and Wallace and Carmichael, (1992; Supplementary Fig. A10). This analytical uncertainty may reflect electron transfer upon quenching between Fe^{2+} and S^{6+} species, discrepancies between SKα peak shift and XANES measurements, or beam damage (Smythe et al., 2017).

An alternative approach to estimate the proportion of S^{6+} species utilizes the strong coupling of the redox states of Fe and S. Jugo et al. (2010) performed experiments on predominantly hydrous basaltic and andesitic melts at 1050˚C, 200 MPa, yielding the following relationship:

$$\frac{S^{6+}}{S_T} = \frac{1}{1+10^{(2.1-2\Delta FMQ)}} \qquad \text{(Equation 2)}$$

Nash et al. (2019) performed experiments on basaltic-dacitic compositions at 1300˚C, and 1 atmosphere. They attribute differences in the observed transition of S redox relative to Fe redox between their study and that of Jugo et al. (2010) to a strong temperature dependence, which is incorporated in their parameterization:

$$\log\frac{S^{6+}}{S^{2-}} = 8\log\frac{Fe^{3+}}{Fe^{2+}} + \frac{8.7436\times10^{6}}{T^{2}} + \frac{27703}{T} + 20.273 \text{ (Equation 3)}$$

While the differences in pressure between these two studies (1 atmosphere vs. 200 MPa) are likely negligible (Nash et al., 2019), the speciation transition has been shown to shift by ~1.5 log units of fO_2 between 0.5–1.5 GPa (Matjuschkin et al., 2016). Unfortunately, as experiments investigating the competing effects of pressure and temperature at conditions relevant to mantle melting beneath the thick Hawaiian lithosphere have not been performed, it would be unwise to apply existing experimental parametrizations to estimate the S redox state. However, based on the ubiquitous (but variable) presence of S^{6+} species in a variety of Hawaiian melts, and the fact that S concentrations in primary melts exceed calculations of the $SCSS^{2-}$, it is reasonable to conclude that the high S contents of primary Kīlauean magmas result from the presence of residual sulfide in the mantle source and the presence of non-negligible quantities of S^{6+} in primary melts. To increase our understanding of the behaviour of sulfides during mantle melting, more experimental work investigating the speciation transition at higher pressures and temperatures is clearly needed.

A complementary approach to quantify the longevity of residual sulfide in the Kīlauean mantle source uses the differential behaviour of lithophile and chalcophile elements during mantle melting. Lavas erupted at Kīlauea volcano show cyclic variations in trace element and isotope ratios (e.g., $^{206}Pb/^{204}Pb$, Nb/Y; Pietruszka and Garcia, 1999; Sides et al., 2014a, b), attributed to variations in melt extent and mantle source heterogeneity (Hofmann et al., 1984; Pietruszka et al., 2018). The suite of eruptions investigated in this study (1969–1974) incorporate some of the most rapid changes in lava chemistry over the past few hundred years (Pietruszka and Garcia, 1999; Wieser et al., 2019), and show chemical variations consistent with changes in extent of melting (Hofmann et al., 1984). Thus, they provide the ideal opportunity to evaluate the differential behaviour of chalcophile and lithophile elements during mantle melting.

The concentration of chalcophile elements in mantle melts is controlled by the initial concentration in the mantle source (C_i), the melt extent (F), and the bulk partition coefficient between the silicate melt and the mantle residue (which may contain silicate and sulfide phases). The concentrations of two elements with low bulk K_Ds in suites of lavas spanning a range of melt extents are well-correlated (e.g., Ba vs. Ce and La; Fig. 4a-b; Hofmann et al., 1984). In contrast, if one element has a high K_D in a residual phase (e.g., Yb in garnet), giving it a bulk K_D close to 1, concentrations will be buffered across a wide range of melt extents. The gradient of a linear regression between this element and a highly incompatible element such as Ba will be ~0 (Fig. 4c; Hoffman et al., 1984). In the past, such comparisons have been used to demonstrate that residual garnet is present throughout the melting interval at Kīlauea (Hofmann et al., 1984). Like Yb, chalcophile elements show poor correlations with Ba (Fig. 4d-f). This implies that chalcophile elements are buffered by the presence of a residual phase during melting in which these elements have a high K_D. Residual sulfide is the most likely candidate, as chalcophile elements have very high K_Ds in sulfides (e.g., $K_{D,Cu}^{sulf/melt}$ = 61–729 and $K_{D,Pb}^{sulf/melt}$ =7–145 for a wide range of melt FeO contents; Kiseeva and Wood, 2015; $K_{D,Cu}^{sulf/melt}$ = 800–4600, $K_{D,Pb}^{sulf/melt}$ =24–170 in basaltic-rhyolitic melts; Li and Audétat, 2015), but low K_Ds in silicates (Lee et al., 2012; Liu et al., 2014). However, it is also worth nothing that while $K_{D,Cd}^{sulf/melt}$= 12-201 (Kiseeva and Wood, 2015), previous studies have demonstrated that the major host for Cd in the mantle is clinopyroxene (Witt-Eickschen et al., 2009).

To demonstrate the variable response of chalcophile and lithophile elements during mantle melting, we model the behaviour of Cu and Ba in aggregated, small fraction batch melts (after Lee et al., 2012; see Appendix A for details). For simplicity, it was assumed that all the S in the mantle was held within sulfides and the concentration of S in mantle melts produced while sulfides were present in the residue was 1600 ppm (Fig. 2b). The amount of residual sulfide present at each step was calculated assuming that mantle sulfides contain 33 wt% S. The concentration of Ba and Cu in the mantle prior to the onset of melting were set at 6.85 and 20 ppm respectively (Palme and O'Neill, 2014). The partition coefficient of Cu in sulfide varies as a function of temperature and sulfide composition (Kiseeva and Wood, 2015). Assuming a sulfide composition of 20% Ni, 5% Cu (Fig. 5b; Ding and Dasgupta, 2018) and a liquid FeO content of 11.33 wt% (Supplementary Figure D), $K_{D,Cu}^{sulf/melt}$ varies from ~250 to ~150 for T=1500 and 1700˚C respectively (Fig. 5a; Kiseeva and Wood, 2015). However, previous studies modelling Cu during mantle melting have used values of $K_{D,Cu}^{sulfide/melt}$ as high as 800 (Lee et al., 2012). To reflect the uncertainty in this parameter, models were run for $K_{D,Cu}^{sulf/melt}$ = 200 and 800. Model melt compositions were compared to fractionation-corrected glass compositions from the three rift eruptions of this study which have only fractionated olivine (and minor chrome-spinel; MgO >6.8 wt%, Wright and Fiske, 1971).

At the onset of melting, the presence of residual sulfide in the mantle raises the bulk K_D for Cu, causing aggregated melts to have significantly lower Cu concentrations than melts produced in a sulfide-free mantle (purple vs. green lines; Fig. 9a-d). The concentration of Cu at the initiation of melting decreases with increasing initial mantle S contents Rapid changes in Ba (which is highly incompatible) combined with the buffering of Cu by residual sulfide (Fig.

9a-d) results in the gradient of Cu vs. Ba being close to zero (Fig. 9c-f). The production of S-rich melts results in the amount of sulfide in the mantle source declining throughout the melting interval. This drives rapid changes in the bulk K_D of Cu until the point at which sulfide is exhausted (black star), after which Cu acts almost incompatibly (Bulk K_D=0.046). For $K_{D,Cu}^{sulf/melt}$=800, melt Cu concentrations peak slightly after the exhaustion of sulfides (Fig. 9b, d; Lee et al., 2012). For $K_{D,Cu}^{sulf/melt}$=200, Cu concentration in the melt remains approximately constant until the melt fraction at which sulfides are exhausted (Fig. 9 a, c). In both scenarios, as the point of sulfide exhaustion is approached, the gradients start to deviate from zero, although in the high K_D case, the rapid increase in Cu concentrations results in a negative gradient, while in the low K_D case the gradient is positive (Fig. 9e-f). Once sulfides are exhausted, the Cu concentrations gradually approach the compositions of melts produced from a mantle which was sulfide free from the onset of melting (green lines), and the gradients become strongly positive (Fig. 9e-f).

The concentration of Cu and the gradient of Cu vs. Ba in our lavas, along with prior constraints on the extent of mantle melting at Kīlauea, provide insight into the fate of mantle sulfides. Previous studies of trace element abundances in Kīlauean lavas have suggested that the mantle source undergoes 5–10% melting (grey box; Fig. 9a-b; Bennett et al., 2000; Norman et al., 2002). The range of Ba concentrations observed in the glasses investigated in this study are consistent with melt extents between F=0.078–0.091 (Supplementary Fig. A12). If sulfides were exhausted very early on in the melting interval (e.g., $S_{i,\ Per}$ = 50 ppm; solid purple line), Cu concentrations in melts produced at F=0.05–0.1 are similar to those expected from melting of a mantle source which was sulfide-free throughout the melting interval (solid green vs. solid purple line; Fig. 9a-b). As Cu is relatively incompatible in silicates, this model exhibits a strong positive correlation between Cu and Ba for the range of Ba concentrations in Kīlauean glasses (Fig. 9e-f). However, even the upper bound of the 95% confidence interval of the gradient of Cu vs. Ba in the fractionation-corrected glass compositions is >30× lower than predicted by this model (black rectangle, Fig. 9e-f). In contrast, the observed range of fractionation-corrected glass Cu concentrations (pink bar; Fig. 9a-b; triangles Fig. 9c-d) are only ~3× lower than predicted in this model. Changing the initial concentration of Cu in the source cannot resolve these discrepancies in both the gradient and the concentration of Cu. Sulfides are also exhausted within the melting interval at Kīlauea if $S_{i,\ Per}$ = 100 ppm. For $K_{D,Cu}^{sulf/melt}$=200, models with $S_{i,\ Per}$ = 100 ppm display highly positive gradients, and overestimate the Cu concentrations of primary melts (Fig. 9c, e). If $K_{D,Cu}^{sulf/melt}$=800, the model scenario matches observed gradients, but still overpredicts melt Cu contents.

It could be argued that a model with $S_{i,\ Per}$ =150 ppm and $K_{D,Cu}^{sulf/melt}$=800 would recreate observed Cu and Ba concentrations without exhausting sulfide. However, the calculated gradient for this model only passes through the very bottom of the observed 95% confidence interval (Supplementary Fig. 13). Additionally, based on the Kiseeva and Wood (2015) parameterization, $K_{D,Cu}^{sulf/melt}$ is very unlikely to be as high as 800. For the more realistic models with $K_{D,Cu}^{sulf/melt}$=200, the observed gradients can only be recreated if sulfides were present in the mantle source throughout the melting interval incorporated by the three primitive eruptions investigated in this study. Overall, the gradient of Cu vs. Ba provides a far more robust measure of the presence or absence of sulfide for the probably range of $K_{D,Cu}^{sulf/melt}$ in the Hawaiian mantle source, as it is far less to the choice of poorly constrained parameters such as Cu_i than absolute concentrations.

Based on the assumption that sulfides were present throughout the melting interval, the *minimum* S concentration of the Kīlauean mantle source may be estimated from the S concentration of primary melts (S_{prim}) and the extent of melting (F) using the equation S_{min}= S_{prim}* F. Assuming melt extents between F=0.07–0.09 (based on Ba concentrations; Supplementary Fig. A12), and primary S concentrations of 1600 ppm, the mantle source contains a minimum of ~110–140 ppm S. Placing further constraints on the source S content is challenging; as discussed above, for low values of $K_{D,Cu}^{sulf/melt}$ (e.g., 200), once sulfides are residual throughout the melting interval, the gradient between Cu and Ba provides no further discriminatory power (all models have gradients of ~0; Fig. 9e-f; Supplementary Fig. 11), and Cu concentrations in the melts are invariably a trade-off between S_i and Cu_i. More precise constraints on the S concentration of the Kīlauean mantle source will require better constraints on the concentrations of other chalcophile elements in the mantle (so that inversions can be performed for more than one element), as well as sulfide-melt partition coefficients, which not only vary with mantle temperature and the composition of mantle sulfides, but may also be sensitive to pressure.

4.2 Sulfide systematics during magma ascent and fractionation

Due to the increase in the $SCSS^{2-}$ with decreasing pressure, a melt that is sulfide-saturated in the mantle will generally become sulfide-undersaturated during its ascent towards the surface (Mavrogenes and O'Neill, 1999). This process was modelled by calculating the $SCSS^{2-}$ for mantle melts ascending along the olivine liquidus (after Matthews et al., 2016 using 39.16˚C/GPa; Putirka, 2008; Fig. 10a) for two mantle potential temperatures (T_p=1450˚C and 1650˚C). For each potential temperature, the trajectory of the hottest melt formed at the onset of melting and the coolest melt formed at the base of the lithosphere was modelled (Matthews et al., 2016; Fig. 10a). As in Fig. 7, the calculated sulfide composition in the S2017 model results in a decrease in the SCSS^{2-} with decreasing pressure (which is likely an artefact of the absence of suitable parameterizations to calculate sulfide compositions at mantle pressures). Using a fixed sulfide composition, the S2017 and O2020 models both show a similar rate of increase in the SCSS^{2-} until ~1 GPa, where the SCSS^{2-} in the O2020 model decreases (Fig. 10c). The paucity of experimental data collected at pressures between 100 kPa and 1 GPa (Smythe et al., 2017) makes it difficult to verify the validity of these different parametrizations at low pressure (see O'Neill, 2020). However, regardless of the exact model or potential temperature, this modelling demonstrates that at low pressures, the SCSS^{2-} is equal to, or exceeds the S contents of primary melts (Fig. 10c). Thus, melts forming from a sulfide-saturated source will be sulfide-undersaturated following their ascent through the thick Hawaiian lithosphere. The likely presence of S^{6+} species in primary melts will shift the SCSS$_{\mathrm{Tot}}$ to higher S contents than SCSS^{2-} models shown in Fig. 10, resulting in melts becoming sulfide undersaturated at even higher pressures. Similarly, if melts were to ascent along an adiabatic gradient instead of the olivine liquidus used in these models, the temperature decrease upon ascent would be smaller, resulting in higher values of the SCSS^{2-}, and the onset of sulfide undersaturation at higher pressures.

Following the injection of sulfide-undersaturated primitive melts into shallow crustal storage reservoirs at Kīlauea (~1-5 km depth; Cervelli and Miklius, 2003), a second episode of sulfide saturation may occur as a result of crystal fractionation. Recent work has concluded that the majority of erupted melts at Kīlauea are sulfide-undersaturated until ~2 wt% MgO (Ding and Dasgupta, 2018; Greaney et al., 2017; Helz et al., 2017). However, this view is difficult to reconcile with the ubiquitous presence of sulfides in the relatively primitive eruptions investigated in this study (Fig. 5), unless sulfides form during late stage processes such as quenching, rather than primary sulfide immiscibility (Stone and Fleet, 1991). We assess the possibility that sulfides form upon quench by comparing bulk sulfide compositions measured using EDS analysis to the predicted sulfide compositions from SCSS^{2-} models. Sulfides formed through primary sulfide immiscibility will progressively evolve towards more Cu-rich and Ni-poor compositions with increasing fractional crystallization. Conversely, sulfides formed during quench-induced segregation and cooling will show extreme compositional variability (Stone and Fleet, 1991; Fleet and Stone, 1990). The sulfide compositions predicted by SCSS^{2-} models were calculated for a liquid line of descent produced in Petrolog3 from the adjusted primary melt composition of Clague et al. (1991) at 1 kbar (Supplementary Fig. A3). Due to an absence of Fe redox measurements in high MgO Kīlauean melts (Fig. 8a), it is uncertain whether melts follow a redox buffer, or act as a closed system for oxygen during fractionation. To incorporate this uncertainty, we consider two fractionation paths which are consistent with melt inclusion Fe-XANES data (closed system, and buffered at ΔQFM+0.6; Fig. 8a). Melt Ni concentrations were modelled using $\mathrm{K_{D,Ni}^{ol/melt}}$ from Beattie et al. (1991), $\mathrm{K_{D,Ni}^{cpx/melt}}$ = 2.6 from Mysen (1978), and $\mathrm{K_{D,Ni}^{plag/melt}}$ = 0. Melt Cu concentrations were modelled using $\mathrm{K_{D,Cu}^{ol/melt}}$ = 0.1, $\mathrm{K_{D,Cu}^{cpx/melt}}$ = 0.21 (Greaney et al., 2017) and $\mathrm{K_{D,Cu}^{plag/melt}}$ = 0.14 (Bougault and Hekinian, 1974). To assess changes in sulfide chemistry during fractionation (and to compare measured sulfide compositions to those predicted by SCSS^{2-} models), the MgO content of the melt at the time of formation for each Kīlauean sulfide was estimated. Sulfides hosted in matrix glasses or embayments were allocated an equivalent melt MgO content equal to that of the host glass. For sulfides hosted in olivine crystals and melt inclusions, the forsterite content of the host olivine was compared to olivine compositions from the Petrolog3 model, and the sulfide was assigned the liquid MgO content at which the measured olivine composition fractionated. Contrary to the observations of Stone and Fleet (1991) that bulk sulfide compositions from Kīlauea Iki are highly variable, bulk sulfide compositions measured in this study show coherent changes in Cu and Ni with decreasing melt MgO contents, and relatively little chemical variability (Fig. 11a-b). Furthermore, the Ni and Cu contents of the sulfides fall between the predictions for the S2017 and O2020 SCSS^{2-} models. Coherent variations in sulfide compositions have also been reported for sulfides observed in the 1955 eruption (Helz and Wright, 1992). It is plausible that scatter in previously reported sulfide compositions from Kīlauea results from the analytical challenges associated with obtaining bulk compositions from EPMA spot analyses of exsolved sulfides. Thus, we conclude that observed sulfides are the result of primary sulfide fractionation.

Our hypothesis that sulfides form during primary sulfide saturation is supported by the presence of sulfides trapped within the cores of olivine crystals (Fig. 5a), often associated with small pockets of melt (Fig. 5f-h). These textural associations cannot be explained by quenching processes, or the formation of sulfides following melt inclusion entrapment (e.g. Hartley et al., 2017), as there is simply not enough Cu, Ni and S in these small pockets of melt to form sulfides of the observed sizes after the melt inclusion became a closed system (Supplementary Fig. A5). The attachment of sulfides to other silicate phases (e.g., Fig. 5c, f) suggests that sulfides have a stronger affinity for nucleation or attachment to silicate phases than the silicate melt (e.g. Fig. 5c, f). Their attachment to the boundary layer of a growing crystal likely accounts for their incorporation as inclusions within olivine crystals. This process may even trigger the formation of melt inclusions in a similar mechanism to that proposed for inclusions associated with chrome-spinels (Maaloe and Hansen, 1982). Overall, our chemical and textural observations of sulfides are consistent with their formation through primary sulfide saturation during differentiation, followed by their subsequent entrapment within growing crystals (often alongside spinels and silicate melt; Nadeau et al., 2010).

The occurrence of sulfides hosted in a wide variety of glass and olivine compositions (~6–14 wt% MgO) indicates that only a small amount of fractional crystallization of sulfide-undersaturated primary melts is required for silicate melts to become sulfide-saturated again during ascent. We assess the cause of this second stage of sulfide saturation by comparing fractionation trajectories for S (assuming S is incompatible in silicate phases) with $SCSS^{2-}$ model trajectories for the two Petrolog3 fractionation paths described above. The $SCSS^{2-}$ is sensitive to melt composition (predominantly the FeO content), temperature, pressure and the composition of co-existing sulfides (Smythe et al., 2017; O'Neill, 2020). During fractional crystallization at Kīlauea, olivine (+chrome-spinel) are the only silicate phases on the liquidus until 6.8 wt% MgO (Wright and Fiske, 1971). Over this fractionation interval, melt FeO contents remain approximately constant (Supplementary Fig. A3). Additionally, although $SCSS^{2-}$ models predict an increase in the ratio of Fe/(Fe+Cu+Ni) in sulfides, this ratio remains remarkably constant in measured bulk sulfide compositions (Fig. 11d). Thus, we fix this at 0.646 in all models. As magma storage (and fractionation) at Kīlauea is restricted to a narrow range of depths (~1–5 km; Cervelli and Miklius, 2003), the dominant control on the $SCSS^{2-}$ during olivine-only fractionation is the drop in temperature (which correlates strongly with the melt MgO content; Helz and Thornber, 1987).

Other than subtle changes in the MgO content at which clinopyroxene and plagioclase begin to crystallize, the closed system and buffered model show very similar major element systematics (Supplementary Fig. A3), so produce similar $SCSS^{2-}$ trajectories (Fig. 12a-b).These models intercept fractionation trajectories for S at high MgO (~16 wt% MgO). Below ~12 wt% MgO, the calculated $SCSS^{2-}$ (even accounting for the upper 1σ error envelope on the S2017 parameterization; pink shading) is significantly lower than the measured S contents in melt inclusions. As discussed in Section 4.1, this indicates that Kīlauea melts must contain S^{6+} species to increase the total solubility of S (Equation 1). We perform several corrections to account for the presence of S^{6+}. The first, and most simplistic, assumes that the S redox state remains constant throughout the fractionation interval at Kīlauea. Based on available S-redox measurements in submarine Hawaiian glasses, the proportion of S^{6+} may range from 0-30% (Fig. 8b). $SCSS_{Tot}$ models with 30% S^{6+} predict the onset of sulfide saturation at ~12 wt% MgO (consistent with textural observations. Fig. 11), and approximately recreate the upper observed limit of S contents in melt inclusions at lower MgO contents (Fig. 12c-d).

The proportion of S^{6+} can also be estimated from the experimental parameterizations of Jugo et al. (2010) and Nash et al. (2019; Equation 2-3). In contrast to the concerns in Section 4.1

that the pressure dependencies were not well enough constrained to calculate S^{6+} proportions during mantle processes, these parameterizations were calibrated at pressures relevant to fractionation processes in the shallow crust at Kīlauea. ΔQFM values for the Jugo et al. (2010) model, and Fe^{3+}/Fe_T ratios for the Nash et al. (2019) model were calculated from the Petrolog3 output, and melt temperatures were calculated using the geothermometer of Helz and Thornber (1987) . The closed system model shows a gradual increase in the Fe^{3+}/Fe_T ratio during olivine-only fractionation (due to the removal of Fe^{2+}-rich olivine; Carmichael and Ghiorso, 1990; Moussallam et al., 2016; Fig 8a). As clinopyroxene and plagioclase begin to fractionate, this ratio increases more rapidly per unit decrease in MgO. In contrast, the buffered model exhibits a constant Fe^{3+}/Fe_T ratio during olivine-only fractionation, followed by a slight decrease at lower MgO contents (Fig. 8a). As both the Jugo et al. (2010) and Nash et al. (2019) models predict a strong coupling between Fe and S redox states, the S^{6+}/S_T ratio, and by extension, the $SCSS_{Tot}$ trajectories are markedly different for the closed system and buffered model.

The S^{6+}/S_T ratio predicted by the Jugo et al. (2010) model for the closed system fractionation path increases from 0 to ~0.25 during olivine-only fractionation, and then rapidly increases towards 1 at <6 wt% MgO (dashed green line labelled J2010, Fig. 8b). In contrast, due to the dependency of the Nash et al. (2019) model on both temperature and Fe^{3+}/Fe_T, the S^{6+}/S_T ratio decreases somewhat during olivine-only fractionation (as the drop in temperature counteracts the increase in Fe^{3+}/Fe_T), and only starts to increase dramatically during clinopyroxene and plagioclase fractionation, where the increase in the Fe^{3+}/Fe_T ratio overwhelms the effect of dropping temperatures (dashed green line labelled N2019; Fig. 8b). $SCSS_{Tot}$ trajectories for the closed system model utilizing these different S^{6+}/S_T parameterizations both show a decrease in the $SCSS_{Tot}$ during olivine-only fractionation (although the drop is much more pronounced using the Nash et al. 2019 model due to the temperature-induced drop in the S^{6+}/S_T ratio), and a subsequent increase in the $SCSS_{Tot}$ at <6 wt% MgO (Fig. 12 e, g). The upper error bracket of the S2017 $SCSS_{Tot}$ model using the Jugo et al. (2010) S^{6+} parameterization predicts the onset of sulfide saturation at ~14 wt% MgO (consistent with textural observations), and does a reasonable job of recreating the upper limit of melt inclusion S contents (although a few melt inclusions have higher S contents than the model; Fig. 12e). However, use of preferred model values (red and blue lines) underestimate the S contents of melt inclusions (Fig. 12e). In contrast, preferred $SCSS_{Tot}$ model values using S^{6+}/S_T proportions from Nash et al. (2019) predict the onset of sulfide saturation at ~10 wt% MgO (later than textural observations), but do a good job of recreating the upper limit of melt inclusion S contents (Fig. 12g).

As the buffered model is fixed at QFM+0.6, the proportion of S^{6+}/S_T estimated using the Jugo et al. (2010) model (Equation 2) is constant throughout the fractionation interval (~0.11; Fig. 8b). In contrast, the Nash et al. (2019) model predicts a very rapid drop in S^{6+}/S_T due to dropping temperatures (blue line labelled N2019; Fig. 8b). The trajectory of the $SCSS_{Tot}$ using S^{6+}/S_T ratios from Jugo et al. (2010) is very similar to that in the closed system model until ~6 wt% MgO, where the slope of the $SCSS_{Tot}$ levels out in the buffered model (Fig. 12f vs. 12e), reflecting an approximately balance between an increase in the $SCSS^{2-}$ driven by increasing melt FeO content during plagioclase fractionation, and a decrease in the $SCSS^{2-}$ due to dropping temperatures. In contrast, the trajectory of the $SCSS_{Tot}$ using S^{6+}/S_T ratios calculated from Nash et al. (2019) is much steeper than in the closed system model during olivine-only fractionation (Fig. 12h vs. 12g), predicting very high $SCSS_{Tot}$ values in primitive melts, and the onset of sulfide saturation at ~8 wt% MgO (a poor match to our textural and chemical observations).

Clearly, more measurements of Fe and S redox states within melt inclusions with a wide range of MgO contents are needed to determine which of the six models accounting for S^{6+} species is most representative of the fractionation path at Kīlauea. Assessing the validity of the strong temperature sensitivity predicted by the Nash model is particularly important, and will require measurements of Fe-S redox in highly primitive melts (>12 wt% MgO). Overall, despite the differences between these models, all six predict that the onset of sulfide fractionation occurs at relatively high MgO contents (>>2 wt% MgO; Wallace and Anderson., 1998; cf. Greaney et al., 2017), supporting our textural and chemical observations that the vast majority of erupted Kīlauean melts were sulfide-saturated. These findings further support our inference that mantle melting occurred in the presence of residual sulfides, as melts generated in a mantle which had exhausted sulfide require large amounts of fractionation to intercept the $SCSS_{Tot}$ following ascent to low pressures (Liu et al., 2014). The simplest models, which utilize a fixed S^{6+}/S_T ratio during fractionation, recreate the onset of sulfide saturation at high MgO contents, and bracket the most S-rich melt inclusions (Fig. 12 c-d). Based on the absence of constraints for changes in Fe-S redox during differentiation (Fig. 8), we favour these simple model trajectories. The most significant deviation between the six $SCSS_{Tot}$ models occurs following the onset of plagioclase fractionation. The absence of sulfur (and other chalcophile element data) for melt inclusions or submarine glasses with MgO contents <6.8 wt%, reflecting a true paucity of erupted compositions which have differentiated significantly beyond olivine control at Kīlauea, makes “ground truthing” these different model scenarios challenging.

4.3 Sulfide saturation in lava lakes

The prevalent view at Kīlauea, that sulfides only saturate following extensive fractionation, is not supported by models of sulfide solubility, or textural observations of sulfide occurrence. This discrepancy may result from the focus of previous studies on chemical trajectories defined by samples collected from lava lakes (e.g., Greaney et al., 2017; Pitcher et al., 2009; Stone and Fleet, 1991). A comparison of the S contents of melt inclusions and matrix glasses clearly demonstrates that basaltic melts at Kīlauea degas >90% of their S during subaerial eruptions (~1600 ppm to ~135 ppm; Fig. 1b; Fig. 2a-b). Kīlauea Iki and Alae lava lakes formed by the ponding of S-poor melt within existing pit craters, followed by extensive fractionation (Wright et al., 1976). As the erupted melts filling these lava lakes have similar MgO contents to those examined in this study, it is reasonable to assume that these magmas were sulfide-saturated prior to their ascent to the surface. However, extensive degassing upon eruption would have caused the S content of the melt to fall well below the $SCSS_{Tot}$ (Fig. 12), driving the resorption of sulfides (Edmonds and Mather, 2017; Moore et al., 1980; Reekie et al., 2019). Subsequent fractionation within these lava lakes may then have proceeded under sulfide-undersaturated conditions.

We model the onset of sulfide saturation within the degassed melts ponding and fractionating within lava lakes by calculating the $SCSS^{2-}$ using major element data for variably evolved glasses from the Kīlauea Iki lava lake (Greaney et al., 2017; Fig. 1b). For simplicity, the amount of S^{6+} in the fractionating lava lake was assumed to be negligible, as extensive degassing of S upon eruption causes a significant drop in the Fe^{3+}/Fe_T ratio (Fig. 8a, Moussallam et al., 2016). The onset of sulfide saturation in Kīlauean lava lakes would occur when the S concentration in the lake exceeds the $SCSS^{2-}$. The evolution of S during progressive fractionation within the lake is uncertain; while the crystallization of silicate minerals drives melt S contents up, the presence of vesicles within lake lava samples and observations of gas release along drill holes suggests that lava lakes continued to lose volatiles during differentiation (Helz and Wright, 1983; Peck, 1978; Wright et al., 1976). To incorporate this uncertainty, we consider the interception of the regression lines for the calculated $SCSS^{2-}$ vs. MgO with the range of S contents in degassed glasses from Kīlauea Iki pumice (black histogram; Fig 1b; Sides et al., 2014a), and the S content measured in Alae lava lake (green line; Moore et al., 1980; Fig. 1b). These models predict that the third stage of sulfide saturation at Kīlauea will occur at ~2 wt % MgO, which is consistent with observations that Cu suddenly decreases at <2 wt% MgO in the Kīlauea Iki lava lake (Fig. 1a; Greaney et al., 2017).

This third stage of sulfide saturation has been attributed to the uptake of Fe^{3+} in Fe-Ti oxides (Greaney et al., 2017) driving S reduction in a mechanism similar to the “magnetite crisis” in arc basalts (Jenner et al., 2010). However, our modelling successfully predicts the onset of sulfide saturation without incorporating changes in redox state. Instead, the decrease in the $SCSS^{2-}$ correlates strongly with glass MgO content (Fig. 1b), which varies approximately linearly with temperature at Kīlauea (Helz and Thornber, 1987). This suggests that sulfide saturation within lava lakes at Kīlauea is driven by decreasing temperatures. Overall, while lava lakes provide useful insights into the plausibility of sulfide saturation following extensive degassing, they are clearly not representative of the onset of sulfide saturation in undegassed melts within crustal storage reservoirs.

4.4 Degassing of chalcophile elements

Aerosol measurements at Kīlauea reveal that, in addition to "conventional" volatile elements (e.g., CO_2, H_2O, S, Cl and F), the volcanic plume also contains considerable quantities of chalcophile elements (Edmonds et al., 2018; Mather et al., 2012). The extent to which an element degasses is represented by the emanation coefficient (Ɛ), which quantifies the proportion of an element lost to the gas phase:

$$Ɛ = \frac{[X]_i - [X]_f}{[X]_i} \text{ (equation 4)}$$

Where $[X]_i$ and $[X]_f$ are the concentrations of element X in the initial (undegassed) and final (degassed) melt respectively (Edmonds et al., 2018; Lambert et al., 1985). Previous petrological work investigating chalcophile degassing at various Hawaiian volcanoes have utilized suites of variably degassed submarine glasses to estimate emanation coefficients (e.g., Norman et al., 2004). These studies have only observed degassing trends for S (Ɛ=0.86–0.92), Re (Ɛ=0.5–0.74), Bi (Ɛ=0.44–0.45), and Cd (Ɛ=0.19–0.27). Additionally, as the glasses of Norman et al. (2004) are from different Hawaiian islands (Ko'olau and Moloka'i), it is difficult to deconvolve the effects of degassing from variations in the original chalcophile contents of these melts.

In this study, chalcophile element degassing was evaluated by comparing element concentrations in melt inclusions (which remain largely undegassed) and matrix glasses (which have extensively degassed; Fig. 3a). However, such comparisons rely on the assumption that melt inclusions are genetically related to their matrix glasses. Lithophile trace element ratios in olivine-hosted melt inclusions from the three rift eruptions investigated in this study show considerable overlaps, despite significant changes in the composition of the co-erupted matrix glass. This indicates that these melt inclusions were trapped from a variety of magma batches present within Kīlauea's plumbing system over centuries, and subsequently brought to the surface in an unrelated magma batch (Wieser et al., 2019, see also Tuohy et al., 2016). Only the 1971 summit eruption contains a crystal cargo that crystallized from the carrier liquid, permitting a direct comparison between melt inclusions and co-erupted glasses.

Fortunately, the presence of residual sulfides in the mantle source means that chalcophile element concentrations do not differ as much as lithophile element concentrations between different magma batches (Fig. 4). Thus, degassing can be assessed by comparing the matrix glasses and melt inclusions, considering the data from all eruptions together.

The concentrations in melt inclusions and matrix glasses of many chalcophile elements overlap (Loewen, 2013), making it difficult to determine whether a given element is degassed (Fig. 3d-f). We consider several possible criteria to robustly assess whether an element shows petrological evidence for degassing. The first criterion is based on the fact that gaseous observations indicate that Cl partially degasses at Kīlauea (Edmonds et al., 2009). Melt inclusion Cl contents overlap with and extend to higher values than matrix glasses, with the most S-rich (least degassed) inclusions generally having higher Cl contents (Fig. 3a). We classify a chalcophile element as showing evidence for subaerial degassing if a regression line between that element and S exhibits a higher R^2 value than Cl vs. S (R^2=0.13). This criterion classifies Se (R^2=0.90), Bi (R^2=0.34) and As (R^2=0.22) as degassed (Fig. 3).

The second criterion is based on a comparison using the ANOVA test of chalcophile element concentrations in melt inclusions and matrix glasses from the 1971 summit eruption (where melts trapped within crystals and the co-erupted matrix glass have similar trace element signatures; Wieser et al., 2019). Due to the small diameter of melt inclusions from this eruption, As and Se were not measured. An element was classified as degassed if $p<0.05$. This criterion only classifies Bi as degassed ($p=9\times10^{-4}$), with no distinguishable differences between matrix glasses and PEC-corrected melt inclusion compositions for Cu (p=0.08), Zn (p=0.66), Mo (p=0.77), Cd (p=0.27), In (p=0.90), Sn (p=0.28), Sb (p=0.21), W (p=0.60), or Tl (p=0.16), despite the fact that aerosol measurements indicate that these elements are present in the volcanic plume at Kīlauea (Mather et al., 2012).

The third criterion involves a comparison of the concentrations of chalcophile elements in Kīlauean and Lōi‘hi glasses. Lōi‘hi glasses were erupted at water depths of ~1000–4700 m (Pietruszka et al., 2011), so remain largely undegassed with respect to H_2O and S (Fig. 2a). For certain elements (e.g., Se, Bi, Cd), Lōi‘hi glasses plot with the least degassed Kīlauean melt inclusions, supporting the hypothesis that these elements have degassed from Kīlauean matrix glasses during subaerial eruptions. However, for certain elements (e.g., As), Lōi‘hi glasses sit at lower values than Kīlauean glasses, suggesting that Lōi‘hi and Kīlauea magmas may have slightly different chalcophile element signatures (perhaps due to differences in the mantle source, or the fact that Lōi‘hi glasses have experienced clinopyroxene fractionation).

To reconcile the apparent discrepancy between aerosol and petrological measurements of chalcophile element degassing, the expected drop in the concentration of each chalcophile element from the least degassed melt inclusions (S ~1600 ppm) to the average composition of degassed matrix glasses (S ~135 ppm) was calculated using the X/S ratios measured in the 2008 summit plume (Mather et al., 2012). For many chalcophile elements, the expected drop in concentration due to degassing is far smaller than the analytical precision of in-situ melt inclusion measurements. For example, even the minimum 2σ variation in the LA-ICP-MS signal during melt inclusion ablation (calculated in Iolite) is ~130× larger than the predicted loss of Cu during degassing (~5× for Bi and Cd, 12× for Pb, 31× for Zn, 167× for Mo). It is perhaps unsurprising that the only element that shows clear petrological evidence for degassing is Se (analytical precision ~0.1× the expected loss during degassing).

While the degassing of most chalcophile elements is obscured by analytical noise and natural variability in melt compositions, a crucial finding of this study is the excellent correlation between S and Se, indicating that these elements are degassing concurrently (Fig. 3b, R^2=0.90). Extensive degassing of Se during subaerial eruptions is consistent with aerosol measurements at Kīlauea (Crowe et al., 1987; Edmonds et al., 2018; Mather et al., 2012) and whole rock analyses of lavas from Antuco, Chile (Cox et al., 2019). However, in subaqueous eruptions (e.g., Lōiʻhi, MORB and oceanic plateau basalts), Se is thought to be less volatile than S and is often used to reconstruct the behaviour of S prior to degassing (Brenan, 2015; Jenner et al., 2015, 2012, 2010; Patten et al., 2013; Reekie et al., 2019). The preservation of high Se contents in Lōiʻhi glasses erupted at depths >1000 m indicates that the onset of Se degassing takes place at pressures of <0.1 kbar. Experimental work assessing the volatility of Se is ambiguous. During preparation of glass reference materials, Se is retained while S is lost (Jenner et al., 2009; Jochum et al., 2006). Yet, experiments on sulfides in the Se-S system (Helmy and Fonseca, 2017), and on chondritic meteorites (Wulf et al., 1995), demonstrate that Se has a similar volatility to S. Thus, although the exact cause of Se degassing at Kīlauea is beyond the scope of this study, we caution that the assumption that Se is less volatile than S may be invalid at low pressures. As metal emissions for Se at arc volcanoes are elevated above those at Kīlauea (Edmonds et al., 2018), it seems likely that Se degasses during subaerial eruptions in a wide variety of tectonic settings.

4.5 Sulfide Resorption during magma degassing

The strong partitioning of S into the gas phase during ascent and eruption causes melt S contents to drop, destabilizing sulfide liquids (Edmonds and Mather, 2017; Gerlach and Nordlie, 1975). At hotspot volcanoes, emanation coefficients calculated from aerosol measurements of volcanic plumes have been shown to broadly correlate with sulfide-silicate melt partition coefficient (Edmonds et al., 2018). This, along with literature observations of sulfides attached to bubbles, has led to suggestions that chalcophile elements held within sulfides are directly transferred to the gas phase during sulfide resorption (Mungall et al., 2015; Nadeau et al., 2010). Alternatively, the quantity of chalcophile elements released into the gas phase may depend on the three-way partitioning between sulfide, melt and vapour (Edmonds et al., 2018).

The near-absence of sulfides in matrix glasses from subaerial eruptions at Kīlauea, but presence of sulfides as inclusions in silicate minerals, is convincing evidence for sulfide resorption (Gerlach and Nordlie, 1975; Moore et al., 1980; Fig. 5). Further evidence is provided by the presence of resorbed features (~20 µm in size) in degassed matrix glasses, which consist predominantly of Fe and O, with small regions of Cu-S rich material (~1 µm; Fig. 6; Supplementary Fig. A8). Their chemistry and texture is highly indicative of the breakdown of sulfides to form Fe-oxide phases (e.g., magnetite) which are metal poor (Berlo et al., 2014; Edmonds and Mather, 2017; Nadeau et al., 2010). Only sulfides which are isolated from the degassing melt, including those trapped within olivine crystals, melt inclusions, and S-rich embayments, survive syn-eruptive degassing (Fig. 5a-h).

However, differences in chalcophile element concentrations in melt inclusions and matrix glasses do not support a model whereby sulfide breakdown releases chalcophile elements “almost quantitatively” into the gas phase (Mungall et al., 2015). Firstly, there is no correlation between sulfide-melt K_Ds and emanation coefficients estimated from comparisons of melt inclusion and matrix glass concentrations (Fig. 3; Fig. 13). Our emanation coefficients for Cd, Bi and S are remarkably similar to those estimated by Norman et al. (2004), and overlap with those calculated from the X/S ratios in the 2008 plume for Cu, Ni, Cd, and Se (Mather et al., 2012; Fig. 13). These published emanation coefficients also show no correlation with sulfide-melt K_Ds. Secondly, comparisons of melt inclusion and matrix glass Cu contents provide very strong evidence that sulfides do not release their chalcophile element cargo directly into the gas phase. While aerosol measurements indicate that Cu partially degasses upon eruption (Edmonds et al., 2018; Mather et al., 2012), a significant proportion of melt inclusions have lower Cu contents than matrix glasses (Fig. 2c, 3f, 14a-b; Loewen, 2013). This is the opposite trajectory to that expected from degassing, giving Cu a negative emanation coefficient (Fig. 13). Additionally, despite textural evidence for sulfide fractionation, glass Cu and MgO contents follow trajectories consistent with sulfide-undersaturated fractionation (Fig. 2c-d).

The compositional differences between melt inclusions and matrix glasses are most obvious in the 1971 summit eruption, where melt inclusions and co-erupted matrix glasses have similar trace element signatures (Wieser et al., 2019). The PEC-corrected Ni and Cu contents of these melt inclusions follow trajectories consistent with the removal of sulfides with Ni and Cu contents estimated from the regression lines shown on Fig. 11a-b using PEC-corrected MgO contents of 8.4 wt% (black line; Fig. 14a). In contrast, matrix glasses mostly plot along the sulfide-free fractional crystallization trajectory (red line; Fig. 14a). The trend towards low Cu and Ni concentrations in melt inclusions indicates that olivine crystals trapped pockets of melt over a period in which sulfide liquids were progressively forming and depleting the melt of Ni and Cu. In order to produce the high Cu and Ni concentrations of matrix glasses, the resorption of sulfides upon eruption must have released almost all of the Ni and Cu held within sulfide liquids back into the melt. If the Cu (and Ni) entered the gas phase directly, matrix glasses would plot with the most Cu and Ni depleted melt inclusions (Fig. 14a). These trends indicate that sulfides remained in the melt, such that they could be resorbed upon eruption. As the high density of sulfide droplets should result in their fractionation from the melt once they grow to a critical size, the involvement of sulfides in volcanic degassing has been attributed to the attachment of sulfide melts onto vapour bubbles, producing a compound drop with elevated buoyancy (Edmonds and Mather, 2017; Mungall et al., 2015). Interestingly, we also observe the attachment of sulfide globules onto the faces of olivine crystals (Fig. 5c). The remobilization of settled olivine crystals (Wieser et al., 2020, 2019) could provide an additional mechanism by which fractionated sulfides can participate in syn-eruptive degassing.

Although the melt inclusion record in the other three eruptions is complicated by the fact that host olivines trapped a diverse range of melt compositions present in the plumbing system over centuries, when all four eruptions are considered together, melt inclusions form a wedge towards lower Cu and Ni contents that is bracketed by fractionation lines for predicted sulfide compositions at ~6.2 and ~14.3 wt% MgO (Fig. 14b). This indicates that sulfide resorption upon eruption is near-ubiquitous process at Kīlauea. The presence of a few melt inclusions with slightly higher Cu and Ni contents than matrix glasses (Fig. 14a-b; Fig. 2c-d) could reflect the true fractionation of a small quantity of sulfide melt (~0.02%), or incomplete resorption of sulfides upon eruption (suggested by the presence of small quantities of Cu-S rich material within resorbed FeO-rich features in matrix glasses, and the presence of sulfides armoured within crystals; Fig. 5; Fig. 6; Supplementary Fig. A8). The absence of correlation between Cu, Ni, and the amount of PEC (Fig. 14, Supplementary Fig. A14) provides further support that sulfides were heterogeneously entrapped during the formation of melt inclusions (Nadeau et al., 2010), rather than forming after melt inclusion entrapment (e.g., Hartley et al., 2017).

Chalcophile systematics in Lōiʻhi glasses further support our assertion that the Cu concentrations of melt inclusions and glasses at Kīlauea record sulfide resorption upon eruption. Unlike Kīlauean glasses, Lōiʻhi glasses show a positive correlation between Cu and MgO (Fig. 1c; R^2=0.44) and Cu and Ni (Fig. 14b; Supplementary Fig. A4; R^2=0.4), which is indicative of sulfide fractionation. Furthermore, abundant sulfides (0.3-10% vol) have been reported in Lōiʻhi xenoliths (Roedder, 1983), and we observe relatively abundant, spherical sulfides within Lōiʻhi matrix glasses, providing strong textural evidence that Lōiʻhi magmas were sulfide-saturated. The lack of syn-eruptive degassing of S during subaqueous eruptions at Lōiʻhi preserved textural and chemical evidence for sulfide removal. Thus, these samples provide a vital analogue for the evolution of sulfides within Kīlauean melts before the onset of subaerial degassing.

The behaviour of Se allows further investigation of the relationship between sulfide resorption and the degassing of chalcophile metal species. In the previous section, the excellent correlation between S and Se (Fig. 3b) was interpreted to represent syn-eruptive degassing of elements with a similar volatility. However, the compound drop theory suggests that Se could be released directly from sulfides into the gas phase (Mungall et al., 2015). Thus, we entertain the possibility that the S-Se trajectory defined by melt inclusions and matrix glasses represents the removal of Se and S in the sulfide phase. The removal of sulfides with 30 wt% S, and Se contents calculated from the likely range of $\mathrm{K}_{\mathrm{D,Se}}^{\mathrm{sulf/melt}}$ (271 – 1012; Brenan, 2015; Patten et al., 2013) was modelled for the subset of melt inclusion and glass data with Se data. While sulfide removal with $\mathrm{K}_{\mathrm{D,Se}}^{\mathrm{sulf/melt}}$=271 approximately recreates the observed trajectories, the low Se concentrations of matrix glasses require removal of >0.4 wt% sulfide (Fig. 14c). Removal of this quantity of sulfides is inconsistent with observed trends in Cu vs. S space for the same subset of melt inclusions and glasses (for $\mathrm{K}_{\mathrm{D,Cu}}^{\mathrm{sulf/melt}}$=380–1754; Fig. 14d). Consequently, as the combined systematics of Cu, Se and S cannot be recreated by the removal of sulfide liquids, the excellent correlation of S and Se must result from syn-eruptive degassing. This is further supported by the fact that Lōiʻhi glasses, which contain visible sulfides, still have Se concentrations plotting close to the least degassed melt inclusions at Kīlauea (Fig. 3b).

These observations provide new insights into the relative importance of vapour-sulfide, vapour-melt, and sulfide-melt partitioning in controlling the chalcophile element budget of volcanic plumes. Sulfide resorption releases chalcophile elements into the silicate-melt-vapour system, which then become further partitioned between vapour and melt (Fig. 15d). This is best demonstrated by comparing the behaviour of Cu and Se. While sulfide resorption leads to the release of large quantities of Cu (>100 ppm; Fig. 14a-b), almost all of this Cu ends up back in the melt, likely due to its relatively low volatility in Kīlauean magmas (X/S ratios measured in the 2008 Kīlauean plume indicate that only ~0.01% of Cu degasses; Mather et al., 2012; Fig. 13). In contrast, the formation of a relatively small quantity of sulfide liquid (~0.12 wt%; Fig. 14b) does not significantly deplete the concentration of Se in the melt (~0.1 ppm; red diamond, Fig. 14c) Instead, the large release of Se upon eruption largely represents direct degassing of Se from the silicate melt due to its high volatility (~0.1-0.15 ppm; Fig. 14c), with the ~0.1 ppm of Se released during sulfide resorption likely being partitioned between the vapour-melt system, rather than directly entering the vapour phase (Fig. 14c).

The resorption of sulfides upon eruption provides a significant, but previously unquantified flux of S to the atmosphere during Kīlauean eruptions. The spread of melt inclusion Ni and Cu contents relative to matrix glasses indicate that 0.06-0.2 % sulfide resorption may occur upon eruption (Fig. 14a-b), accounting for the release of an additional 180–600 ppm of S (as measured sulfides contain ~30 wt% S). This represents an additional source of error when using the "petrological method" in basaltic systems to quantify total S release (in addition to uncertainty in erupted lava volumes). This source of error can be circumvented if the Cu-Ni-S systematics of melt inclusions are carefully evaluated when choosing S concentrations to compare to co-erupted matrix glasses. The best constraint on the S release during eruptions is provided by melt inclusions with Cu and Ni concentrations overlapping the co-erupted matrix glasses. For example, in the 1971 summit eruption, these have PEC-corrected S concentrations between 1360-1425 ppm. Accounting for the incomplete degassing of basaltic melts (1971 matrix glasses have average S contents of 121 ppm), these measurements suggest that ~1240–1300 ppm of S was released. Using the maximum PEC-corrected S content at high Cu contents of the entire database (~1600 ppm), and the average glass S content (135 ppm), S release during more primitive eruptions than the 1971 summit eruption could reach 1465 ppm. SO_2 emissions at Kīlauea have been used to calculate lava effusion rates (Sutton et al., 2003, 2001) using estimates of S release from C/S ratios measured in volcanic gases (e.g., 861 ppm - Greenland, 1984 and Greenland et al., 1988; 745 ppm - Sutton et al., 2003). Our estimates of S release are significantly higher than these previous estimates, highlighting the importance of detailed petrological work on specific eruptions to accurately constrain lava effusion rates.

5. Conclusions

Chalcophile element behaviour at Kīlauea Volcano, Hawai'i, is predominantly controlled by three separate stages of sulfide saturation, combined with the effects of sulfide resorption and degassing upon ascent to the site of eruption. The decoupled variability of chalcophile and lithophile elements during mantle melting in primitive samples (>6.8 wt% MgO) indicates that the concentration of chalcophile elements in Kīlauea's mantle source are buffered by the presence of residual sulfide (Fig. 15a). These residual sulfides, combined with the presence of S^{6+} in primary melts, are responsible for the high S contents of primary Kīlauean melts (1387–1600 ppm). The increase in sulfide solubility with decreasing pressures as primary melts ascend through the thick Hawaiian lithosphere results in crustal magma chambers being supplied with sulfide-undersaturated melts (Fig. 15b). The occurrence of sulfides within primitive olivines, combined with the results of $SCSS_{Tot}$ modelling, indicates that a second stage of sulfide saturation within the crust occurs after relatively small amounts of crystal fractionation (~10–14 wt% MgO; Fig. 15c).

Syn-eruptive degassing of S drives sulfide undersaturation of previously saturated magmas, resulting in the resorption of sulfides in contact with the degassing host glass (Fig. 15d). This releases Cu, Ni, S and other chalcophile elements into the vapour-melt-(sulfide) system. Elements with high vapour-melt partition coefficients residing predominantly in the melt phase (e.g., S, Se) enter the gas phase, while elements with lower vapour-melt partition coefficients (e.g., Ni, Cu) predominantly remain in the melt. The resorption of sulfides within matrix glasses and the release of their chalcophile element budget back into the melts obscures the textural and chemical record of sulfide saturation in matrix glasses. The coincidence of Cu-MgO and Cu-Ni systematics in matrix glasses with the trends predicted from sulfide-undersaturated fractionation demonstrates that the vast majority of immiscible sulfide liquids participated in the degassing process; perhaps due to their attachment to buoyant vapour bubbles, or remobilized olivine crystals. Fortunately, the chalcophile element systematics within melt inclusion populations (which are isolated from the late stage release of chalcophile elements into the melt), along with the preservation of visible sulfides within olivine crystals, melt inclusions, and undegassed embayments, faithfully record the fractionation of sulfides.

Previous studies investigating chalcophile element systematics have focused on lava lakes, which form through the ponding and fractionation of degassing melt within pre-existing pit craters. This has led to suggestion that sulfide saturation at Kīlauea only occurs after significant amounts of crystal fractionation (~2 wt% MgO). We demonstrate that the loss of S to the gas phase upon eruption resulted in previously sulfide-saturated magmas becoming sulfide undersaturated once more. Only following significant amounts of cooling and fractionation do melts reach a third phase of sulfide saturation. This phase is unique to the fractionation path taken by degassed melts, and not representative of the evolution of undegassed melts in crustal magma chambers (Fig. 15d).

Author Contributions

PW prepared and analysed the Kīlauean melt inclusions, glasses and sulfides by EPMA and EDS. PW performed LA-ICP-MS analyses under the guidance of FJ and BK. FJ analysed the Lōiʻhi glasses. PW interpreted the data and wrote the manuscript with help from all authors.

Acknowledgements

We thank Callum Reekie, Duane Smythe and Hugh O'Neill for helpful discussions about sulfide saturation (and the importance of S^{6+} corrections in particular); Giulio Lampronti and Iris Buisman for help collecting EDS and EPMA data; John Craven and Sally Gibson for providing sulfide standards, Michael Garcia and Aaron Pietruszka for supplying the Lōiʻhi samples. Isobel Sides (funded by a Natural Environment Research Council [NERC] studentship) and Don Swanson (U.S. Geological Survey) collected the Kīlauean samples used in this study. PW is funded by NERC DTP studentship NE/L002507/1. BK is funded by NERC grant 'From Arc Magmas to Ore Systems (FAMOS): a Mineral Systems Approach (NE/P017045/1). FJ acknowledges technique development funding from the NERC grant 'Mantle volatiles: processes, reservoirs and fluxes (NE/M000427/1). The authors thank Paul Wallace, Clifford Patten, and Yuan Li for helpful reviewers which substantially increased the clarity of the manuscript.

Figures and Captions

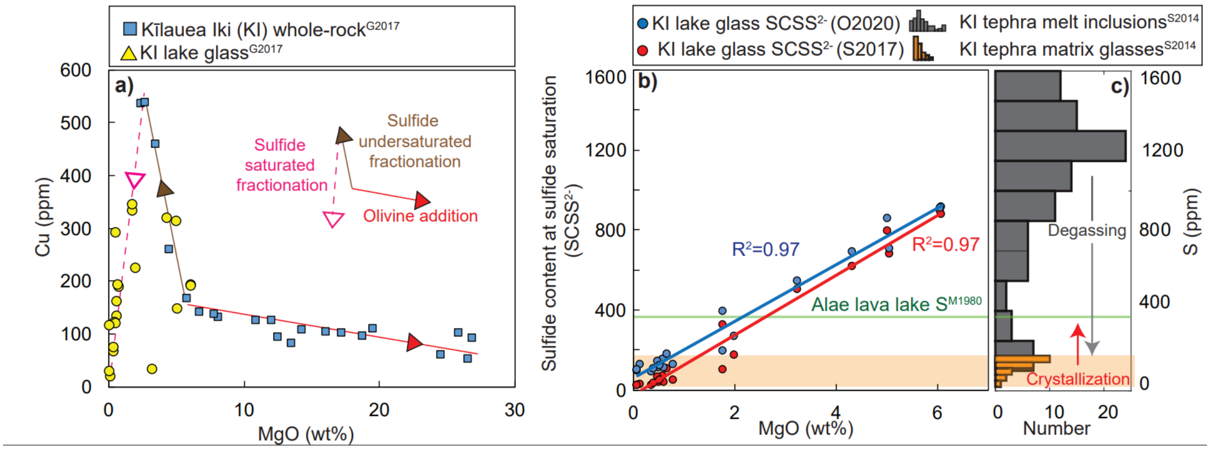

Fig. 1 – Chalcophile element behaviour in the Kīlauea Iki lava lake. **a)** Whole rock measurements from Kīlauea Iki define olivine-addition trends between ~27 and 7 wt% MgO. Whole-rock and glass measurements show a drastic increase in Cu between ~7 and 2 wt% MgO, followed by a rapid decrease at <2 wt% MgO (Greaney et al., 2017). The approximate vectors producing variability in Cu vs. MgO space are overlain. **b)** Calculated sulfide concentration at sulfide saturation ($SCSS^{2-}$) for the Kīlauea Iki lava lake glass compositions of Greaney et al. (2017) using the S2017 and O2020 models (with Fe^{3+}/Fe_{Tot} fixed at 0.1, no S^{6+}). **c)** Degassing upon eruption causes melt S contents to drop from the high concentrations observed in Kīlauea Iki melt inclusions (PEC-corrected; grey histogram; Sides et al., 2014a) to the low concentrations observed in matrix glasses (Kīlauea Iki scoria; orange histogram and bar; Sides et al., 2014a). These degassed melts have significantly

lower S contents than the SCSS^{2-}, driving sulfide resorption. Eventually, the drop in temperature with decreasing MgO content results in the SCSS^{2-} re-intercepting the S concentration of the melt (which probably lies between the S content measured in Kīlauea Iki pumices and that measured in a fractionated glass from Alae lava lake; Moore et al., 1980; Sides et al., 2014a). Thus, fractionation in lava lakes initially proceeds under sulfide-undersaturated conditions, producing the rapid increase in Cu contents with decreasing MgO contents between 7-2 wt% MgO (**a**). Following extensive fractionation (~2 wt% MgO), the ponded melt becomes sulfide-saturated once more, causing the rapid downturn in Cu (**a**). Crucially, these trajectories in Cu-MgO space are only characteristic of fractionation of degassed melt (where the S concentrations of melts have dropped significantly below the SCSS^{2-}).

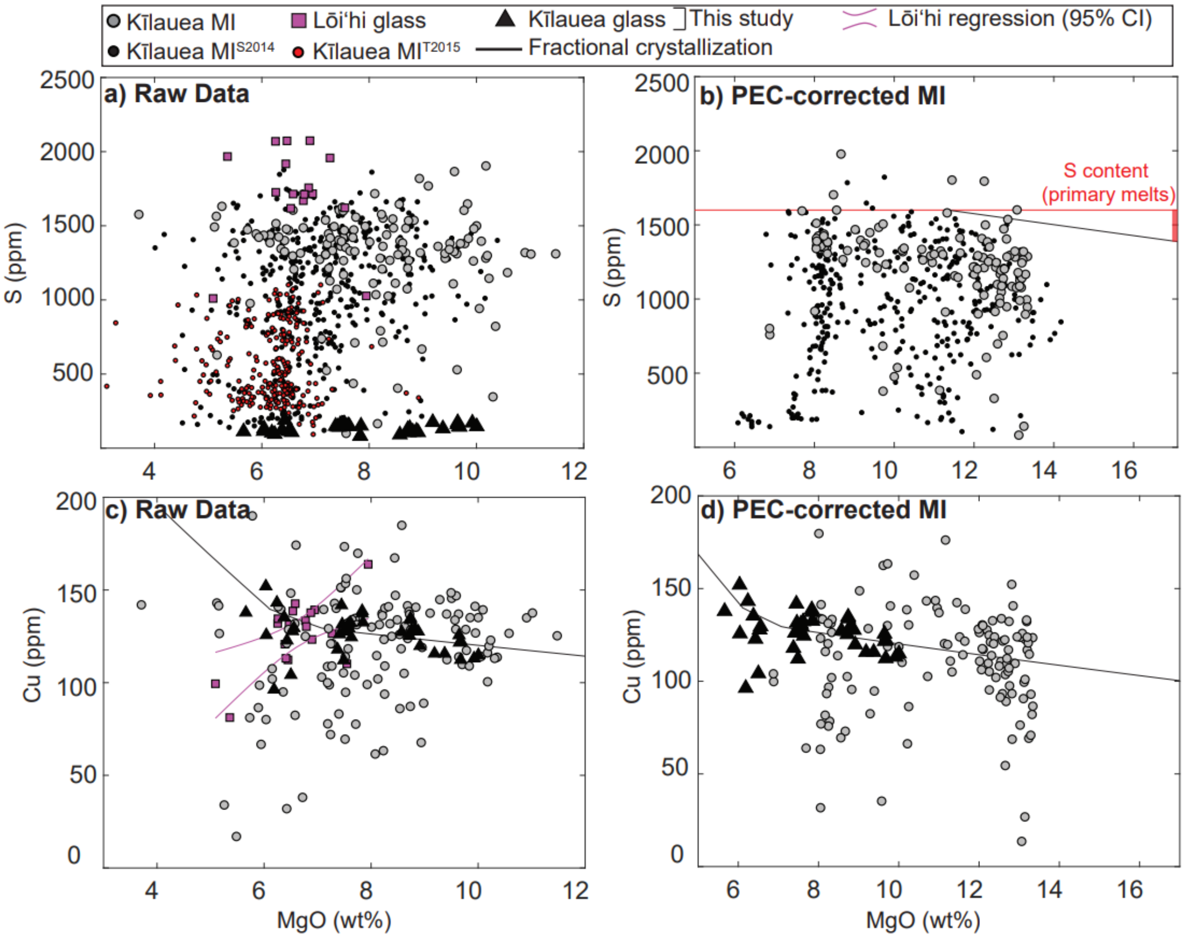

Fig. 2 –Cu, S and MgO systematics. **a)** S concentrations of Kīlauean melt inclusions, matrix glasses, and submarine matrix glasses from Lōiʻhi. Literature melt inclusion data for Kīlauea from Sides et al. (2014a,b; black dots) and Thornber et al. (2015; red dots) are also shown (all melt inclusion data is uncorrected for PEC). **b)** Melt inclusion S and MgO systematics following a correction for post-entrapment crystallization (using the "Olivine MI" tool in Petrolog3). Estimated S concentrations of primary melts are indicated with a pink bar. The

upper limit (1600 ppm) effectively brackets the vast majority of S-rich melt inclusions, while the lower limit (1387 ppm) was calculated by extrapolating back along olivine fractionation trends from 1600 ppm at 11.3 wt% MgO to an reasonable upper limit for the MgO content of primary melts (~17.1 wt% MgO) assuming S was entirely incompatible during olivine fractionation. **c)** Kīlauean matrix glasses show a slight increase in Cu contents with decreasing MgO, while Lōiʻhi glasses show a decrease in Cu over the same MgO interval. Uncorrected melt inclusions with <10 wt% MgO plot alongside, and slightly above Kīlauean matrix glasses, while more evolved inclusions predominantly plot below matrix glasses. **d)** Following a correction for PEC ($\mathrm{K}_{\mathrm{D,Cu}}^{\mathrm{ol/melt}}$ = 0.1), melt inclusions form a cluster at ~13 wt% MgO, plotting on the fractionation trajectory defined by matrix glasses (black lines), although a number of inclusions lie significantly below this line. The fractional crystallization model for Cu was calculated from the Petrolog3 fractionation path described in the main text (QFM+0.6; $\mathrm{K}_{\mathrm{D,Cu}}^{\mathrm{ol/melt}}$ = 0.1, $\mathrm{K}_{\mathrm{D,Cu}}^{\mathrm{cpx/melt}}$ = 0.21; Greaney et al., 2017; $\mathrm{K}_{\mathrm{D,Cu}}^{\mathrm{plag/melt}}$ = 0.17; Bougault and Hekinian, 1974).

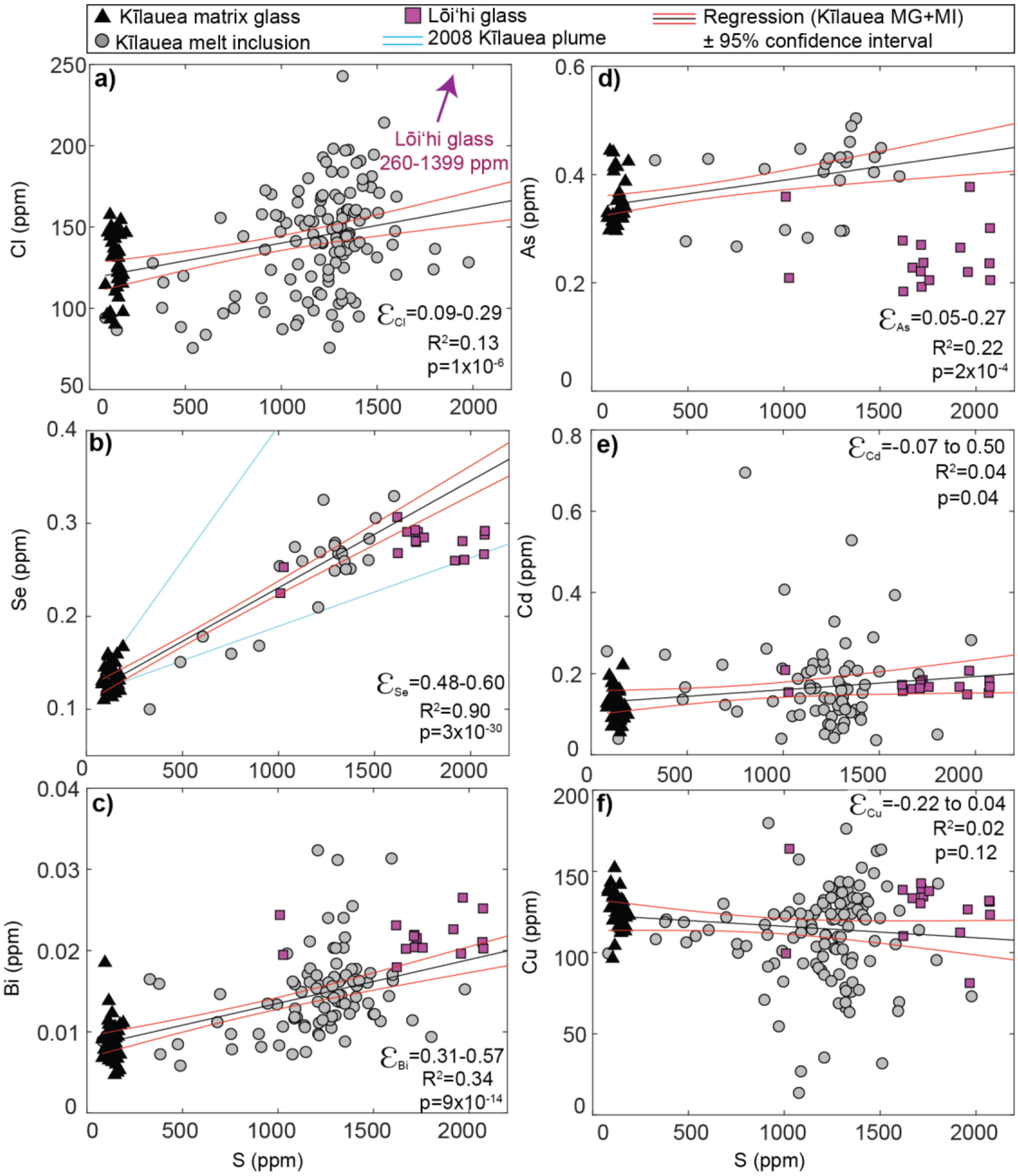

Fig. 3 – Assessing chalcophile element volatility. **a-f)** Plots of various chalcophile elements (and Cl) against S provide insights into the behaviour of chalcophile elements during subaerial degassing. Regressions through the combined Kīlauea dataset (matrix glasses and melt inclusions from all 4 eruptions) are shown with 95% confidence intervals. The upper and lower limits of the initial and final concentrations of each element used to calculate emanation coefficients (Ɛ) were estimated from the 95% confidence intervals of the regression lines with S_i=1387–1600 and S_f=135. Subaqueous Lōi'hi glasses have concentrations similar to those of the most undegassed Kīlauean melt inclusions for several elements (Se, Bi, Cd). PEC-corrected concentrations are shown for melt inclusions, assuming that all elements except Cu ($K_{D,Cu}^{ol/melt}$ = 0.1) are entirely incompatible in olivine. Note, that the y axis in **a)** has been cropped to emphasize the magnitude of Cl variation at Kīlauea, Lōi'hi glasses have Cl concentrations

up to 1399 ppm. The range of S/Se ratio observed in the 2008 summit plume are shown in **b)** to demonstrate that the emanation coefficient of Se derived from petrological measurements is consistent with aerosol measurements (Mather et al., 2012). A full comparison of our emanation coefficients and those of Mather et al. (2012) is shown in Fig. 13.

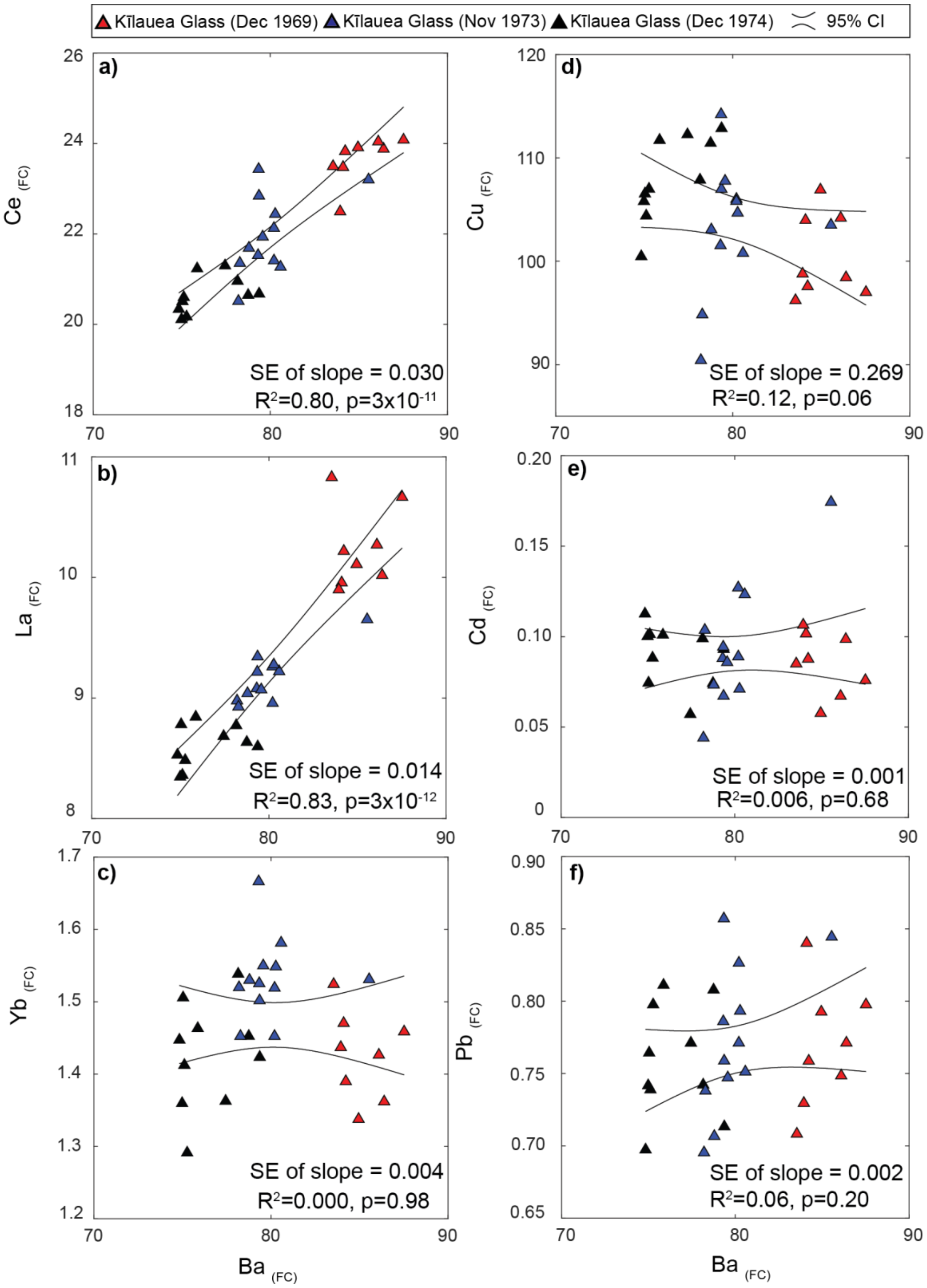

Fig. 4 –Fractionation-corrected trace element concentrations in matrix glasses which have not fractionated beyond olivine control. **a-b)** La and Ce show strong positive correlations with Ba. **c-f)** In contrast, Yb, Cu, Cd and Pb show very weak correlations with Ba. Trace element contents were corrected for fractional crystallization back to 16 wt% MgO assuming all elements except Cu ($K_{D,Cu}^{Ol/melt}$ = 0.1) are perfectly incompatible in olivine**.** Note, that the choice

of primary MgO content does not affect the observed correlations. The 95% confidence intervals on linear regressions through the data are shown, along with the standard error of the slope (and other statistical measures).

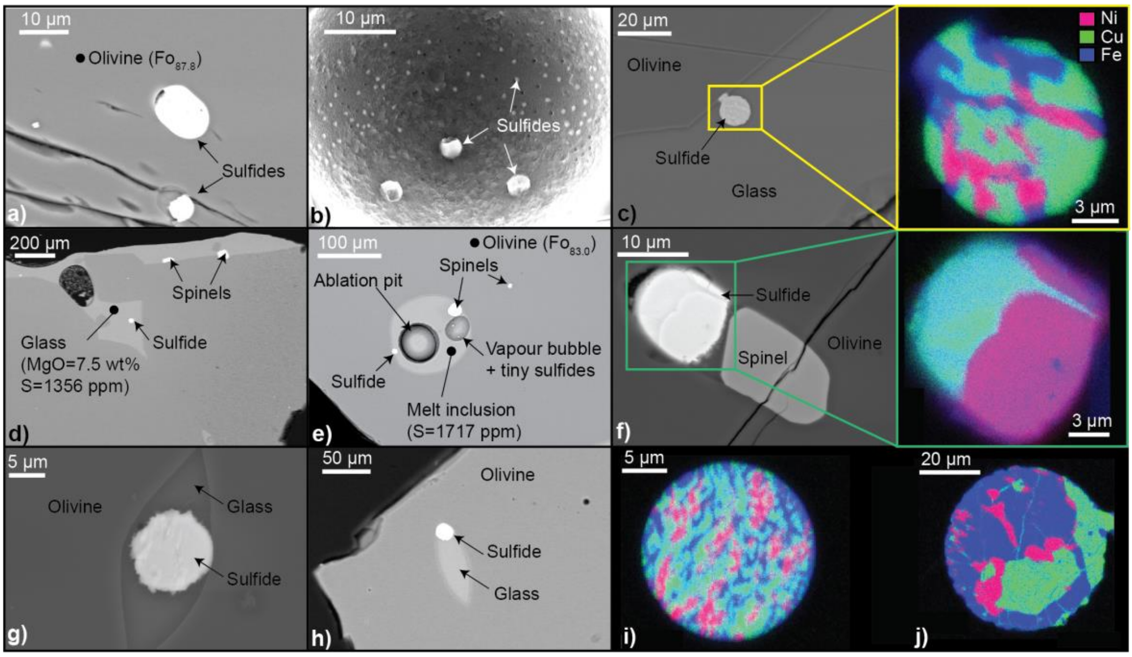

Fig. 5 - Textural and chemical characteristics of Kīlauean sulfides revealed with BSE and EDS mapping. **a)** Sulfides are commonly hosted as inclusions within olivine crystals. **b)** Sulfides with a bimodal size distribution within the wall of a matrix glass vesicle. **c)** Sulfide attached to an olivine crystal within a relatively open embayment. EDS maps show that this sulfide consists of exsolved Fe, Ni and Cu-rich phases. **d)** Sulfide within an open, but largely undegassed embayment (S=1356 ppm). **e)** Sulfide within a melt inclusion, which also contains a vapour bubble with tiny <1 µm sulfides embedded in the bubble wall. **f)** Sulfide trapped within an olivine crystal along with a spinel, and a small amount of melt. EDS maps show that this sulfide has exsolved 2 main phases at a relatively course scale. **g-h)** Sulfides trapped within small melt inclusions hosted in olivine crystals. **i-j)** EDS maps of sulfides showing fine and coarse exsolution of Cu-Ni-Fe rich phases (BSE images not shown)

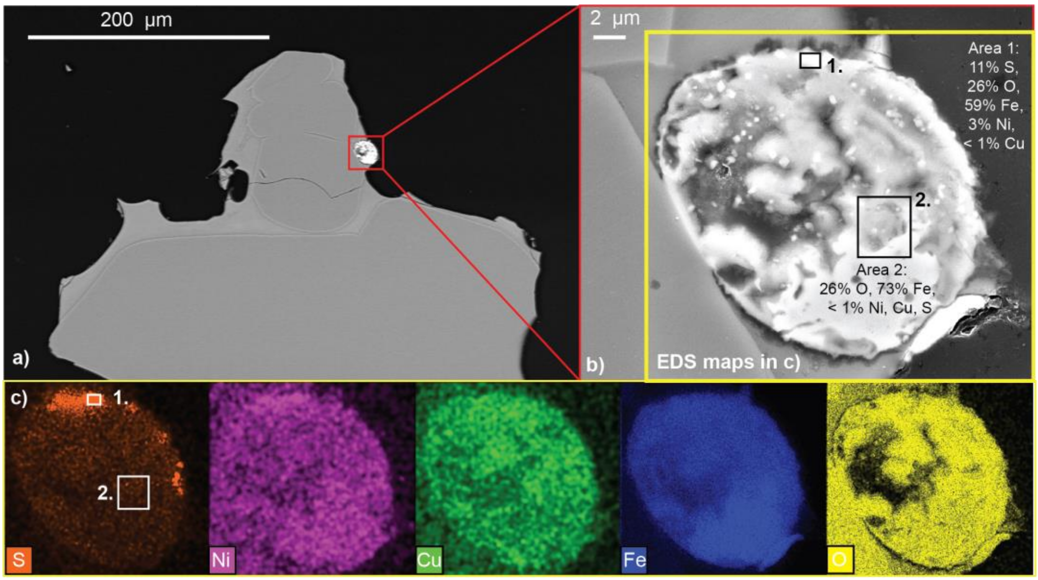

Fig. 6-Textural and chemical characteristics of resorbed Kīlauean sulfides **a)** A BSE image of a resorbed sulfide attached to an olivine crystal. **b**) BSE image of the sulfide (red square in a), which shows considerable textural complexity compared to the pristine sulfides shown in Fig. 5. **c)** EDS maps of the area indicated by the yellow rectangle in **b**. Most of the resorbed sulfide is very Ni and Cu poor, with counts only just above background (e.g., area 2, compare with Fig. 5 **c**,**f**, **i**, **j**). Small regions of more S (and Ni)-rich material survive (e.g. area 1). The approximate composition of the areas indicated with black rectangles in **b)** are displayed in wt%. Resorbed sulfides contain considerable quantities of O (~26 wt%), compared to pristine sulfides which generally contain <4 wt% O (Supplementary Fig. A9).

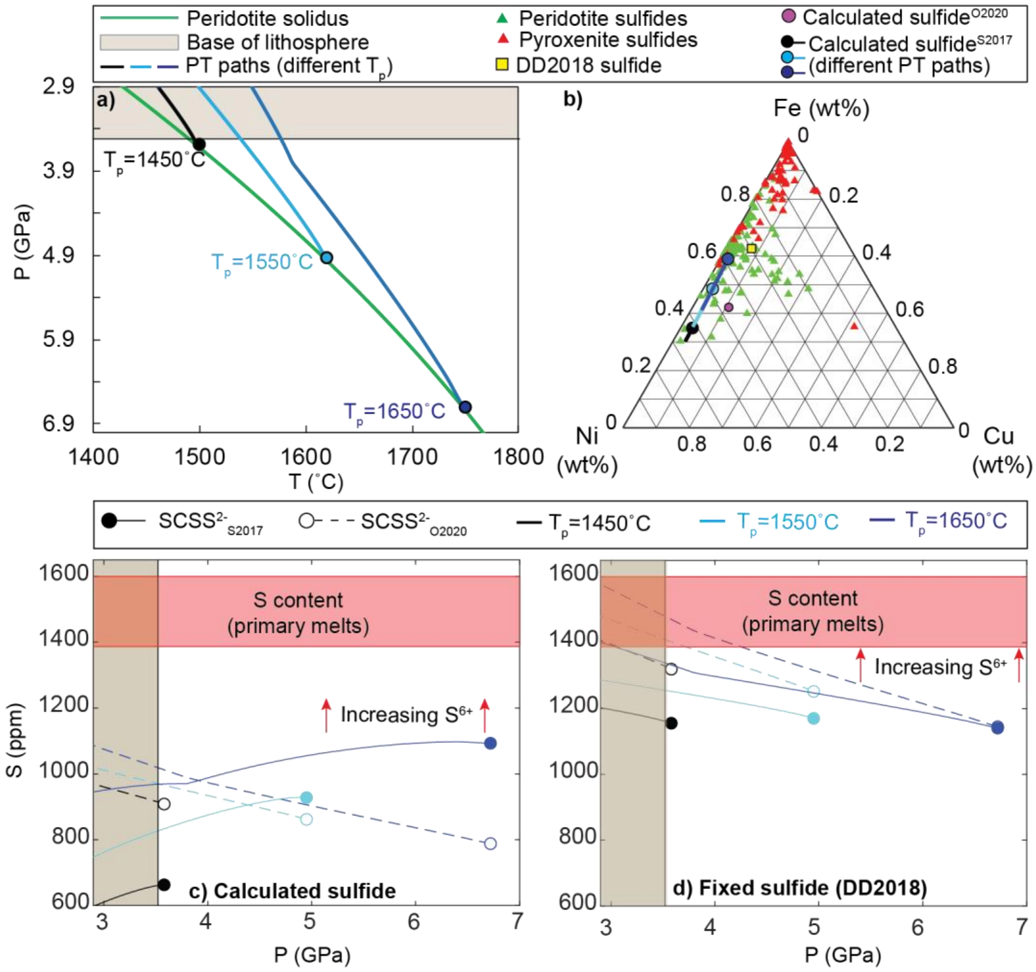

Fig. 7 - Modelling melt S contents during mantle melting. **a)** PT paths for an ascending peridotitic mantle undergoing melting for three different potential temperatures (calculated in Melt-PX; Lambart et al., 2016). **b)** Comparison of calculated sulfide compositions from SCSS^{2-} models with measured sulfide compositions in mantle peridotites and eclogites/pyroxenites (Bulanova et al., 1996; Guo et al., 1999; Pearson et al., 1998; Richardson et al., 2001.; Westerlund et al., 2006). The sulfide composition in the S2017 model changes along the PT path and deviate dramatically from measured sulfide compositions near the top of the melting column. The calculated sulfide composition from the O2020 model also plots away from the composition of most mantle sulfides. The fixed sulfide composition used in the models shown in **d)** is also shown (yellow square; after Ding and Dasgupta, 2018). **c)** Calculated SCSS^{2-} trajectories following the PT paths in **a)** using calculated sulfide compositions. In particular, the behaviour of the S2017 model with decreasing pressure is anomalous. **d)** Calculated SCSS^{2-} trajectories using a fixed sulfide composition (yellow square in **b)**, Ding and Dasgupta, 2018). Except for melts generated right at the base of the lithosphere from a mantle with T$_p$=1650˚C, model trajectories in the S2017 model plot below the estimated S contents of primary Kīlauean melts. Only melts produced near the top of the melting column in the O2020

model plot within the range of primary melts. The beige bar shows the uncertainty in the depth of the base of the lithosphere beneath Kīlauea (Li et al., 2004; Wölbern et al., 2006).

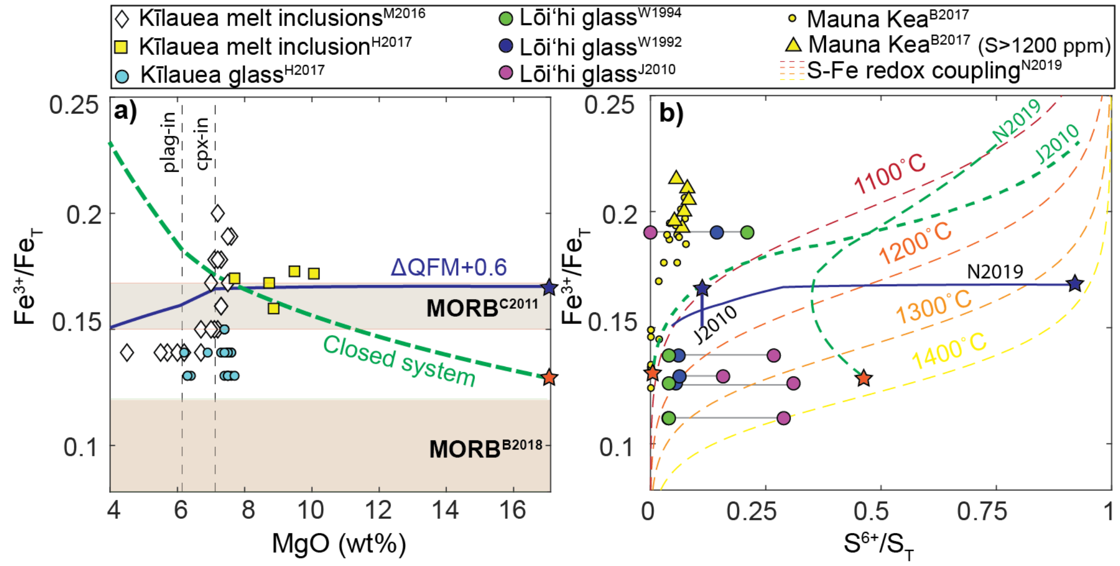

Fig. 8 - Models and observations of S and Fe redox in Hawaiian melts. **a)** Literature measurements of Fe oxidation state in Kīlauean melt inclusions are highly variable (Helz et al., 2017; Moussallam et al., 2016), but consistently elevated above the most recent estimates of MORB redox (Berry et al., 2018), and mostly elevated above even the highest estimates of MORB oxidation state (Cottrell and Kelley, 2011). Fractionation trajectories from the adjusted primary melt composition of Clague et al. (1991) in a closed system, and buffered at ΔQFM+0.6 from Petrolog3 are overlain; the limited MgO range of the XANES data makes it difficult to distinguish which of these models is most realistic. **b)** Literature measurements of Fe and S redox in submarine glasses from Mauna Kea (Brounce et al., 2017) and Lōi'hi. Fe redox measurements for Lōi'hi are taken from Wallace and Carmichael, (1992), and S redox measurements were made on the same samples in three separate studies (Jugo et al., 2010; Wallace and Carmichael, 1992, 1994; joined with a grey line). The fractionation paths in S^{6+}/S_T vs. Fe^{3+}/Fe_T space for the closed and open system models using equation 2 (Jugo et al., 2010) and 3 (Nash et al., 2019) are overlain. S^{6+} corrections of this sort were not made for the models shown in Fig. 7 and 10, because the effect of pressure, which is likely to be substantial during mantle processes, has not been parametrized.

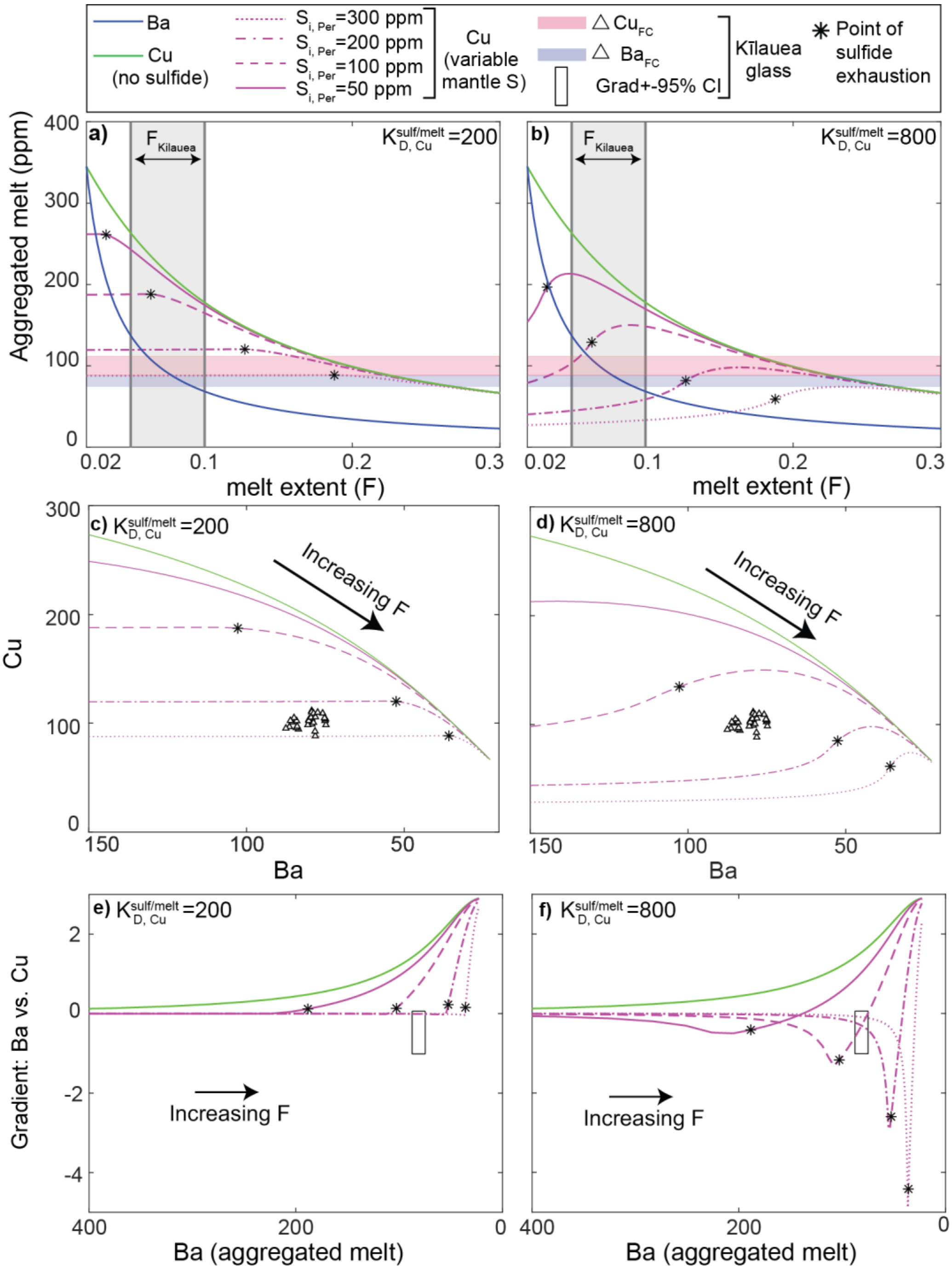

Fig. 9 -Models of Cu and Ba contents in aggregated fractional melts with changing F and initial S contents of the mantle, assuming Cu_{per} = 20 ppm (see Supplementary Fig. A11 for Cu_{per} = 30 ppm). **a-b)** Changes in the Cu contents of aggregated fractional melts with increasing melt extents for two different values of $K_{D,Cu}^{sulf/melt}$. Ba rapidly decreases with increasing melt extents (blue line). If there are no sulfides in the mantle source, Cu shows a less dramatic increase (green line). The purple lines show the evolution of Cu for four different initial S concentrations in the mantle source ($S_{i,\,Per}$). The point at which sulfides are exhausted (black star) moves to progressively higher F values as the amount of S in the mantle increases. The pink and blue

bar show the range of Cu and Ba concentrations in fractionation-corrected Kīlauean glasses from the three rift eruptions which have not fractionated beyond olivine control. Models with low initial mantle S contents vastly overestimate the Cu concentration of primary melts. In **a),** Cu concentrations in melts produced at F=0.05–0.1 with $S_{i,\ Per}$ = 200–300 ppm bracket the range of observed glass Cu concentrations. In **b)** models with $S_{i,\ Per}$ = 100–200 bracket the range of observed values. **c-d)** The concentrations of Cu are plotted against Ba to aid visual assessment of the changing gradients following sulfide exhaustion. **e-f)** **T**he gradient of Ba vs. Cu at each step in the model vs. the Ba concentration of aggregated melts. The black rectangle shows the range of Ba concentrations measured in glasses, and the 95% confidence interval on the observed gradient of Cu vs. Ba (see Fig. 4d). The gradient of Cu vs. Ba is roughly flat until just before sulfides are exhausted. Following sulfide exhaustion, all models show positive gradients.

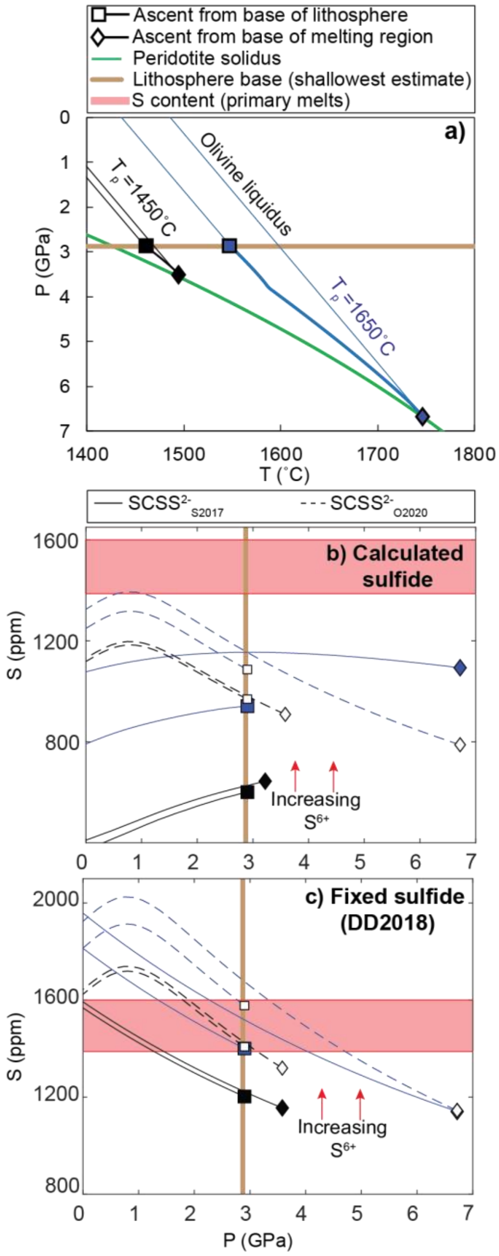

Fig. 10 – Modelling the SCSS^{2-} during the ascent of melts from the mantle into shallow crustal storage reservoirs. **a)** PT paths tracking the ascent of mantle melts generated at bottom and top of the melting column along the olivine liquidus (39.16 ˚C/Gpa; after Matthews et al., 2016). **b-c)** Calculated SCSS^{2-} trajectories for these ascent paths for the adjust primary melt composition of Clague et al. (1991) using calculated (**b**) and fixed sulfide compositions (**c**)**,** as in Fig. 7. The behaviour of the S2017 model in **b**) is likely anomalous. In **c)**, all modelled trajectories except for the lowest T_p (1450 ˚C) in the O2020 model exceed the S concentrations of primary melts at low pressures. The presence of even a very small amount of S^{6+} would mean that the SCSS^{Tot} for this model would also exceed the S contents of primary melts. These models indicate that upon ascent, Kīlauean magmas become sulfide-undersaturated. The beige line marks the shallowest estimate for the base of the lithosphere beneath Kīlauea (Li et al., 2004; Wölbern et al., 2006).

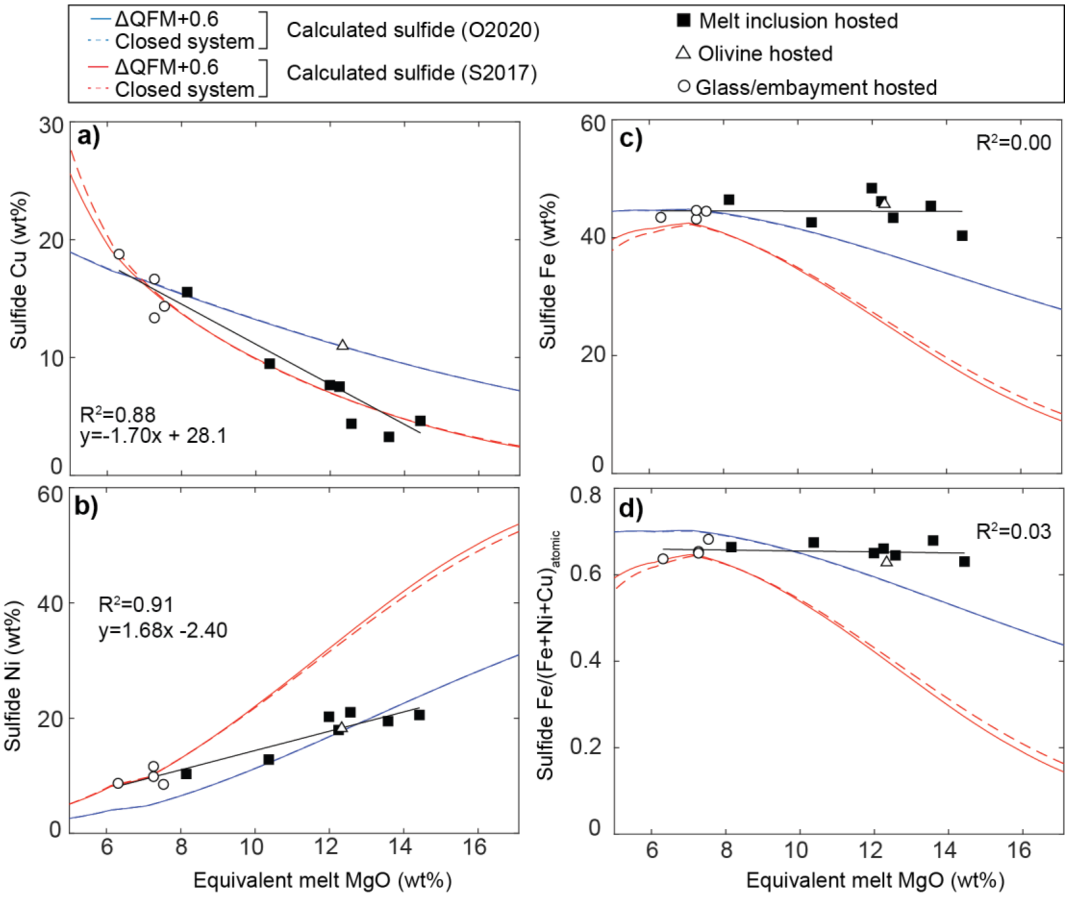

Fig. 11 - Comparison of measured sulfide compositions to those calculated from SCSS^{2-} models. Bulk sulfide compositions were obtained from EDS maps (quantified by analysing sulfide standards whose compositions were determined by EPMA in the same analytical session). Equivalent melt MgO contents for each sulfide were allocated from glass MgO

contents, or olivine Fo contents (see section 4.2). Modelled sulfide compositions were calculated for a fractionation path in Petrolog3 from the adjusted primary magma composition of Clague et al. (1991). Differences in the treatment of melt oxidation state (see Fig. 8a) make negligible differences to the calculated sulfide composition (dashed vs. solid lines).

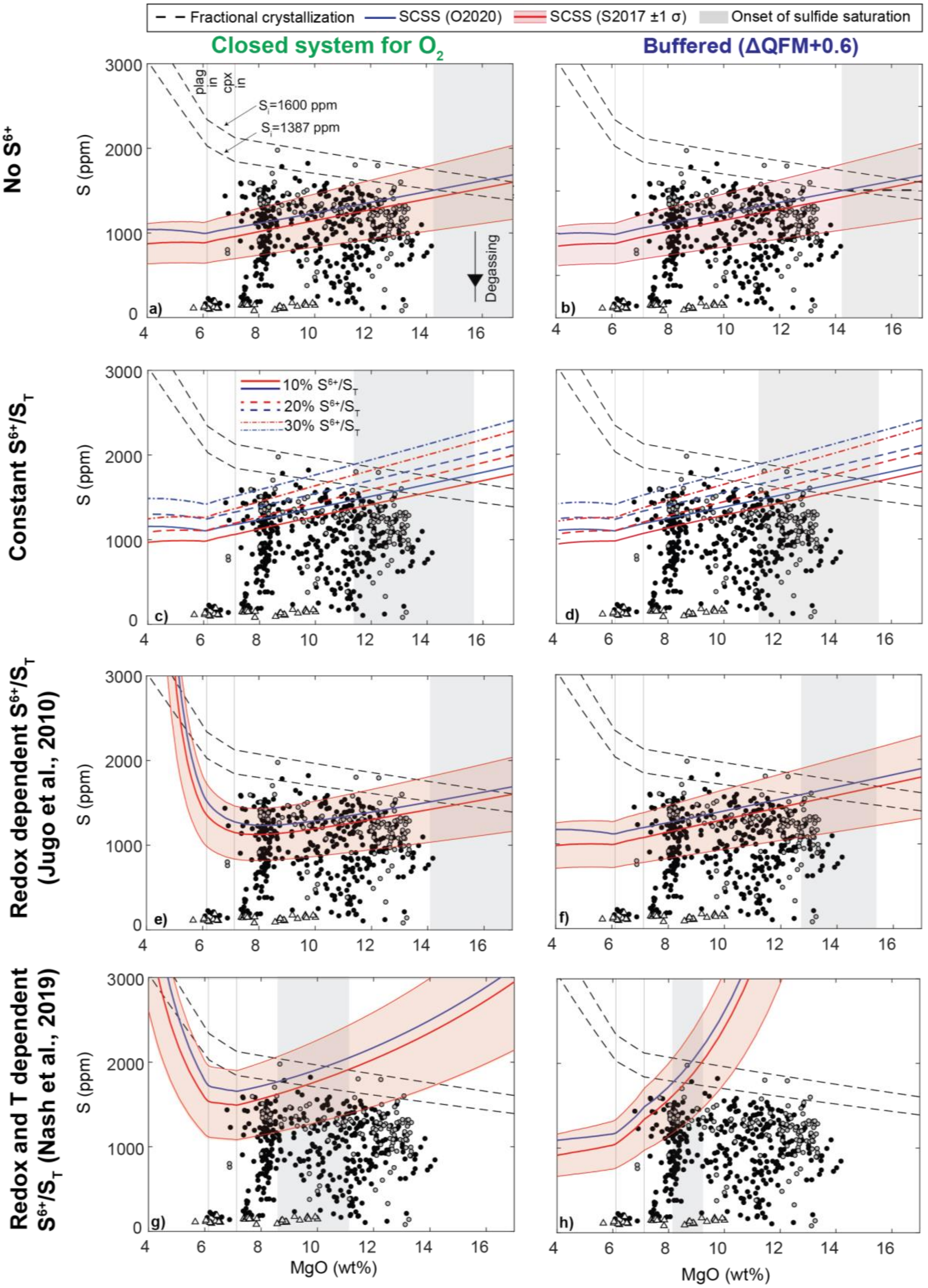

Fig. 12-Modelling changes in sulfide solubility during fractionation. **a-b)** In models only accounting for S^{2-} species, the $SCSS^{2-}$ intercepts the fractionation trajectory for S at high MgO contents (~16 wt% MgO), and cannot account for the high S contents of melt inclusions with <12 wt% MgO. The closed system and buffered model show very similar trajectories, and the O2020 and S2017 are within error of one another (the pink bar indicates the published 1σ uncertainty on the S2017 model). **c-d)** $SCSS_{Tot}$ trajectories following a correction for variable (but constant) amounts of S^{6+} using equation 1. Models with 30% S^{6+} do a good job of recreating the onset of sulfide saturation at ~14 wt% MgO indicated by textural observations, and effectively bracket the upper limit of melt inclusion S contents. **e-f)** $SCSS_{Tot}$ trajectories following a correction for S^{6+} using the parameterization of Jugo et al. (2010; equation 2). The closed system and buffered model differ substantially following the onset of plagioclase fractionation (due to a rapid increase in the proportion of S^{6+} in the closed system model; Fig. 8b). **g-h)** $SCSS_{Tot}$ trajectories following a correction for S^{6+} using the parameterization of Nash et al. (2019; equation 3). As in **e**, the closed system model shows a sharp increase in S solubility during plagioclase fractionation. In the open system model, the strong temperature dependence on the proportion of S^{6+} results in very high estimates of S solubility at high MgO contents.

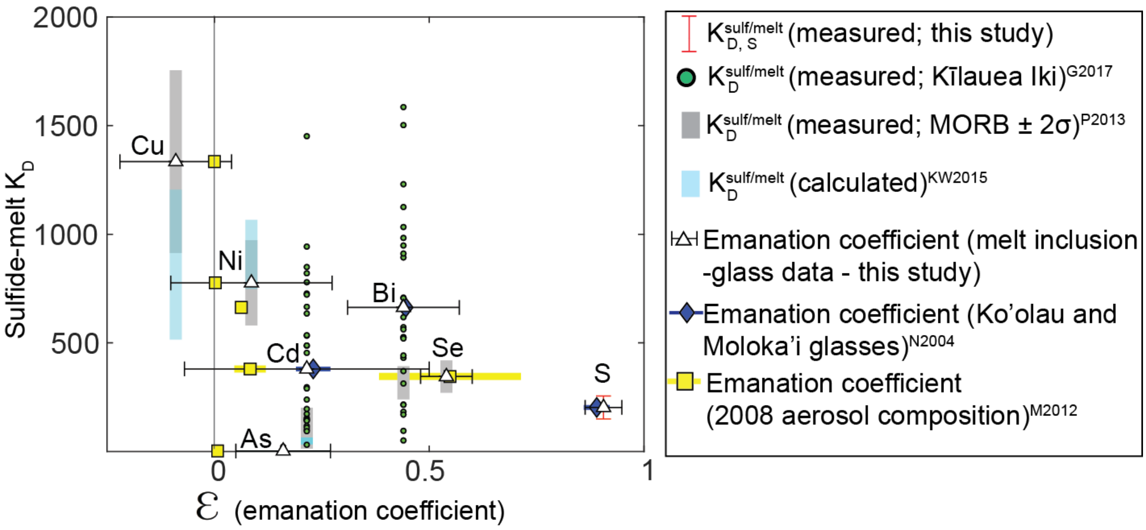

Fig. 13- Comparison of emanation coefficients (this study, Norman et al., 2004, Mather et al., 2012) and sulfide-liquid partition coefficients. Emanation coefficients (white triangles) and black error bars from this study were calculated from the regression lines of each element in melt inclusions and matrix glasses against S (see Fig. 3 and caption for more detail). Emanation coefficients were also calculated from X/S ratios from the 2008 plume (Mather et al., 2012), with the numerator ($[X]_i$-$[X]_f$) calculated from $\frac{X}{S} \times S_{degassed}$ and the denominator ($[X]_i$) calculated from $[X]_f + \frac{X}{S} \times S_{degassed}$, where $[X]_f$ is the average composition of the 1971 matrix

glass (most similar in major element composition to the 2008 summit eruption), and $S_{degassed}$=1300 ppm. Measured sulfide-silicate partition coefficients from Kīlauea Iki lava lake samples are shown in green (Greaney et al., 2017). The range of measured partition coefficients for MORBs are shown with a grey bar (mean ±2σ; Patten et al., 2013). The light blue bar shows the range of calculated partition coefficients from Kiseeva and Wood, (2015) for compositions with MgO contents between 6–14 wt% MgO (using the regressions shown in Fig. 11 to estimate the Ni and Cu composition in the sulfide, and the geothermometer of Helz and Thornber, 1987). The partition coefficient of S was calculated using the range of measured S concentrations in sulfides, assuming melt S contents of 1387–1600 ppm. There is no correlation between sulfide-liquid partition coefficients and emanation coefficients defined using petrology, or aerosol chemistry.

→ Post entrapment crystallization

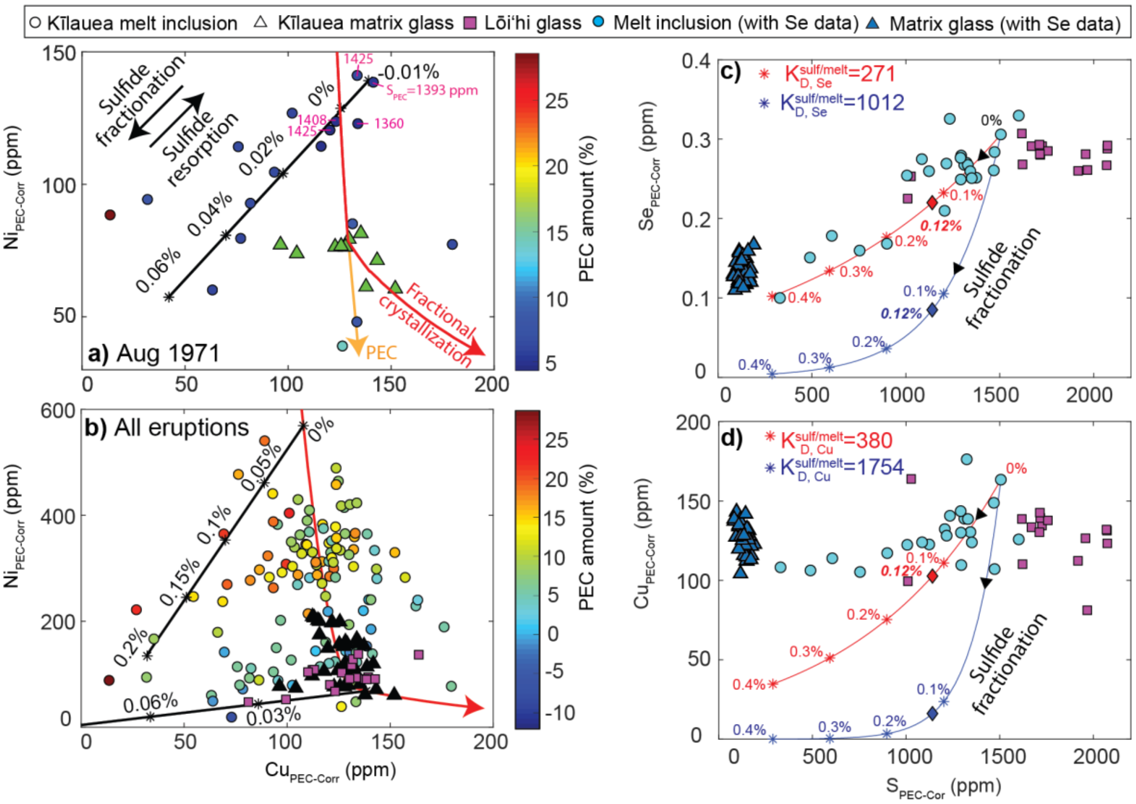

Fig. 14 – Differentiating sulfide resorption and degassing. **a)** Cu-Ni systematics for the 1971 summit eruptions (where melt inclusions exhibit a clear genetic relationship with their carrier melts; Wieser et al., 2019). Matrix glasses largely plot along the sulfide-free fractional crystallization trajectory. Melt inclusion compositions corrected for post-entrapment

crystallization follow two trajectories; olivine-only fractionation (red line), and decreasing Cu and Ni concentrations indicative of sulfide fractionation (black line). The sulfide fractionation trajectory shows the removal of a sulfide composition calculated from the regression lines in Fig. 11 for MgO = 8.4 wt% MgO (mean PEC-corrected melt inclusion MgO content) **b)** Cu-Ni systematics for all matrix glasses and melt inclusions are bracketed by fractional crystallization and sulfide fractionation trends (lower and upper sulfide removal trend for 6.3 and 14.3 wt% MgO). **c)** Models of the trajectory in Se. vs. S space expected from sulfide fractionation. Sulfide fractionation trends fit the data for the lower limit of estimates for the partition coefficient of Se in sulfides. However, the low Se concentrations of matrix glasses require fractionation of large quantities (~0.4%) of sulfide. **d)** Fractionation of this quantity of sulfides is inconsistent with observed Cu-S concentrations in the subset of matrix glass and melt inclusion compositions with Se data. The minimum partition coefficient for Se (271) is calculated from Patten et al. (2013; mean - 2σ), and the maximum (1012) is calculated from the parametrization of Brenan, (2015) for FeO=11.33 wt%. The maximum partition coefficient for Cu is from Patten et al. (2013; mean + 2σ), and the minimum was calculated from the parametrization of Kiseeva and Wood (2015) for the sulfide composition calculated from the regressions in Fig. 8 for 14 wt% MgO, and temperatures from Helz and Thornber (1987).

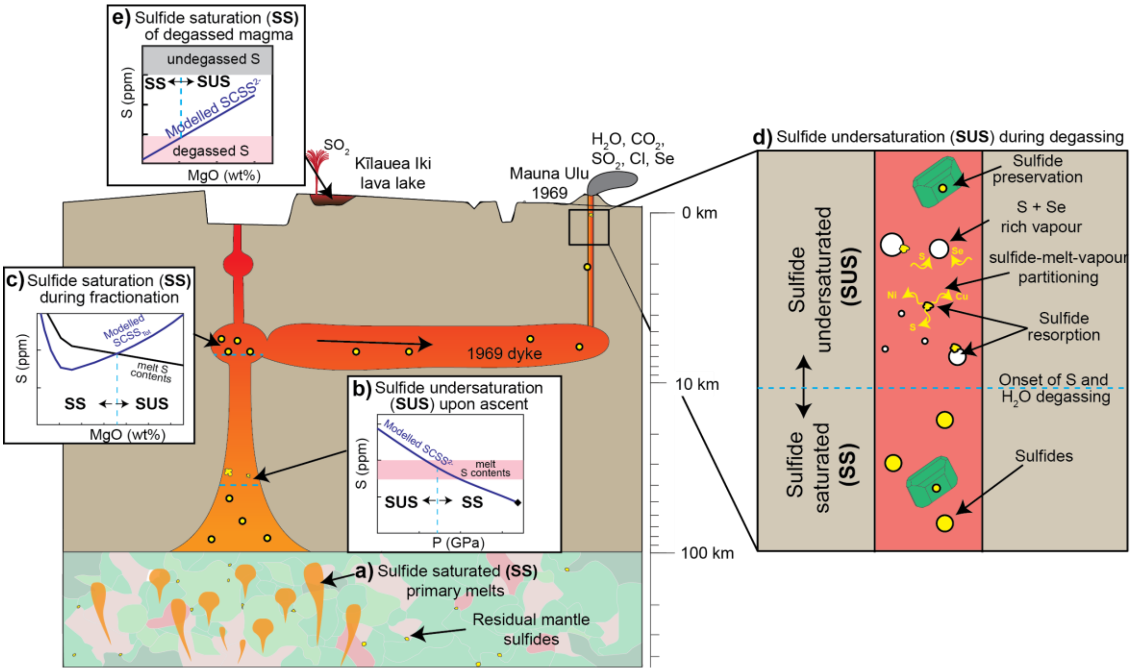

Fig. 15 – Summary diagram of processes affecting chalcophile element concentrations at Kīlauea. **a)** Residual sulfides are present in the mantle source throughout the melting interval of the eruptions analysed in this study (~F<0.1), buffering the concentrations of chalcophile elements relative to lithophile elements during changes in melt extent. The presence of residual sulfides, combined with S^{6+} species account for the high S contents of primary melts

(1387-1600 ppm). **b)** Upon ascent through the thick Hawaiian lithosphere, the large increase in the SCSS^{2-} with decreasing pressure results in melts becoming sulfide undersaturated (SUS). **c)** During fractionation in crustal magma chambers, decreasing temperatures, combined with an increase in melt S contents during crystal fractionation drives the melts towards sulfide saturation once more (~10-14 wt% MgO). **d)** At low pressures as magma ascends towards the site of eruption, S partitions strongly into a vapour phase, rapidly decreasing its concentration in the melt such that it becomes sulfide undersaturated. This causes sulfides to start resorbing, and release their chalcophile element load (S, Ni, Cu etc.) back into the melt. These elements then partition between the melt and vapour phase, resulting in volatile elements such as S and Se mostly partitioning in the gas phase, and more refractory elements such as Ni and Cu remaining in the melt. **e)** The lava filling the Kīlauea Iki lava lake was S-poor (and therefore sulfur undersaturated) due to extensive degassing upon eruption. Extensive amounts of cooling and fractionation were required to reach sulfide saturation from such a S-poor melt.

Research Data

The melt inclusion and glass chalcophile element compositions used in this study are provided as an excel spreadsheet in Appendix B, along with information on standards run in each session.

References

Beattie, P., Ford, C., Russell, D., 1991. Partition coefficients for olivine-melt and orthopyroxene-melt systems. Contributions to Mineralogy and Petrology 109(2), 212–224.

Bennett, V.C., Norman, M.D., Garcia, M.O., 2000. Rhenium and platinum group element abundances correlated with mantle source components in Hawaiian picrites: sulphides in the plume. Earth and Planetary Science Letters 183, 513–526. https://doi.org/10.1016/S0012-821X(00)00295-8

Berlo, K., van Hinsberg, V.J., Vigouroux, N., Gagnon, J.E., Williams-Jones, A.E., 2014. Sulfide breakdown controls metal signature in volcanic gas at Kawah Ijen volcano, Indonesia. Chemical Geology 371, 115–127. https://doi.org/10.1016/j.chemgeo.2014.02.009

Berry, A.J., Stewart, G.A., O’Neill, H.St.C., Mallmann, G., Mosselmans, J.F.W., 2018. A re-assessment of the oxidation state of iron in MORB glasses. Earth and Planetary Science Letters 483, 114–123. https://doi.org/10.1016/j.epsl.2017.11.032

Bougault, H., Hekinian, R., 1974. Rift Valley in the Atlantic Ocean near 36°50′N: petrology and geochemistry of basaltic rocks. Earth and Planetary Science Letters 24, 249–261. https://doi.org/10.1016/0012-821X(74)90103-4

Brenan, J.M., 2015. Se–Te fractionation by sulfide–silicate melt partitioning: Implications for the composition of mantle-derived magmas and their melting residues. Earth and Planetary Science Letters 422, 45–57. https://doi.org/10.1016/j.epsl.2015.04.011

Brounce, M., Stolper, E., Eiler, J., 2017. Redox variations in Mauna Kea lavas, the oxygen fugacity of the Hawaiian plume, and the role of volcanic gases in Earth's oxygenation. Proceedings of the National Academy of Sciences 114, 8997–9002. https://doi.org/10.1073/pnas.1619527114

Bulanova, G.P., Griffin, W.L., Ryan, C.G., Shestakova, O.Y., Barnes, S.-J., 1996. Trace elements in sulfide inclusions from Yakutian diamonds. Contributions to Mineralogy and Petrology 124, 111–125. https://doi.org/10.1007/s004100050179

Cervelli, P.F., Miklius, A., 2003. The Shallow Magmatic System of Kïlauea Volcano, in: USGS Professional Paper. pp. 149–163.

Clague, D.A., Weber, W., Dixon, J., 1991. Picritic Glasses from Hawaii. Nature 353, 6344.

Cottrell, E., Kelley, K.A., 2011. The oxidation state of Fe in MORB glasses and the oxygen fugacity of the upper mantle. Earth and Planetary Science Letters 305, 270–282. https://doi.org/10.1016/j.epsl.2011.03.014

Cox, D., Watt, S.F.L., Jenner, F.E., Hastie, A.R., Hammond, S.J., 2019. Chalcophile element processing beneath a continental arc stratovolcano. Earth and Planetary Science Letters 522, 1–11. https://doi.org/10.1016/j.epsl.2019.06.017

Crowe, B.M., Finnegan, D.L., Zoller, W.H., Boynton, W.V., 1987. Trace element geochemistry of volcanic gases and particles from 1983-1984 eruptive episodes of Kilauea Volcano. Journal of Geophysical Research: Solid Earth 92, 13708–13714. https://doi.org/10.1029/JB092iB13p13708

Czamanske, G.K., Moore, J.G., 1977. Composition and phase chemistry of sulfide globules in basalt from the Mid-Atlantic Ridge rift valley near 37°N lat. Geological Society of America Bulletin 88, 587. https://doi.org/10.1130/0016-7606(1977)88<587:CAPCOS>2.0.CO;2

Desborough, G.A., Anderson, A.T., Wright, T.L., 1968. Mineralogy of sulfides from certain Hawaiian basalts. Economic Geology 63, 636–644. https://doi.org/10.2113/gsecongeo.63.6.636

Ding, S., Dasgupta, R., 2018. Sulfur Inventory of Ocean Island Basalt Source Regions Constrained by Modeling the Fate of Sulfide during Decompression Melting of a Heterogeneous Mantle. Journal of Petrology 59, 1281–1308. https://doi.org/10.1093/petrology/egy061

Dixon, J.E., Clague, D.A., Stolper, E.M., 1991. Degassing History of Water, Sulfur, and Carbon in Submarine Lavas from Kilauea Volcano, Hawaii. The Journal of Geology 99, 371–394. https://doi.org/10.1086/629501

Dixon, J.E., Clague, D.A., Wallace, P., Poreda, R., 1997. Volatiles in Alkalic Basalts form the North Arch Volcanic Field, Hawaii: Extensive Degassing of Deep Submarine-erupted Alkalic Series Lavas. Journal of Petrology 38, 911–939. https://doi.org/10.1093/petroj/38.7.911

Edmonds, M., Gerlach, T.M., Herd, R.A., 2009. Halogen degassing during ascent and eruption of water-poor basaltic magma. Chemical Geology 263(1–4), 122–130.

Edmonds, M., Mather, T.A., 2017. Volcanic Sulfides and Outgassing. Elements 13, 105–110. https://doi.org/10.2113/gselements.13.2.105

Edmonds, M., Mather, T.A., Liu, E.J., 2018. A distinct metal fingerprint in arc volcanic emissions. Nature Geoscience 11, 790–794. https://doi.org/10.1038/s41561-018-0214-5

Fleet, M.E., Stone, W.E., 1990. Nickeliferous sulfides in xenoliths, olivine megacrysts and basaltic glass. Contributions to Mineralogy and Petrology 105, 629–636. https://doi.org/10.1007/BF00306529

Fortin, M.-A., Riddle, J., Desjardins-Langlais, Y., Baker, D.R., 2015. The effect of water on the sulfur concentration at sulfide saturation (SCSS) in natural melts. Geochimica et Cosmochimica Acta 160, 100–116. https://doi.org/10.1016/j.gca.2015.03.022

Garcia, M.O., Jorgenson, B.A., Mahoney, J.J., Ito, E., Irving, A.J., 1993. An evaluation of temporal geochemical evolution of Loihi Summit Lavas: Results from *Alvin* submersible dives. Journal of Geophysical Research: Solid Earth 98, 537–550. https://doi.org/10.1029/92JB01707

Garcia, M.O., Rubin, K.H., Norman, M.D., Rhodes, J.M., Graham, D.W., Muenow, D.W., Spencer, K., 1998. Petrology and geochronology of basalt breccia from the 1996 earthquake swarm of Loihi seamount, Hawaii: magmatic history of its 1996 eruption. Bulletin of Volcanology 59, 577–592. https://doi.org/10.1007/s004450050211

Gerlach, T.M., Nordlie, B.E., 1975. The C-O-H-S Gaseous system, part III. American Journal of Science 275(4), 353–376.

Greaney, A.T., Rudnick, R.L., Helz, R.T., Gaschnig, R.M., Piccoli, P.M., Ash, R.D., 2017. The behavior of chalcophile elements during magmatic differentiation as observed in Kilauea Iki lava lake, Hawaii. Geochimica et Cosmochimica Acta 210, 71–96. https://doi.org/10.1016/j.gca.2017.04.033

Greenland, L.P., 1984. Gas composition of the January 1983 eruption of Kilauea Volcano, Hawaii. Geochimica et Cosmochimica Acta 48, 193–195. https://doi.org/10.1016/0016-7037(84)90361-2

Greenland, L.P., Okamura, A.T., Stokes, J.B., 1988. Constraints on the mechanism of eruption, in: The Pu'u O' O Eruption of Kilauea Volcano, Hawai'i: Episodes 1 through 20. US Geological Survey Professional Paper, p. 251.

Guo, J., Griffin, W.L., O'Reilly, S.Y., 1999. Geochemistry and Origin of Sulphide Minerals in Mantle Xenoliths: Qilin, Southeastern China. Journal of Petrology 40, 1125–1149.

Hartley, M.E., Shorttle, O., Maclennan, J., Moussallam, Y., Edmonds, M., 2017. Olivine-hosted melt inclusions as an archive of redox heterogeneity in magmatic systems. Earth and Planetary Science Letters 479, 192–205. https://doi.org/10.1016/j.epsl.2017.09.029

Helmy, H.M., Fonseca, R.O.C., 2017. The behavior of Pt, Pd, Cu and Ni in the Se-sulfide system between 1050 and 700 °C and the role of Se in platinum-group elements fractionation in sulfide melts. Geochimica et Cosmochimica Acta 216, 141–152. https://doi.org/10.1016/j.gca.2017.05.010

Helz, R., 1987. Diverse olivine types in lava of the 1959 eruption of Kilauea volcano and their bearing on eruption dynamics. Volcanism In Hawaii 1 691–722.

Helz, R.T., Clague, D.A., Sisson, T.W., Thornber, C.R., 2014. Petrologic Insights into Basaltic Volcanism at Historically Active Hawaiian Volcanoes, in: Characteristics of Hawaiian Volcanoes.

Helz, R.T., Cottrell, E., Brounce, M.N., Kelley, K.A., 2017. Olivine-melt relationships and syneruptive redox variations in the 1959 eruption of Kīlauea Volcano as revealed by XANES.

Journal of Volcanology and Geothermal Research 333–334, 1–14. https://doi.org/10.1016/j.jvolgeores.2016.12.006

Helz, R.T., Thornber, C.R., 1987. Geothermometry of Kilauea Iki lava lake, Hawaii. Bulletin of Volcanology 49, 651–668. https://doi.org/10.1007/BF01080357

Helz, R.T., Wright, T.L., 1992. Differentiation and magma mixing on Kilauea's east rift zone: A further look at the eruptions of 1955 and 1960. Part I. The late 1955 lavas. Bulletin of Volcanology 54, 361–384. https://doi.org/10.1007/BF00312319

Helz, R.T. and Wright, T.L., 1983. Drilling report and core logs for the 1981 drilling of Kilauea Iki lava 1200 lake, Kilauea volcano, Hawaii, with comparative notes on earlier (1967-1979) drilling experiences (No. 1201 USGS-OFR-83-326). Geological Survey, Reston, VA (USA)

Hofmann, A.W., Feigenson, M.D., Raczek, I., 1984. Case studies on the origin of basalt: III. Petrogenesis of the Mauna Ulu eruption, Kilauea, 1969-1971. Contributions to Mineralogy and Petrology 88, 24–35. https://doi.org/10.1007/BF00371409

Jenner, F.E., 2017. Cumulate causes for the low contents of sulfide-loving elements in the continental crust. Nature Geoscience 10, 524–529. https://doi.org/10.1038/ngeo2965

Jenner, F.E., Arculus, R.J., Mavrogenes, J.A., Dyriw, N.J., Nebel, O., Hauri, E.H., 2012. Chalcophile element systematics in volcanic glasses from the northwestern Lau Basin. Geochemistry, Geophysics, Geosystems 13, 1–25. https://doi.org/10.1029/2012GC004088

Jenner, F.E., Arevalo, R.D., 2016. Major and Trace Element Analysis of Natural and Experimental Igneous Systems using LA–ICP–MS. ELEMENTS 12, 311–316. https://doi.org/10.2113/gselements.12.5.311

Jenner, F.E., Hauri, E.H., Bullock, E.S., König, S., Arculus, R.J., Mavrogenes, J.A., Mikkelson, N., Goddard, C., 2015. The competing effects of sulfide saturation versus degassing on the behavior of the chalcophile elements during the differentiation of hydrous melts. Geochemistry, Geophysics, Geosystems 16, 1490–1507. https://doi.org/10.1002/2014GC005670

Jenner, F.E., Holden, P., Mavrogenes, J.A., O'Neill, H.St.C., Allen, C., 2009. Determination of Selenium Concentrations in NIST SRM 610, 612, 614 and Geological Glass Reference Materials Using the Electron Probe, LA-ICP-MS and SHRIMP II. Geostandards and Geoanalytical Research 33, 309–317. https://doi.org/10.1111/j.1751-908X.2009.00024.x

Jenner, F.E., O'Neill, H.St.C., 2012. Major and trace analysis of basaltic glasses by laser-ablation ICP-MS: ANALYSIS OF GLASSES BY LA-ICP-MS. Geochem. Geophys. Geosyst. 13, n/a-n/a. https://doi.org/10.1029/2011GC003890

Jenner, F.E., O'Neill, H.ST.C., Arculus, R.J., Mavrogenes, J.A., 2010. The Magnetite Crisis in the Evolution of Arc-related Magmas and the Initial Concentration of Au, Ag and Cu. Journal of Petrology 51, 2445–2464. https://doi.org/10.1093/petrology/egq063

Jochum, K.P., Hofmann, A.W., 1997. Constraints on earth evolution from antimony in mantle-derived rocks. Chemical Geology 39–49.

Jochum, K.P., Stoll, B., Herwig, K., Willbold, M., Hofmann, A.W., Amini, M., Aarburg, S., Abouchami, W., Hellebrand, E., Mocek, B., Raczek, I., Stracke, A., Alard, O., Bouman, C., Becker, S., Dücking, M., Brätz, H., Klemd, R., de Bruin, D., Canil, D., Cornell, D., de Hoog, C.-J., Dalpé, C., Danyushevsky, L., Eisenhauer, A., Gao, Y., Snow, J.E., Groschopf, N., Günther, D., Latkoczy, C., Guillong, M., Hauri, E.H., Höfer, H.E., Lahaye, Y., Horz, K., Jacob, D.E., Kasemann, S.A., Kent, A.J.R., Ludwig, T., Zack, T., Mason, P.R.D., Meixner, A., Rosner, M., Misawa, K., Nash, B.P., Pfänder, J., Premo, W.R., Sun, W.D., Tiepolo, M., Vannucci, R., Vennemann, T., Wayne, D., Woodhead, J.D., 2006. MPI-DING reference glasses for in situ microanalysis: New reference values for element concentrations and isotope ratios. Geochemistry, Geophysics, Geosystems 7. https://doi.org/10.1029/2005GC001060

Jugo, P.J., Luth, R.W., Richards, J., 2005. An Experimental Study of the Sulfur Content in Basaltic Melts Saturated with Immiscible Sulfide or Sulfate Liquids at 1300 C and 1{middle dot}0 GPa. Journal of Petrology 46, 783–798. https://doi.org/10.1093/petrology/egh097

Jugo, P.J., Wilke, M., Botcharnikov, R.E., 2010. Sulfur K-edge XANES analysis of natural and synthetic basaltic glasses: Implications for S speciation and S content as function of oxygen fugacity. Geochimica et Cosmochimica Acta 74, 5926–5938. https://doi.org/10.1016/j.gca.2010.07.022

Kelley, K.A., Kingsley, R., Schilling, J.-G., 2013. Composition of plume-influenced mid-ocean ridge lavas and glasses from the Mid-Atlantic Ridge, East Pacific Rise, Galápagos Spreading Center, and Gulf of Aden. Geochemistry, Geophysics, Geosystems 14, 223–242. https://doi.org/10.1002/ggge.20049

Kiseeva, E.S., Fonseca, R.O.C., Smythe, D.J., 2017. Chalcophile Elements and Sulfides in the Upper Mantle. Elements 13, 111–116. https://doi.org/10.2113/gselements.13.2.111

Kiseeva, E.S., Wood, B.J., 2015. The effects of composition and temperature on chalcophile and lithophile element partitioning into magmatic sulphides. Earth and Planetary Science Letters 424, 280–294. https://doi.org/10.1016/j.epsl.2015.05.012

Lambart, S., Baker, M.B., Stolper, E.M., 2016. The role of pyroxenite in basalt genesis: Melt-PX, a melting parameterization for mantle pyroxenites between 0.9 and 5 GPa: Melt-PX: Pyroxenite Melting Model. Journal of Geophysical Research: Solid Earth 121, 5708–5735. https://doi.org/10.1002/2015JB012762

Lambert, G., Le Cloarec, M.F., Ardouin, B., Le Roulley, J.C., 1985. Volcanic emission of radionuclides and magma dynamics. Earth and Planetary Science Letters 76, 185–192. https://doi.org/10.1016/0012-821X(85)90158-X

Lee, C.-T.A., Luffi, P., Chin, E.J., Bouchet, R., Dasgupta, R., Morton, D.M., Le Roux, V., Yin, Q. -z., Jin, D., 2012. Copper Systematics in Arc Magmas and Implications for Crust-Mantle Differentiation. Science 336, 64–68. https://doi.org/10.1126/science.1217313

Li, C., Ripley, E.M., 2009. Sulfur Contents at Sulfide-Liquid or Anhydrite Saturation in Silicate Melts: Empirical Equations and Example Applications. Economic Geology 104, 405–412. https://doi.org/10.2113/gsecongeo.104.3.405

Li, C., Ripley, E.M., 2005. Empirical equations to predict the sulfur content of mafic magmas at sulfide saturation and applications to magmatic sulfide deposits. Mineralium Deposita 40, 218–230. https://doi.org/10.1007/s00126-005-0478-8

Li, X., Kind, R., Yuan, X., Wölbern, I., Hanka, W., 2004. Rejuvenation of the lithosphere by the Hawaiian plume. Nature 427, 827–829. https://doi.org/10.1038/nature02349

Li, Y., Audétat, A., 2015. Effects of temperature, silicate melt composition, and oxygen fugacity on the partitioning of V, Mn, Co, Ni, Cu, Zn, As, Mo, Ag, Sn, Sb, W, Au, Pb, and Bi between sulfide phases and silicate melt. Geochimica et Cosmochimica Acta 162, 25–45. https://doi.org/10.1016/j.gca.2015.04.036

Liu, X., Xiong, X., Audétat, A., Li, Y., Song, M., Li, L., Sun, W., Ding, X., 2014. Partitioning of copper between olivine, orthopyroxene, clinopyroxene, spinel, garnet and silicate melts at upper mantle conditions. Geochimica et Cosmochimica Acta 125, 1–22. https://doi.org/10.1016/j.gca.2013.09.039

Loewen, M.W., 2013. Volatile Mobility of Trace Metals in Volcanic Systems.

Longo, B.M., Yang, W., Green, J.B., Crosby, F.L., Crosby, V.L., 2010. Acute Health Effects Associated with Exposure to Volcanic Air Pollution (vog) from Increased Activity at Kilauea Volcano in 2008. Journal of Toxicology and Environmental Health, Part A 73, 1370–1381. https://doi.org/10.1080/15287394.2010.497440

Maal�e, S., Hansen, B., 1982. Olivine phenocrysts of Hawaiian olivine tholeiite and oceanite. Contr. Mineral. and Petrol. 81, 203–211. https://doi.org/10.1007/BF00371297

Mather, T.A., Witt, M.L.I., Pyle, D.M., Quayle, B.M., Aiuppa, A., Bagnato, E., Martin, R.S., Sims, K.W.W., Edmonds, M., Sutton, A.J., Ilyinskaya, E., 2012. Halogens and trace metal emissions from the ongoing 2008 summit eruption of Kīlauea volcano, Hawai`i. Geochimica et Cosmochimica Acta 83, 292–323. https://doi.org/10.1016/j.gca.2011.11.029

Matjuschkin, V., Blundy, J.D., Brooker, R.A., 2016. The effect of pressure on sulphur speciation in mid- to deep-crustal arc magmas and implications for the formation of porphyry copper deposits. Contributions to Mineralogy and Petrology 171, 66. https://doi.org/10.1007/s00410-016-1274-4

Matthews, S., Shorttle, O., Maclennan, J., 2016. The temperature of the Icelandic mantle from olivine-spinel aluminum exchange thermometry. Geochemistry, Geophysics, Geosystems 17, 4725–4752. https://doi.org/10.1002/2016GC006497

Mavrogenes, J.A., O'Neill, H.St.C., 1999. The relative effects of pressure, temperature and oxygen fugacity on the solubility of sulfide in mafic magmas. Geochimica et Cosmochimica Acta 63, 1173–1180. https://doi.org/10.1016/S0016-7037(98)00289-0

Metrich, N., Mandeville, C.W., 2010. Sulfur in Magmas. Elements 6, 81–86. https://doi.org/10.2113/gselements.6.2.81

Moore, R.B., Helz, R.T., Dzurisin, D., Eaton, G.P., Koyanagi, R., Lipman, P.W., Lockwood, J.P., Puniwai, G.S., 1980. THE 1977 ERUPTION OF KILAUEA VOLCANO, HAWAII. Journal of Volcanology and Geothermal Research 7(3–4), 189–210.

Moussallam, Y., Edmonds, M., Scaillet, B., Peters, N., Gennaro, E., Sides, I., Oppenheimer, C., 2016. The impact of degassing on the oxidation state of basaltic magmas: A case study of Kīlauea volcano. Earth and Planetary Science Letters 450, 317–325. https://doi.org/10.1016/j.epsl.2016.06.031

Moussallam, Y., Longpré, M.-A., McCammon, C., Gomez-Ulla, A., Rose-Koga, E.F., Scaillet, B., Peters, N., Gennaro, E., Paris, R., Oppenheimer, C., 2019. Mantle plumes are oxidised. Earth and Planetary Science Letters 527, 115798. https://doi.org/10.1016/j.epsl.2019.115798

Mungall, J.E., Brenan, J.M., Godel, B., Barnes, S.J., Gaillard, F., 2015. Transport of metals and sulphur in magmas by flotation of sulphide melt on vapour bubbles. Nature Geoscience 8, 216–219. https://doi.org/10.1038/ngeo2373

Mysen, B.O., 1978. Experimental determination of nickel partition coefficients between liquid, pargasite, and garnet peridotite minerals and concentration limits of behavior according to

Henry's law at high pressure and temperature. American Journal of Science 278, 217–243. https://doi.org/10.2475/ajs.278.2.217

Nadeau, O., Williams-Jones, A.E., Stix, J., 2010. Sulphide magma as a source of metals in arc-related magmatic hydrothermal ore fluids. Nature Geoscience 3, 501–505. https://doi.org/10.1038/ngeo899

Nash, W.M., Smythe, D.J., Wood, B.J., 2019. Compositional and temperature effects on sulfur speciation and solubility in silicate melts. Earth and Planetary Science Letters 507, 187–198. https://doi.org/10.1016/j.epsl.2018.12.006

Neal, C.A., Brantley, S.R., Antolik, L., Babb, J.L., Burgess, M., Calles, K., Cappos, M., Chang, J.C., Conway, S., Desmither, L., Dotray, P., Elias, T., Fukunaga, P., Fuke, S., Johanson, I.A., Kamibayashi, K., Kauahikaua, J., Lee, R.L., Pekalib, S., Miklius, A., Million, W., Moniz, C.J., Nadeau, P.A., Okubo, P., Parcheta, C., Patrick, M.R., Shiro, B., Swanson, D.A., Tollett, W., Trusdell, F., Younger, E.F., Zoeller, M.H., Montgomery-Brown, E.K., Anderson, K.R., Poland, M.P., Ball, J.L., Bard, J., Coombs, M., Dietterich, H.R., Kern, C., Thelen, W.A., Cervelli, P.F., Orr, T., Houghton, B.F., Gansecki, C., Hazlett, R., Lundgren, P., Diefenbach, A.K., Lerner, A.H., Waite, G., Kelly, P., Clor, L., Werner, C., Mulliken, K., Fisher, G., Damby, D., 2018. The 2018 rift eruption and summit collapse of Kīlauea Volcano. Science eaav7046. https://doi.org/10.1126/science.aav7046

Nelson, S., Sewake, K., 2008. Volcanic Emissions Injury to Plant Foliage. College of Tropical Agriculture and Human Resources 11. https://scholarspace.manoa.hawaii.edu/bitstream/10125/12429/PD-47.pdf

Newsom, H.E., White, W.M., Jochum, K.P., Hofmann, A.W., 1986. Siderophile and chalcophile element abundances in oceanic basalts, Pb isotope evolution and growth of the Earth's core. Earth and Planetary Science Letters 80, 299–313. https://doi.org/10.1016/0012-821X(86)90112-3

Norman, M.D., Garcia, M.O., Bennett, V.C., 2004. Rhenium and chalcophile elements in basaltic glasses from Ko'olau and Moloka'i volcanoes: Magmatic outgassing and composition of the Hawaiian plume. Geochimica et Cosmochimica Acta 68, 3761–3777. https://doi.org/10.1016/j.gca.2004.02.025

Norman, M.D., Garcia, M.O., Kamenetsky, V.S., Nielsen, R.L., 2002. Olivine-hosted melt inclusions in Hawaiian picrites: equilibration, melting, and plume source characteristics. Chemical Geology 183, 143–168. https://doi.org/10.1016/S0009-2541(01)00376-X

O'Neill, H.St.C., 2020. The thermodynamic controls on sulfide saturation in silicate melts with application to Ocean Floor Basalts. Agu Monograph, editors Daniel Neuville and Roberto Moretti. In 1335 press.

Palme, H., O'Neill, H.St.C., 2014. Cosmochemical Estimates of Mantle Composition, in: Treatise on Geochemistry. Elsevier, pp. 1–39. https://doi.org/10.1016/B978-0-08-095975-7.00201-1

Patten, C., Barnes, S.-J., Mathez, E.A., 2012. TEXTURAL VARIATIONS IN MORB SULFIDE DROPLETS DUE TO DIFFERENCES IN CRYSTALLIZATION HISTORY. The Canadian Mineralogist 50, 675–692. https://doi.org/10.3749/canmin.50.3.675

Patten, C., Barnes, S.-J., Mathez, E.A., Jenner, F.E., 2013. Partition coefficients of chalcophile elements between sulfide and silicate melts and the early crystallization history of sulfide liquid: LA-ICP-MS analysis of MORB sulfide droplets. Chemical Geology 358, 170–188. https://doi.org/10.1016/j.chemgeo.2013.08.040

Pearson, D.G., Shirey, S.B., Harris, J.W., Carlson, R.W., 1998. Sulphide inclusions in diamonds from the Koffiefontein kimberlite, S Africa: constraints on diamond ages and mantle Re–Os systematics. Earth and Planetary Science Letters 160, 311–326. https://doi.org/10.1016/S0012-821X(98)00092-2

Peck, D., 1978. Cooling and Vesiculation of Alae lava lake, Hawaii. US Geological Survey Professional Paper 935-B.

Pietruszka, A.J., Garcia, M.O., 1999. A Rapid Fluctuation in the Mantle Source and Melting History of Kilauea Volcano Inferred from the Geochemistry of its Historical Summit Lavas (1790–1982). Journal of Petrology 40, 1321–1342.

Pietruszka, A.J., Keyes, M.J., Duncan, J.A., Hauri, E.H., Carlson, R.W., Garcia, M.O., 2011. Excesses of seawater-derived 234U in volcanic glasses from Loihi Seamount due to crustal contamination. Earth and Planetary Science Letters 304, 280–289. https://doi.org/10.1016/j.epsl.2011.02.018

Pietruszka, A.J., Marske, J.P., Heaton, D.E., Garcia, M.O., Rhodes, J.M., 2018. An Isotopic Perspective into the Magmatic Evolution and Architecture of the Rift Zones of Kīlauea Volcano. Journal of Petrology. https://doi.org/10.1093/petrology/egy098

Pitcher, L., Helz, R.T., Walker, R.J., Piccoli, P., 2009. Fractionation of the platinum-group elments and Re during crystallization of basalt in Kilauea Iki Lava Lake, Hawaii. Chemical Geology 260, 196–210. https://doi.org/10.1016/j.chemgeo.2008.12.022

Poland, M.P., Miklius, A., Emily, M.-B., 2014. Magma Supply, Storage, and Transport at Shield-Stage Hawaiian Volcanoes, in: Characteristics of Hawaiian Volcanoes. pp. 179–234.

Putirka, K.D., 2017. Down the Crater: Where Magmas are Stored and Why They Erupt. Elements 13, 11–16. https://doi.org/10.2113/gselements.13.1.11

Putirka, K.D., 2008. Thermometers and Barometers for Volcanic Systems. Reviews in Mineralogy and Geochemistry 69, 61–120. https://doi.org/10.2138/rmg.2008.69.3

Reekie, C.D.J., Jenner, F.E., Smythe, D.J., Hauri, E.H., Bullock, E.S., Williams, H.M., 2019. Sulfide resorption during crustal ascent and degassing of oceanic plateau basalts. Nature Communications 10. https://doi.org/10.1038/s41467-018-08001-3

Richardson, S.H., Shirey, S.B., Harris, J.W., Carlson, R.W., n.d. Archean subduction recorded by Re^Os isotopes in eclogitic sul¢de inclusions in Kimberley diamonds. Earth and Planetary Science Letters 10.

Robock, A., 2000. Volcanic eruptions and climate. Reviews of Geophysics 38, 191–219. https://doi.org/10.1029/1998RG000054

Roedder, E., 1983. Geobarometry of ultramafic xenoliths from Loihi seamount, Hawaii, on the basis of CO2 inclusions in olivine. Earth and Planetary Science Letters 66, 369–379.

Saal, A.E., Hauri, E.H., Langmuir, C.H., Perfit, M.R., 2002. Vapour undersaturation in primitive mid-ocean-ridge basalt and the volatile content of Earth’s upper mantle. Nature 419, 451–455. https://doi.org/10.1038/nature01073

Sides, I., Edmonds, M., Maclennan, J., Houghton, B.F., Swanson, D.A., Steele-MacInnis, M.J., 2014. Magma mixing and high fountaining during the 1959 Kīlauea Iki eruption, Hawaiʻi. Earth and Planetary Science Letters 400, 102–112. https://doi.org/10.1016/j.epsl.2014.05.024

Sides, I.R., Edmonds, M., Maclennan, J., Swanson, D.A., Houghton, B.F., 2014. Eruption style at Kīlauea Volcano in Hawaiʻi linked to primary melt composition. Nature Geoscience 7, 464–469. https://doi.org/10.1038/ngeo2140

Sisson, T.W., 2003. Native gold in a Hawaiian alkalic magma. Economic Geology 98, 643–648. https://doi.org/10.2113/gsecongeo.98.3.643

Skinner, B., Peck, D., 1969. An immiscible sulfide melt from Hawaii in Magmatic Ore Deposits, H. D. B. Wilson, Society of Economic Geologists.

Smythe, D.J., Wood, B.J., Kiseeva, E.S., 2017. The S content of silicate melts at sulfide saturation: New experiments and a model incorporating the effects of sulfide composition. American Mineralogist 102, 795–803. https://doi.org/10.2138/am-2017-5800CCBY

Stone, W.E., Fleet, M.E., 1991. Nickel-copper sulfides from the 1959 eruption of Kilauea Volcano, Hawaii: Contrasting compositions and phase relations in eruption pumice and Kilauea Iki lava lake. American Mineralogist 76(7–8).

Sutton, A.J., Elias, T., Gerlach, T.M., Stokes, J.B., 2001. Implications for eruptive processes as indicated by sulfur dioxide emissions from Killauea Volcano, Hawai`i, 1979-1997. Journal of Volcanology and Geothermal Research 20.

Sutton, A.J., Elias, T., Kauahikaua, J., 2003. Lava-Effusion Rates for the Puʻu ʻÖʻö-Küpaianaha Eruption Derived from SO2 Emissions and Very Low Frequency (VLF) Measurements 12.

Swanson, D.A., Duffield, W.A., Jackson, D.B., Peterson, D.W., 1979. Chronological narrative of the 1969-71 Mauna Ulu eruption of Kilauea Volcano, Hawaii. Geological Survey Professional Paper 1056.

Tam, E., Miike, R., Labrenz, S., Sutton, A.J., Elias, T., Davis, J., Chen, Y.-L., Tantisira, K., Dockery, D., Avol, E., 2016. Volcanic air pollution over the Island of Hawai'i: Emissions, dispersal, and composition. Association with respiratory symptoms and lung function in Hawai'i Island school children. Environment International 92–93, 543–552. https://doi.org/10.1016/j.envint.2016.03.025

Tatsumi, Y., Oguri, K., Shimoda, G., 1999. The behaviour of platinum-group elements during magmatic differentiation in Hawaiian tholeiites. Geochemical Journal 33, 237–247. https://doi.org/10.2343/geochemj.33.237

Thornber, C.R., Tim, O., Heliker, C., Hoblitt, R.P., 2015. Petrologic testament to changes in shallow magma storage and transport during 30+ years of recharge and eruption at Kılauea Volcano, Hawai ʻ, in: Hawaiian Volcanoes: From Source to Surface.

Tuohy, R.M., Wallace, P.J., Loewen, M.W., Swanson, D.A., Kent, A.J.R., 2016. Magma transport and olivine crystallization depths in Kīlauea's east rift zone inferred from experimentally rehomogenized melt inclusions. Geochimica et Cosmochimica Acta 185, 232–250. https://doi.org/10.1016/j.gca.2016.04.020

Wallace, P., Carmichael, I.S.E., 1992. Sulfur in basaltic magmas. Geochimica et Cosmochimica Acta 56, 1863–1874. https://doi.org/10.1016/0016-7037(92)90316-B

Wallace, P.J., Anderson, A.T., 1998. Effects of eruption and lava drainback on the H 2 O contents of basaltic magmas at Kilauea Volcano. Bulletin of Volcanology 59, 327–344. https://doi.org/10.1007/s004450050195

Wallace, P.J., Carmichael, I.S.E., 1994. S speciation in submarine basaltic glasses as determined by measurements of SKα X-ray wavelength shifts. American Mineralogist 79, 161–167.

Westerlund, K.J., Shirey, S.B., Richardson, S.H., Carlson, R.W., Gurney, J.J., Harris, J.W., 2006. A subduction wedge origin for Paleoarchean peridotitic diamonds and harzburgites from the Panda kimberlite, Slave craton: evidence from Re–Os isotope systematics. Contributions to Mineralogy and Petrology 152, 275–294. https://doi.org/10.1007/s00410-006-0101-8

Wieser, P.E., Edmonds, M., Maclennan, J., Jenner, F.E., Kunz, B.E., 2019. Crystal scavenging from mush piles recorded by melt inclusions. Nat Commun 10, 5797. https://doi.org/10.1038/s41467-019-13518-2

Wieser, P.E., Edmonds, M., Maclennan, J., Wheeler, J., 2020. Microstructural constraints on magmatic mushes under Kīlauea Volcano, Hawaiʻi. Nat Commun 11, 14. https://doi.org/10.1038/s41467-019-13635-y

Witham, C.S., Oppenheimer, C., 2004. Mortality in England during the 1783?4 Laki Craters eruption. Bulletin of Volcanology 67, 15–26. https://doi.org/10.1007/s00445-004-0357-7

Witt-Eickschen, G., Palme, H., O’Neill, H.St.C., Allen, C.M., 2009. The geochemistry of the volatile trace elements As, Cd, Ga, In and Sn in the Earth’s mantle: New evidence from in situ analyses of mantle xenoliths. Geochimica et Cosmochimica Acta 73, 1755–1778. https://doi.org/10.1016/j.gca.2008.12.013

Wölbern, I., Jacob, A.W.B., Blake, T.A., Kind, R., Li, X., Yuan, X., Duennebier, F., Weber, M., 2006. Deep origin of the Hawaiian tilted plume conduit derived from receiver functions. Geophysical Journal International 166, 767–781. https://doi.org/10.1111/j.1365-246X.2006.03036.x

Wright, T.L., Fiske, R.S., 1971. Origin of the Differentiated and Hybrid Lavas of Kilauea Volcano, Hawaii. Journal of Petrology 12, 1–65. https://doi.org/10.1093/petrology/12.1.1

Wright, T.L., Peck, D.L., Shaw, H.R., 1976. Kilauea Lava Lakes: Natural Laboratories for Study of Cooling, Crystallization, and Differentiation of Basaltic Magma, in: Sutton, G.H., Manghnani, M.H., Moberly, R., Mcafee, E.U. (Eds.), Geophysical Monograph Series. American Geophysical Union, Washington, D. C., pp. 375–390. https://doi.org/10.1029/GM019p0375

Wulf, A.V., Palme, H., Jochum, K.P., 1995. Fractionation of volatile elements in the early solar system: evidence from heating experiments on primitive meteorites. Planetary and Space Science 43, 451–468. https://doi.org/10.1016/0032-0633(94)00189-X

Appendix A: Chalcophile elements track the fate of sulfur at Kīlauea Volcano, Hawai'i

Penny E. Wieser*[1], Frances Jenner[2], Marie Edmonds[1], John Maclennan[1], and Barbara E. Kunz[2].

[1] Department of Earth Sciences, University of Cambridge, Downing Street, Cambridge, UK, CB2 3EQ.
[2]School of Environment, Earth and Ecosystem Sciences, The Open University, Walton Hall, 7 Milton Keynes, Buckinghamshire, MK7 6AA.
**Corresponding Author: pew26@cam.ac.uk*

Additional Figures

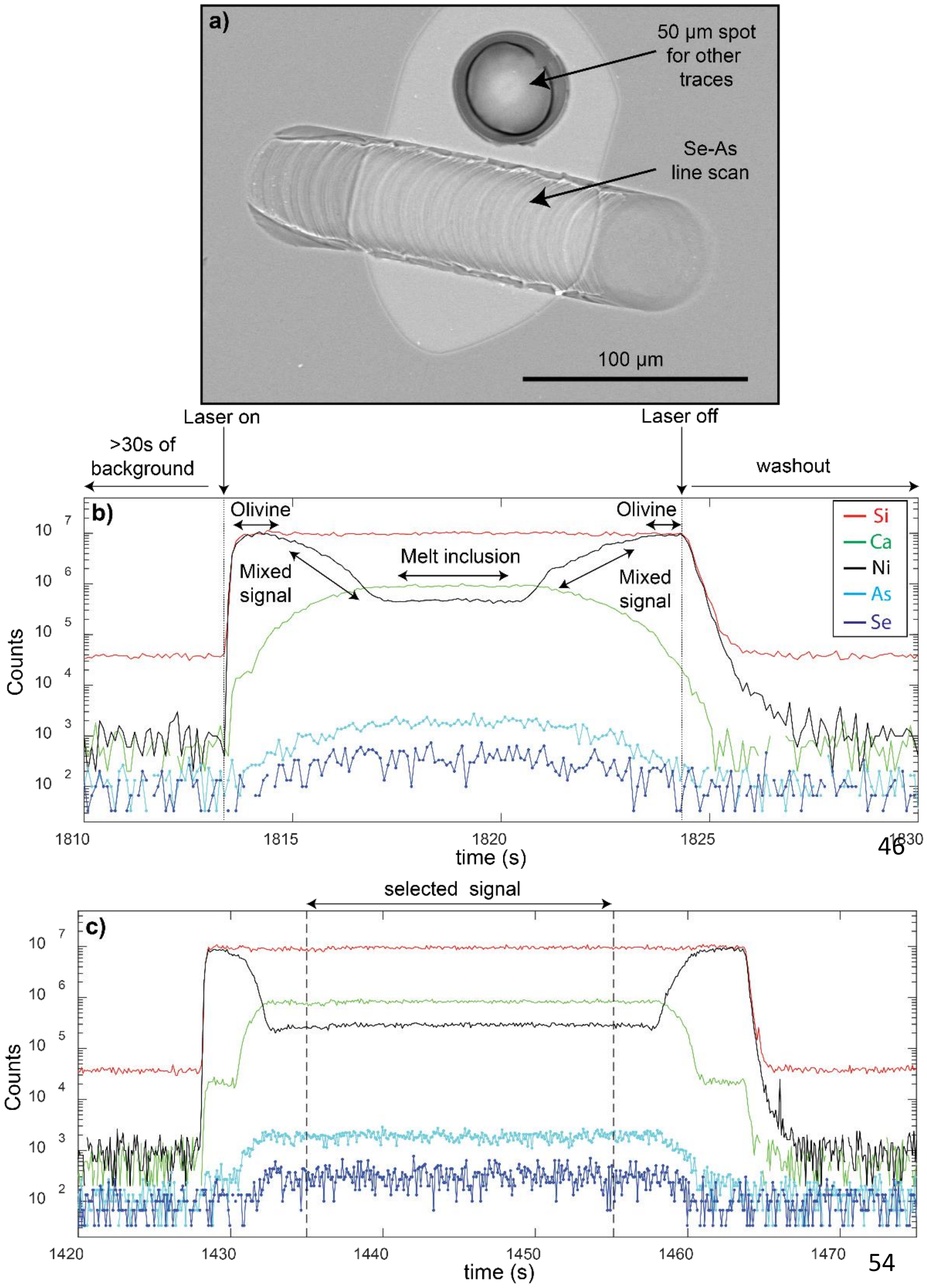

Figure A1- Examples of Se-As line scans. **a)** BSE image of melt inclusion with a 50 µm laser spot and a Se-As line scan. **b)** Raw signal for the Se-As line scan shown in a). The line scan starts in the host olivine crystal (which has high Ni, and low Ca contents). The rapid drop in Ni, and increase in Ca marks the mixing of the signal of the melt inclusion and the host olivine. Signals from the melt inclusion were selected based on the presence of a flat plateau in Ni and Ca contents. The selected signal in this instance was relatively short (2.04s) due to the relatively small size of the melt inclusion. **c)** Line scan signals from a significantly larger melt inclusion (selected signal = 20.1s).

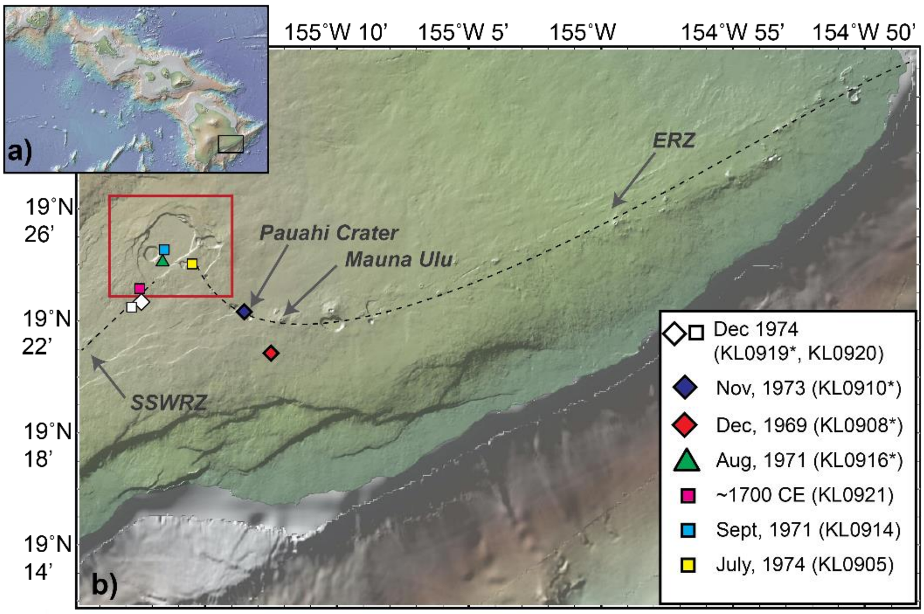

Figure A2 – Sample locations for eruption deposits examined in this study. Samples used for melt inclusion work are indicated with an asterisk. Other samples shown were found to contain sulfides during BSE-SE mapping. Maps were produced in GeoMap App (http://www.geomapapp.org; Ryan et al. 2009), and show the topography of Kīlauea before the onset of the 2018 summit collapse.

Sample Details

Sample Code	Eruption Date	Description	Location	GPS
KL0908*	Dec 30th, 1969	Ep. 12 Mauna Ulu	ERZ	19˚ 20.839‘ N, 155˚ 12.518‘ W
KL0910*	Nov 10th, 1973	Pau’ahi Crater	ERZ	19˚ 22.313‘ N, 155˚ 13.510‘ W
KL0916*	Aug 14th, 1971	Spatter ramparts in summit caldera	Intracaldera	19˚ 24.137‘ N, 155˚ 16.644‘ W
KL0919*	Late Dec, 1974	Ka’u Desert	SSWRZ	19˚ 22.649‘ N, 155˚ 17.609‘ W
KL0920	Late Dec, 1974	Ka’u Desert	SSWRZ	19˚ 22.603‘ N, 155˚ 17.713‘ W
KL0905	July 19th-22nd, 1974	Lua Manu Crater	Extracaldera	19˚ 23.935‘ N, 155˚ 15.337‘ W
KL0914	September 24th-29th , 1971	Spatter ramparts in summit caldera	Intracaldera	19˚ 24.580‘ N, 155˚ 16.631‘ W
KL0921	~1700 CE	Spatter ramparts	SSWRZ	19˚ 22.989‘ N, 155˚ 17.464 ‘W

Table A1 - Information for samples analysed in this study. Melt inclusion analyses were conducted on samples indicated with an asterisk (*). The other samples were examined for sulfide occurrence.

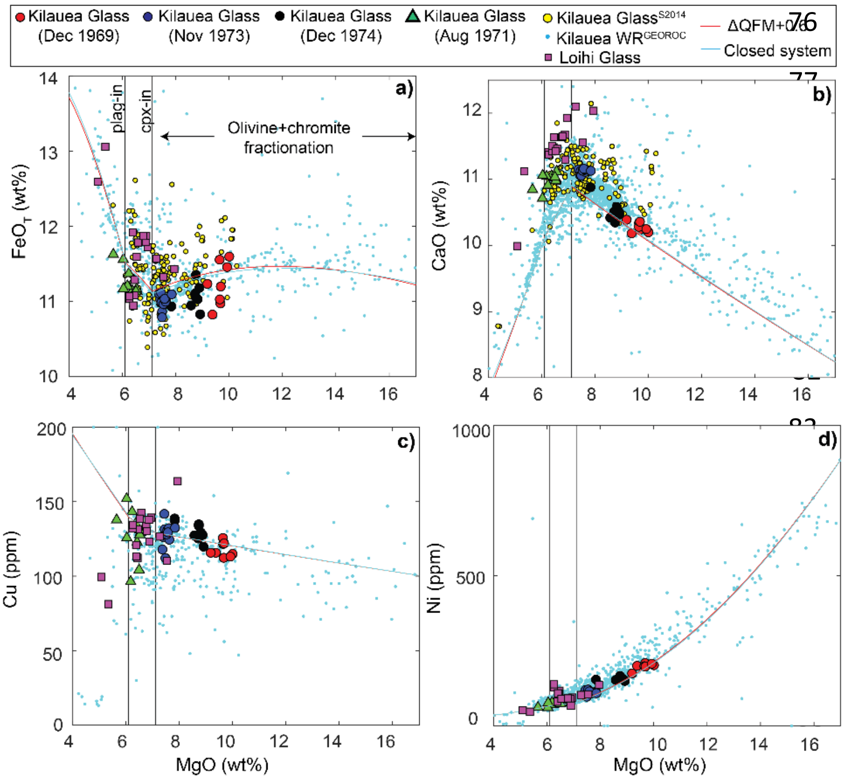

Figure A3 – **a-b)** Glass major element compositions demonstrate that the three rift eruptions investigated in this study (1969, 1973, 1974) have not fractionated beyond olivine control. The 1971 summit eruption shows a relative enrichment in FeO, and depletion in CaO, indicative of clinopyroxene fractionation. Similarly, Lōiʻhi glasses lie on trajectories indicating that they have experienced clinopyroxene (and some plagioclase) fractionation. Kilauean glass compositions from Sides et al. (2014) and whole rock measurements from GEOROC are also overlain. Fractionation paths from Petrolog3 are shown for a buffered and closed systems. The FeO$_T$ content of primary melts was reduced from that of Clague et al. (1991) by 3.2% to improve the model fit. Particular detail was paid to the fit of FeO$_T$ as this strongly controls the SCSS. **c-d)** This fractionation model recreates available Ni and Cu data (model details in main text).

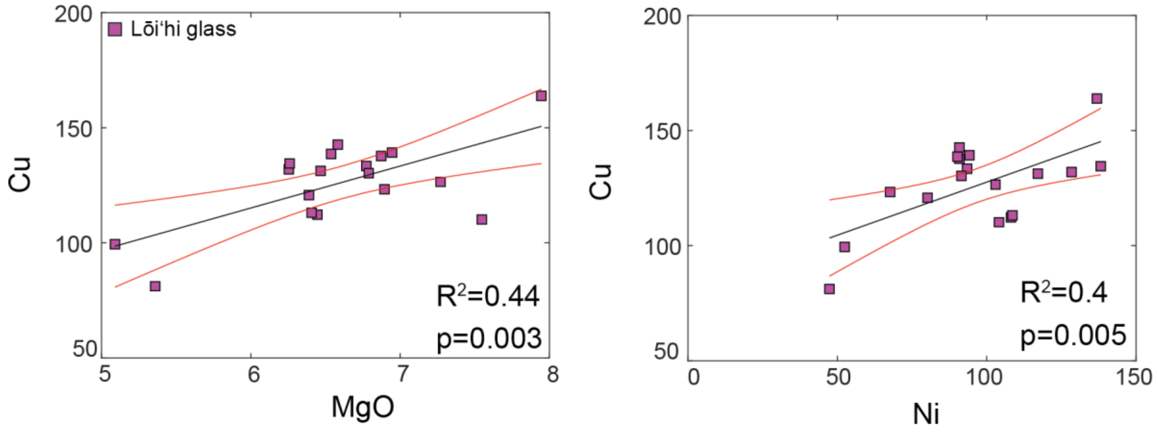

Figure A4 – Lōiʻhi glasses show a positive correlation between Cu and MgO, and Cu and Ni (indicative of sulfide fractionation).

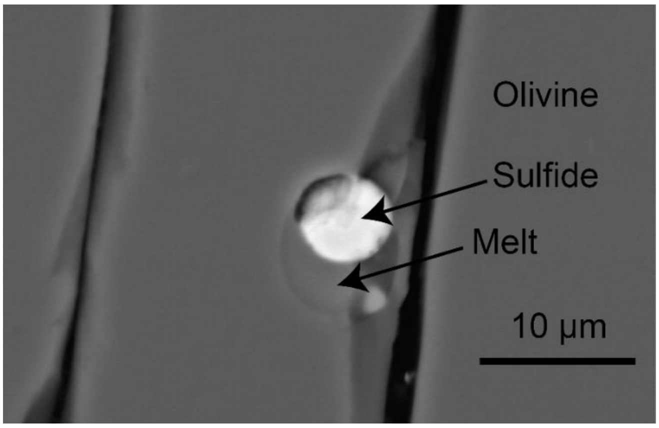

Figure A5 – A large sulfide within a small melt inclusion. From a mass balance perspective, this sulfide cannot have grown after melt inclusion entrapment (the melt would have needed ~5-15 wt% Cu and Ni).

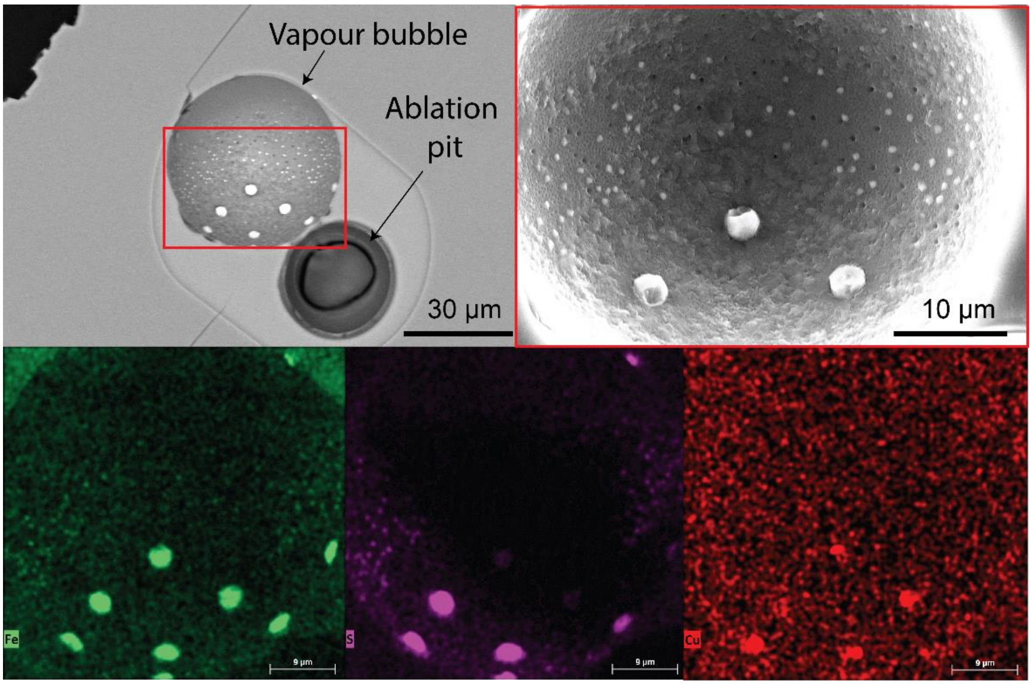

Figure A6– Bimodal-sized Fe-Cu rich sulfides within a melt inclusion vapour bubble

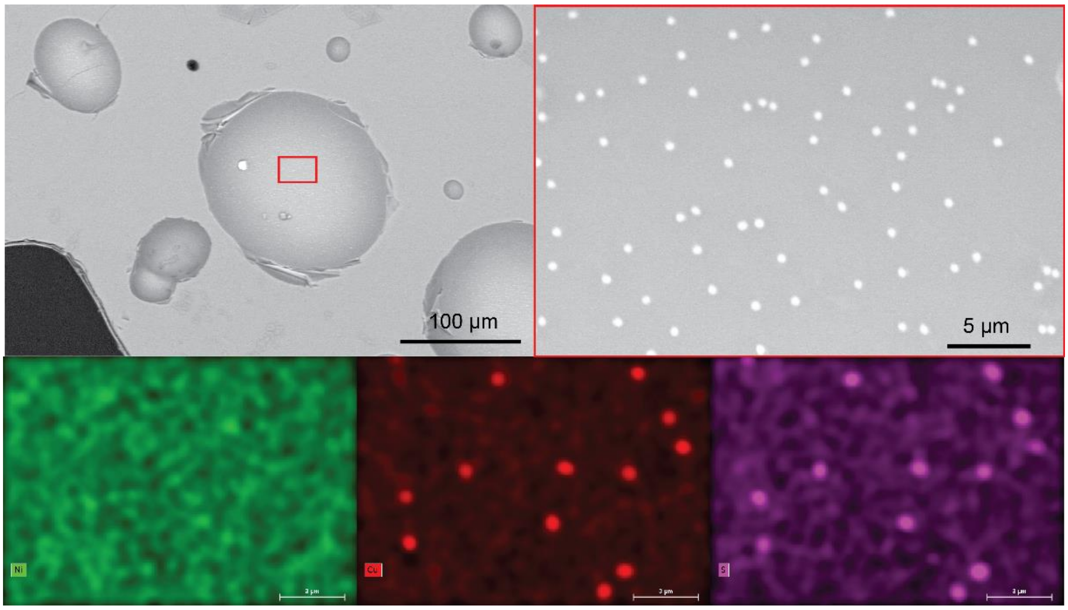

Figure A7–Tiny Fe-Cu-rich sulfides within matrix glass vesicles.

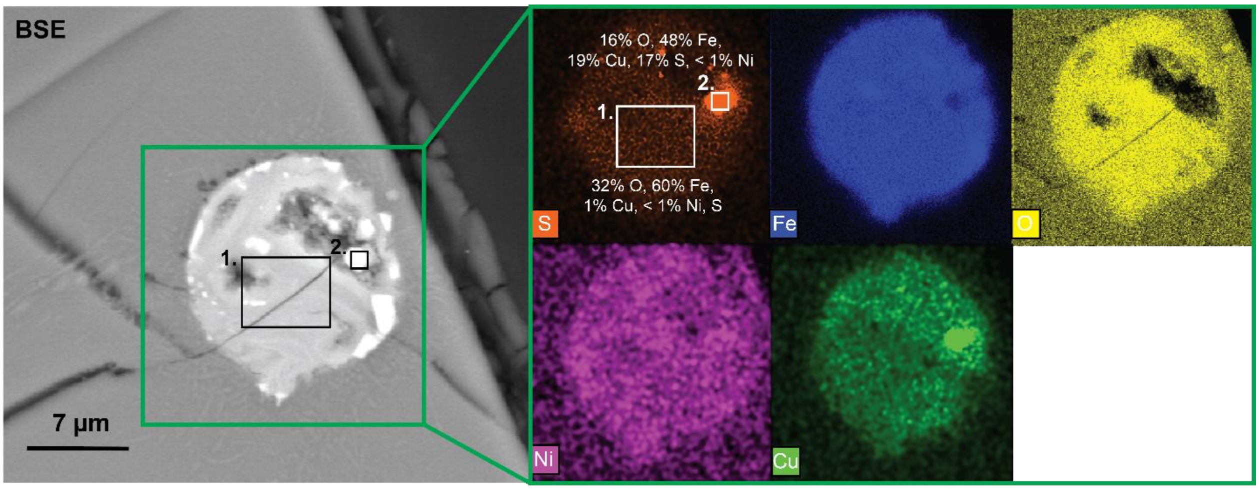

Figure A8 –A broken down sulfide within the matrix glass. Area 1 is almost entirely composed of iron oxide, while area 2 is still relatively sulfur and copper-rich (although it also contains significant amounts of O, unlike pristine sulfides; see Fig. A9).

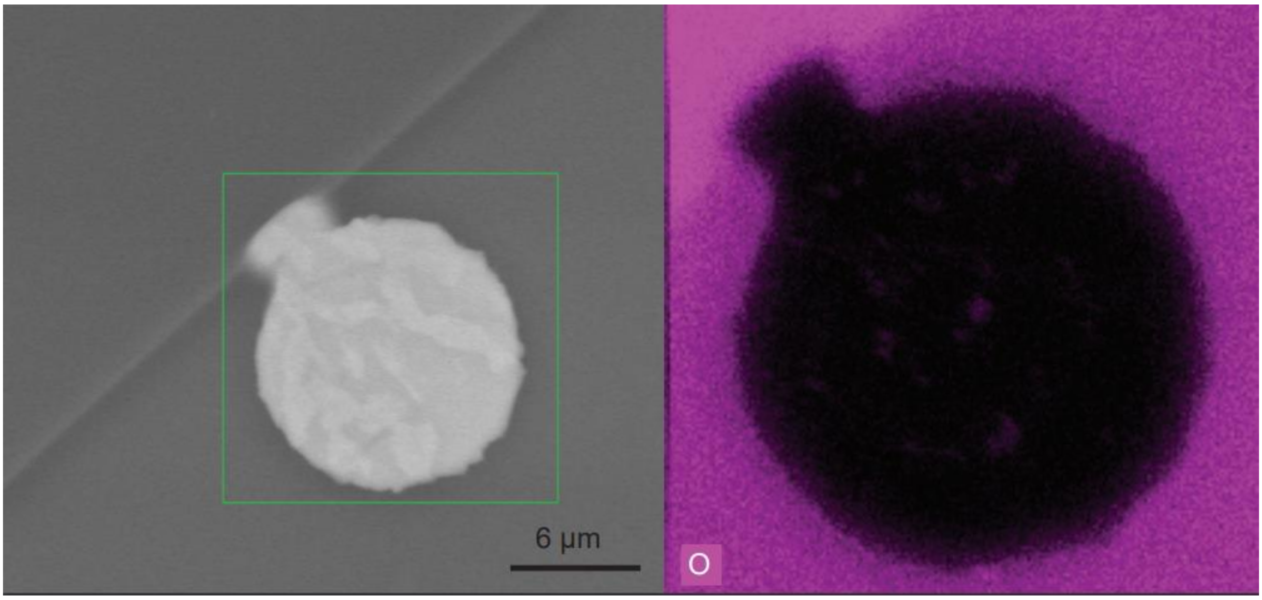

Figure A9 –Map of O in a sulfide which does not show textural evidence for resorption. The sulfide is very O-poor (compare to Fig. A8, Fig. 6).

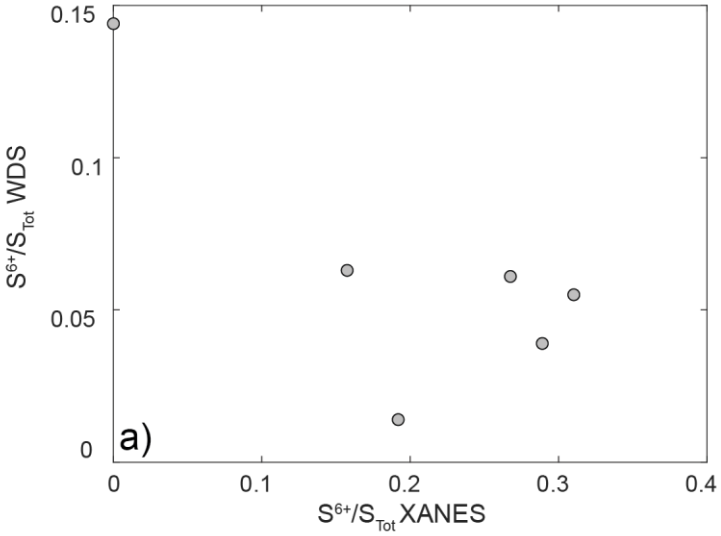

Figure A10 –A comparison of S^{6+}/S_{Tot} ratios determined by Wallace and Carmichael (1992) and Jugo et al. (2010) for the same samples from Lōiʻhi. There is no real correlation between the two measurements, showing that the S-redox state of Hawaiian magmas is very poorly constrained.

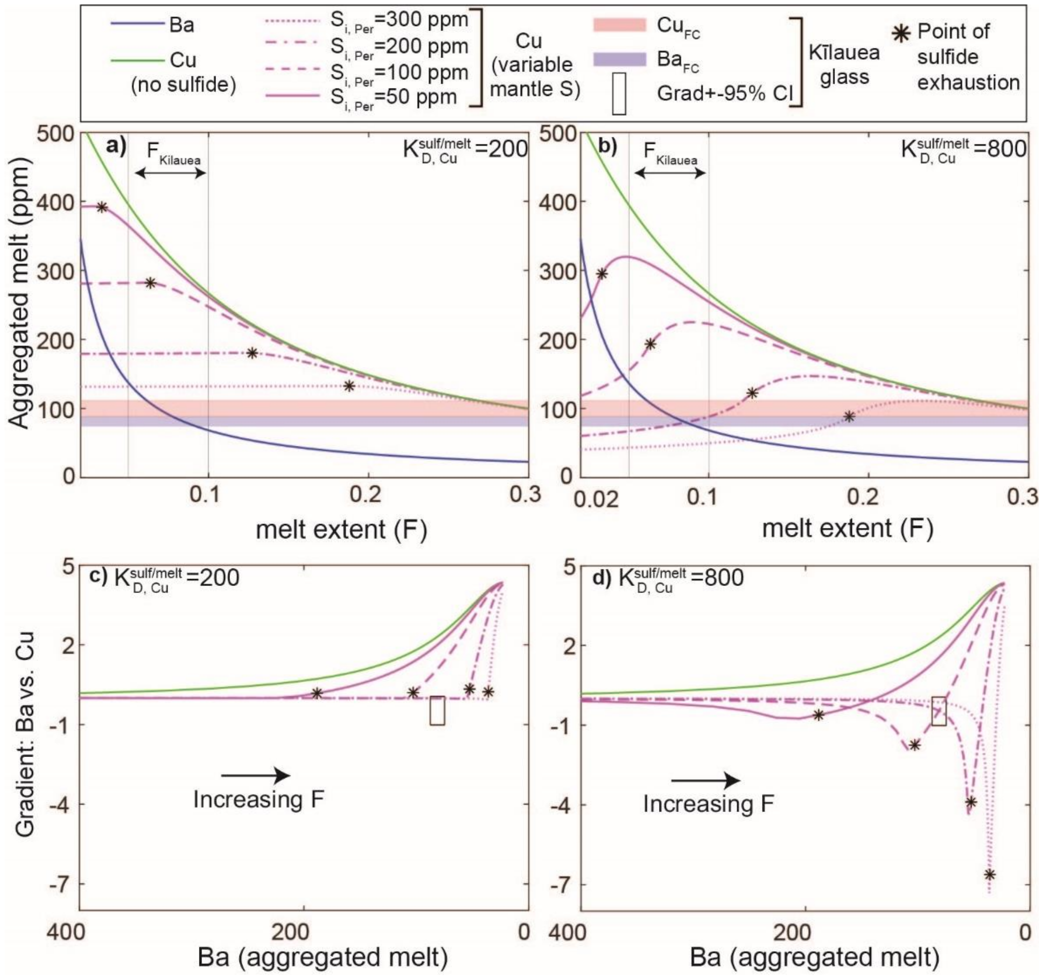

Figure A11 – Models shown in figure 9 in the text, but for initial source Cu concentrations of 30 ppm.

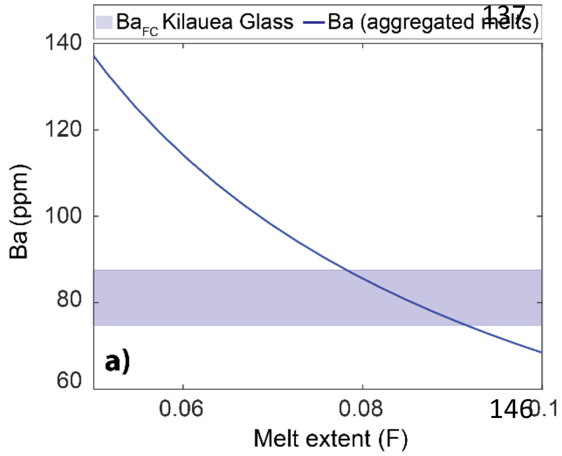

Figure A12 –The range of fractionation corrected Ba concentrations in matrix glasses suggests that the mantle source experienced melt extents of ~F=0.078-0.091 *(*for *Ba$_i$*=6.85; Palme and O’Neill, 2014). Other incompatible trace elements such as La and Ce predict similar F values.

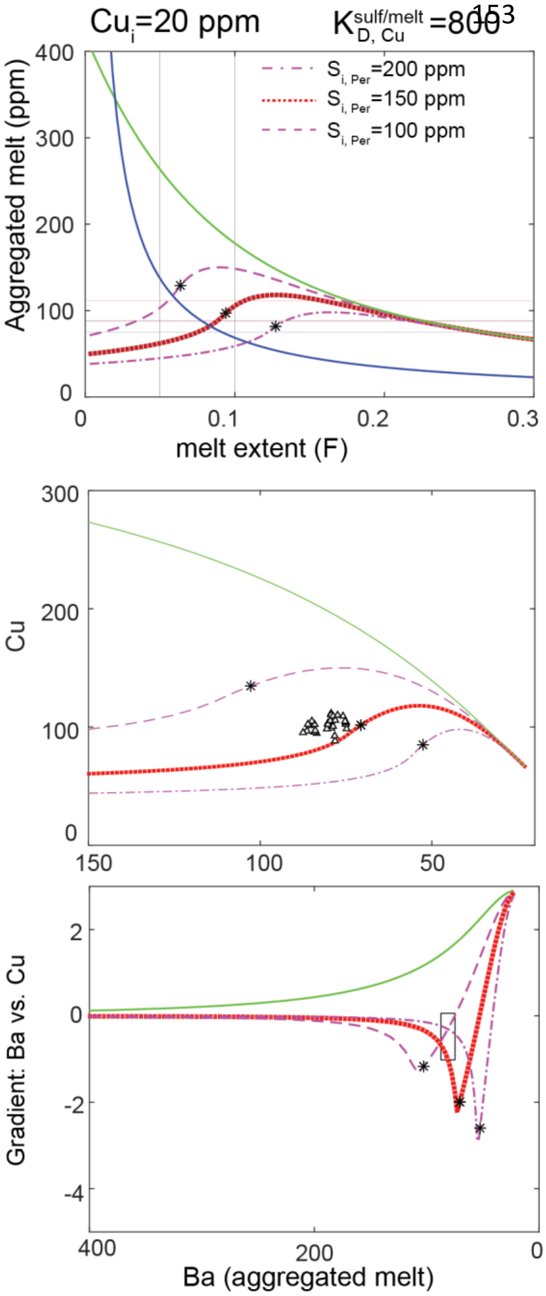

Figure A13 –Models for S_i=150 ppm highlighted in red. Although this model scenario recreates observed Cu and Ba concentrations, it only glances through the 95% confidence interval of the observed gradient.

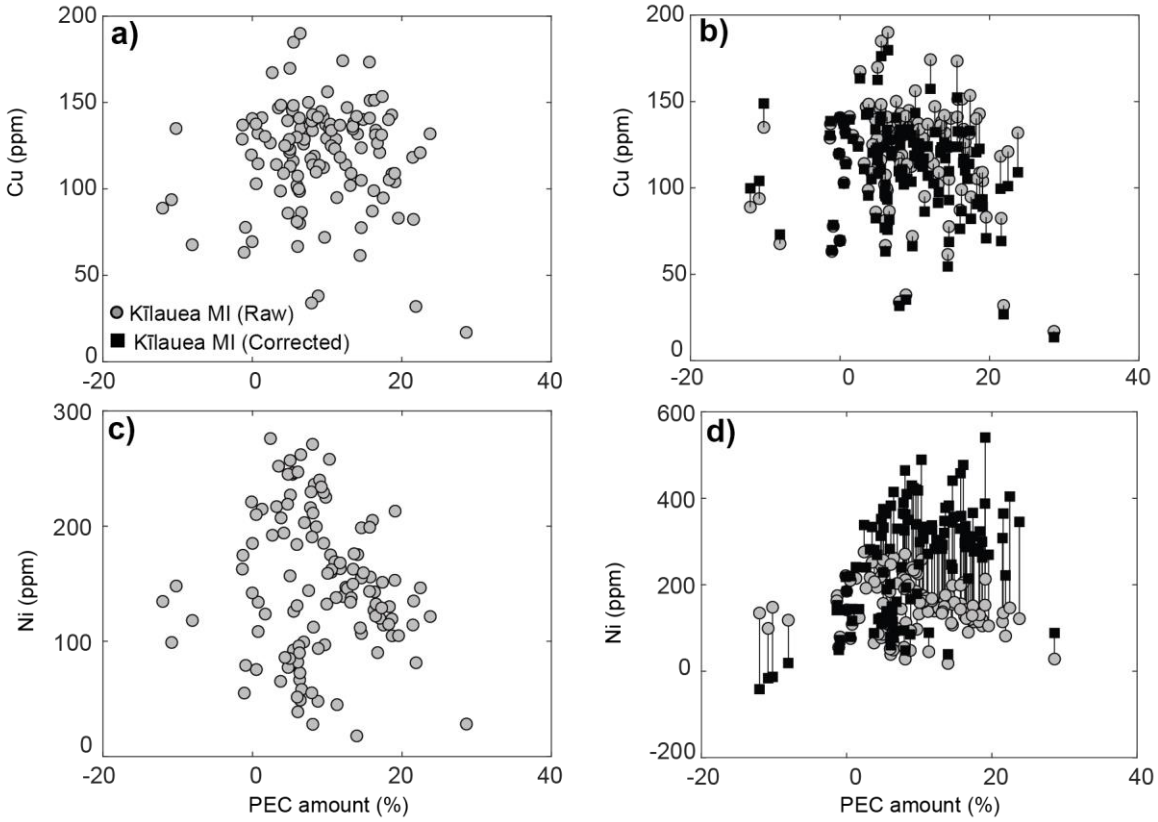

Figure A14–There is no correlation between the Ni and Cu contents of melt inclusions and the amount of PEC crystallization (calculated in Petrolog3). The PEC correction does not alter the Cu contents by very much. Ni is a bit more sensitive, due to its high compatibility in olivine (here $K_{D,\ Ni}^{ol\text{-}melt}$ = 10.6).

Mantle Melting Model Details

Cu-Ba trajectories shown in Figure 6 were created using an iterative loop with 100 steps between F=0 and F=0.3 following the modelling approach described in Lee et al. (2012). In the Equations below, the mass of peridotite residue (M) is used instead of F (F=1-M). The amount of melting occurring in each step was calculated from:

$$\Delta M = |M(i-1) - M(i)|$$

At each step, the amount of S left in the mantle residue was calculated using a mass balance between the amount of melting occurring in that step, and the concentration of S in the melts (S_{Melt} = 1600 ppm).

$$S_{Mantle}(i) = \frac{M(i-1) * S_{Mantle}(i-1) - S_{Melt} * \Delta M}{M(i)}$$

The amount of sulfide present in the mantle was calculated from the amount of S remaining in the residue, assuming that mantle sulfides contain 33 wt% S.

$$X_{sulf}(i) = \frac{S_{Mantle}(i)}{33 \times 10^4}$$

The bulk K_D was calculated assuming that the proportions of silicate phases stayed fixed throughout the melting interval (for simplicity).

$$K_{D,bulk}(i) = K_{D,bulk\ silicate} * \left(1 - X_{sulf}(i)\right) + K_{D,sulfide} * X_{sulf}(i)$$

Incorporating non-modal melting into the model does not affect the result, as the K_D of Cu in sulfide is many orders of magnitude higher than the K_D of silicate phases. The bulk K_D of silicate phases for Ba and Cu was calculated assuming the mantle source contains 59.8% olivine, 21.1% orthopyroxene, 13% clinopyroxene and 11.5% garnet (Mckenzie and O'Nions, 1991). Partition coefficients from Ba were taken from Gibson and Geist (2010). Partition coefficients for Cu were taken from Liu et al. (2014).

K_D silicate-melt	Garnet	Clinopyroxene	Olivine	Orthopyroxene
Ba	0.00007	0.0004	0.000005	0.000006
Cu	0.03	0.06	0.05	0.04

The concentration of each element [C] in the instantaneous melt at each step was calculated from:

$$[C]_{inst}(i) = \frac{Cu_{Mantle}(i-1)}{K_{D,bulk}(i) + \left(1 - K_{D,bulk}(i)\right) * \frac{\Delta M}{M(i-1)}}$$

The concentration of each element [C] in the aggregated fractional melts was calculated from:

$$[C]_{Agg}(i) = Fracmelt(i) * [C]_{inst}(i) + \left(1 - Fracmelt(i)\right) * [C]_{Agg}(i-1)\ )$$

Where:

$$Fracmelt(i) = \frac{|M(i-1) - M(i)|}{|M(1) - M(i)|}$$

The concentration of each element [C] in the mantle residue was calculated from:

$$[C]_{Mantle}(i) = \frac{M(i-1) * C_{Mantle}(i-1) - C_{inst} * \Delta M}{M(i)}$$

Analytical Methodology

EDS analysis

EDS maps collected at 20kV were quantified using Esprit 2.1 software. An area was drawn around the sulfide in question, excluding the outer ~1 µm to avoid beam interaction with the surrounding olivine or host glass. The spectra was quantified using a P/B ZAF model with background collection. Sulfides with coarsely exsolved Cu-Ni-Fe rich phases were not quantified (e.g. Fig. 5f) as different 3D cuts through such features will yield very different bulk analyses. Three inhouse sulfide standards, a pyrite (UWPY-1), a chalcopyrite (Nifty) and a pentlandite were quantified with EPMA analysis, and then mapped for ~20 mins by EDS in the same analytical session as the Hawaiian sulfide blebs.

Ni, Cu, S and Fe analysis on these inhouse sulfide standards was conducted by EPMA at 20 kV, 20 nA and a 5 µm spot using the following crystals, calibration materials and count times.

Table A2– Conditions for EPMA analyses of sulfide standards.

	Crystal	**Calibration material**	**Peak count time**
S	PET	Pyrite	10 s
Cu	LLIF	Cu metal	30 s
Ni	LIF	Ni metal	30 s
Fe	LIF	Pyrite	10 s

The average EPMA results for these standards can be found in Appendix B.

LA-ICP-MS analysis

Two separate analytical conditions were used for LA-ICP-MS analysis; all reported concentrations of elements except Se and As were analysed in the "trace element" routine (although this was altered slightly for 25 µm spot sizes). All analyses were conducted with a fluency of 3.63 J/cm^2, 0.9l/min of He, 0.77 l/min of Ar carrier gas, and 15 l/min of Ar plasma gas. 5 ml/min N_2 was added downstream for trace element spots smaller than 25 µm, and Se-As analyses, to increase sensitivity. Additional information is provided in table 1.

Table A3– Conditions for spot analyses and line analysis

	Background	**Signal**	**Repetition rate**	**Scan speed**	**Oxygen gas flow**
Spot Analysis (Trace elements)	30s	20s	10 Hz	N/A	N/A
Spot Analysis (Se-As	30s	20s	20 Hz	N/A	N/A
Line scans (Se & As)	30s	Length of line in melt inclusion	50 Hz	15 µm/sec	0.47ml/min into reaction cell

Se-As line scans started and ended in the surrounding olivine to maximise the signal. In order to select the signal from the melt inclusion (rather than a mixed signal between the melt inclusion and the surrounding olivine), we analysed masses ^{29}Si, ^{43}Ca, ^{60}Ni, $^{75\to91}$As and $^{80\to96}$Se. The signal from the olivine is characterized by low Ca and high Ni. As the laser starts ablating the host olivine and melt inclusion, a mixed signal is acquired, characterised by rapidly decreasing Ni concentration as the line scan moves further into the melt inclusion. Signals were selected based on the presence of a flat Ni plateau, and the concentrations from this plateau were compared to the Ni concentrations collected during spot analysis of the same inclusion (Supplementary Fig. A1).

Additional References

Gibson, S.A. and Geist, D., 2010. Geochemical and geophysical estimates of lithospheric thickness variation beneath Galápagos. Earth and Planetary Science Letters, 300(3-4), pp.275-286.

McKenzie, D., and O'Nions, R., 1991, Partial melt distributions from inversion of rare earth element concentrations. Journal of Petrology, 32, no. 5, p. 1021-1091.

Ryan, W. B. F. et al. Global multi-resolution topography synthesis. Geochem. Geophys. Geosyst. 10, 1–9 (2009).